Calibration and Temperature Correction of Multi-Wire Constant-Temperature Anemometers

F.K. Aleksandrowicz

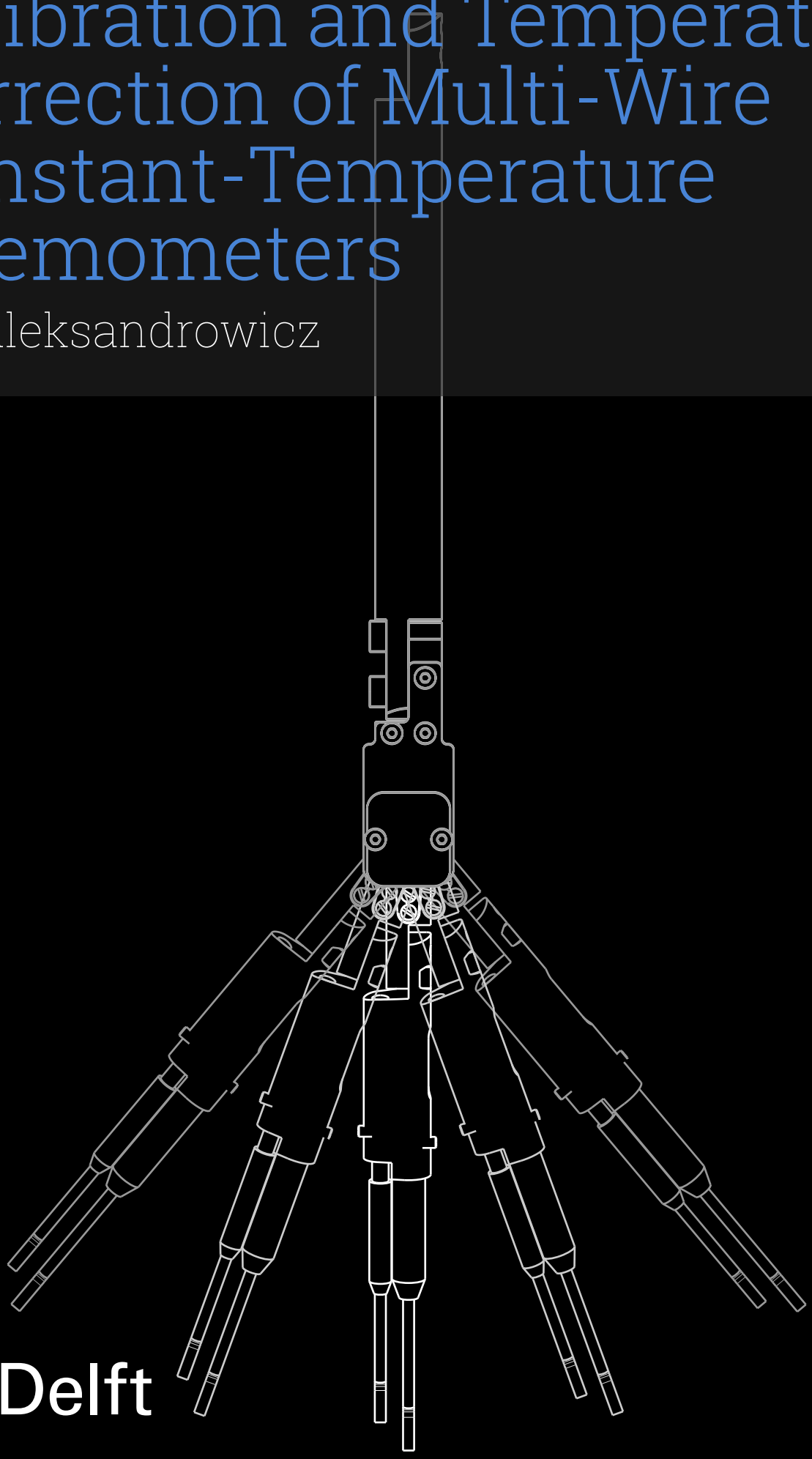

TU Delft

Calibration and Temperature Correction of Multi-Wire Constant-Temperature Anemometers

by

F.K. Aleksandrowicz

to obtain the degree of Master of Science
at the Delft University of Technology,
to be defended publicly on Monday December 15, 2025 at 11:00.

Student number:	4809505	
Project duration:	March 10, 2025 – December 8, 2025	
Thesis committee:	Prof. Dr. M. Kotsonis,	TU Delft, responsible supervisor
	Dr. W. Baars,	TU Delft, chairman
	Dr. C. Falsetti,	TU Delft, examiner
	M. Barahona,	TU Delft, daily supervisor

TU Delft

Preface

This thesis marks the end of my seven-year-long endeavor at TU Delft. I am certain that I will always look back on this period with great fondness, and for that reason I want to thank everyone who contributed.

I would like to offer my gratitude to my supervisor, Prof. Marios Kotsonis, for the opportunity to work on this thesis and for his support throughout the project. However, it would not have been possible for me to finish this work without Marina Barahona, my daily supervisor, who provided invaluable day-to-day guidance and taught me everything about working with hot-wires and conducting experiments in wind tunnels. I would also like to thank the support staff at the Low-Speed Wind Tunnel Laboratory, especially Stefan Bernardy, who was always there to answer my questions about LabView. Additionally, I am grateful to the remaining members of my defense committee, Dr. Woutijn Baars and Dr. Chiara Falsetti, for offering their time and expertise to evaluate my thesis.

What truly laid the foundations for this work was Delft Aerospace Rocket Engineering. During my more than six-year-long journey there, I learned how to design, build, and test hardware that actually works. I am deeply grateful to all the friends I made along the way—those who shared the moments of joy (and of failure) and who taught me how to be a real engineer. This experience is what made my time at TU Delft unforgettable, and it will stay with me for the rest of my life.

Finally, a huge thanks to my parents, my sister, and my girlfriend Tuğçe. Without their continuous support and encouragement, it would not have been possible for me to reach this point.

F.K. Aleksandrowicz
Delft, December 2025

Summary

Hot-wire anemometry (HWA) remains an essential diagnostic tool for high–frequency velocity measurements in aerodynamic research, yet its practical accuracy strongly depends on robust temperature correction and reliable multi–component probe calibration. Despite the maturity of the technique, the literature provides no consensus on how best to correct for fluid–temperature variations or how to calibrate X-wire probes with consistent accuracy across wide velocity and angular ranges. The situation is further complicated at the TU Delft Low-Speed Wind Tunnel Laboratory (LSL), where the absence of an in-situ multi-wire calibration system has made efficient and repeatable probe preparation difficult. This thesis addresses these issues by developing a new automated calibration framework for multi-wire CTA probes and performing a comprehensive evaluation of existing temperature-correction and X-wire calibration schemes.

The first part of the work concerns the separation of velocity and temperature effects in CTA measurements. Six temperature-correction models—ranging from simple Bearman [1]-type scaling ignoring the change in fluid properties with temperature, to more complex formulations incorporating fluid-property variations and the Collis & Williams factor [2] are applied to four independent datasets from literature, covering a wide range of velocities and temperature conditions. Each model is assessed by collapsing data acquired at varying temperatures onto a single fourth-degree polynomial calibration curve to quantify the residual error via normalized root mean square percentage error. Across all datasets, simple temperature corrections perform surprisingly well. Relying on resistance-based wire-temperature estimation suffers from uncertainty, with the best success when calculating the fluid properties at the film temperature and applying the Collis & Williams correction. Allowing the wire temperature to act as an optimization parameter can improve the fit of the curves, confirming earlier findings that resistance-derived temperatures can introduce systematic error.

The second part of the thesis focuses on the calibration of X-wires. A new miniature, high-precision, in-situ yaw calibrator is designed and implemented. The device integrates a compact high-torque servo motor and a magnetic rotary encoder with high accuracy, assembled using high-precision alignment procedures. With the calibration and controlled through a LabView interface, and the position feedback and servo control integrated via an Arduino implementation, the system enables automated yaw sweeps. Its compact form factor allows installation directly inside restricted wind-tunnel test sections.

Using this system, a dense X-wire calibration dataset was collected, spanning velocities from 5 to $30\,\mathrm{m\,s^{-1}}$ in $1\,\mathrm{m\,s^{-1}}$ increments and yaw angles from -40° to 40° in 1° steps. The dataset enabled comparison of calibration schemes, including interpolation-based indirect methods (Lueptow [3] and Tropea [4] variants), and direct polynomial surface

fits. Method performance is evaluated using modified RMSPE metrics of the reconstructed velocity components u and v. The results demonstrate that interpolation-based offer the best accuracy but show greater sensitivity to calibration-grid sparsity, requiring a grid of at least 8 velocity and 25 angle steps. The Lueptow variant was found to perform unreliably near calibration domain boundary. Fourth-degree direct polynomial surface fits applied to the velocity components yielded reasonable accuracy and robustness across the domain, much better polynomial fits of velocity magnitude and angle, while allowing a three-times smaller calibration grid of 5x15 points.

Overall, this thesis delivers three principal contributions: (1) a quantitative cross-dataset assessment of widely used temperature-correction schemes, (2) the design and commissioning of a compact and versatile in-situ X-wire calibrator, and (3) a comprehensive evaluation of X-wire calibration methods and the required density of calibration grids. The outcomes provide a practical foundation for improving the reliability and accessibility of multi-component CTA measurements in future aerodynamic experiments.

Contents

Nomenclature

Abbreviations

Abbreviation	Definition
CCA	Constant Current Anemometry
CTA	Constant Temperature Anemometry
CVA	Constant Voltage Anemometry
C&W	Collis & Williams correction
HWA	Hot-wire Anemometry
LSL	TU Delft Low-speed Wind Tunnel Laboratory
RMSE	Root Mean Square Error
RMSPE	Root Mean Square Percentage Error

Symbols

Symbol	Definition	Unit
c	Heat capacity	[$\mathrm{J\,K^{-1}}$]
d	Diameter	[m]
E	Voltage	[V]
f, g	Generic function	[-]
Gr	Grashof number	[-]
h	Convective heat transfer coefficient	[$\mathrm{W\,m^{-2}\,K^{-1}}$]
I	Electrical current	[A]
Kn	Knudsen number	[-]
k	Wire directional sensitivity in yaw	[-]
l	Length	[m]
N	Number of points	[-]
Nu	Nusselt number	[-]
Pr	Prandtl number	[-]
$\dot{Q}$	Heat flow	[W]
$\dot{Q}_v$	Heat generation rate inside the body	[W]
q	Dynamic pressure	[Pa]
R	Electrical resistance	[Ω]
Re	Reynolds number	[-]
T	Temperature	[K]
t	Time	[s]
U	Velocity	[$\mathrm{m\,s^{-1}}$]
u	Velocity parallel to the probe axis	[$\mathrm{m\,s^{-1}}$]

Symbol	Definition	Unit
v	Velocity perpendicular to the probe axis in-plane with the wires	[$\mathrm{m\,s^{-1}}$]
w	Velocity perpendicular to the probe axis out-of-plane with the wires	[$\mathrm{m\,s^{-1}}$]
α	Pitch angle of hot-wire probe	[°]
ε	Root Mean Square Percentage Error	[%]
λ	Heat conductivity	[$\mathrm{W\,m^{-1}\,K^{-1}}$]
ν	Kinematic viscosity	[$\mathrm{m^2\,s^{-1}}$]
ρ	Density	[$\mathrm{kg\,m^{-3}}$]
σ_U, σ_u, σ_v	Root Mean Square Error of velocity U or velocity component u or v	[$\mathrm{m\,s^{-1}}$]
σ_ϕ	Root Mean Square Error of yaw angle	[°]
ϕ	Yaw angle of hot-wire probe	[°]
$\bar{\phi}$	Inclination angle of a wire in an X-probe	[°]

Subscripts and superscripts

Subscript	Definition
a	At free-stream of fluid
c	Calulated from calibration
cp	Conduction to prongs
e	Effective
f	At ”film” of fluid
m	Measured
h	Convection
r	Radiation
w	Wire

Superscript	Definition
$*$	Corrected for fluid temperature drift, ”at reference fluid temperature”
(i)	At angle step ϕ_i
(j)	At velocity step U_j

1

Introduction

Hot-Wire Anemometry (HWA) remains a widely used measurement technique for high-frequency velocity measurements in aerodynamics. Although the technique is nearly a century old, it continues to play an important role in the study of wall-bounded and free shear flows, as is the case at the Low-Speed Wind Tunnel Laboratory (LSL) of TU Delft.

However, the reliability of hot-wire measurements depends on careful probe calibration prior to experiments. Although the physical principles of HWA are well documented, the literature reveals a lack of consensus on two key calibration aspects:

1. A universal method to correct hot-wire measurements for fluid temperature in flows with large temperature variations.

   Multiple approaches have been proposed for temperature correction. Some neglect the variation of fluid properties, while others propose semi-empirical corrections based on fluid properties calculated at different reference temperatures. The recommendations sometimes disagree, and there is a lack of comprehensive comparisons across datasets.

2. Different accuracies among methods used to obtain magnitude and direction of flow from the voltage measured from multi-wire probes.

   Numerous calibration schemes have been proposed, including the so-called various effective-velocity methods, look-up-table approaches, and direct fitting methods. However, a robust comparison of the performance of these methods across different velocities and flow directions is still missing in literature.

In experiments at the LSL, the lack of established best-practices combined with practical difficulty of calibration of X-wire probes in diverse experimental setups often leads to convoluted setup and calibration approaches, which make HWA measurements less accessible to entry-level experimentalists.

This thesis aims to address these gaps by developing a new, automated calibration framework and hardware for multi-wire constant-temperature anemometry in applications under variable thermal conditions, designed for in-situ operation in the wind

tunnel sections.

The work combines a comprehensive literature review of HWA calibration and correction methods, mechanical design of a new multi-wire probe calibrator, compilation of a comprehensive X-wire experimental calibration dataset, and experimental evaluation of different calibration schemes. The contributions include:

- A quantitative comparison of temperature correction methods across four independent datasets from literature.
- A new custom-built, high-precision yaw actuation system designed for in-situ X-wire calibration during experiments.
- An extensive X-wire dataset under a wide range of velocities and flow angles.
- A quantitative comparison of X-wire calibration schemes and the effect of calibration grid resolution.

The structure of the report is as follows: Chapter 2 reviews the theoretical background of HWA and common calibration techniques. Chapter 3 outlines the research gap and defines the research objectives and research questions. Chapter 4 presents the methodology. Chapter 5 provides the results for the temperature-correction and X-wire calibration studies. Finally, Chapter 6 offers the conclusions and recommendations for future work.

2

Background on Hot-Wire Anemometry

This chapter provides the theoretical background necessary to understand the calibration challenges addressed in this thesis. It first outlines the principles of Hot-Wire Anemometry in Section 2.1, the heat-transfer mechanisms that relate the measured voltage to the flow velocity with emphasis on Constant-Temperature Anemometry.

Next, the approaches to corrections for fluid temperature in hot-wire measurements is discussed in Section 2.2. Since the cooling of the wire depends on both velocity and temperature, changes in fluid temperature introduce ambiguity in the voltage–velocity relation. Several correction approaches exist in literature, but they often disagree, motivating the comparative assessment performed later in this work.

Finally, Section 2.3 introduces multi-wire probes and the methods used to calibrate X-wires for two-component velocity measurements. Both indirect interpolation schemes and direct polynomial fits are reviewed, as these form the basis for the calibration evaluation in subsequent chapters.

2.1. Principles of Hot-Wire Anemometry

Hot-Wire Anemometry relies on measuring the heat transfer from a thin, electrically heated wire placed in the fluid flow to be measured. The velocity of the fluid is determined by measuring the heat lost by the wire through forced convection, which depends on the velocity of the fluid.

Typically, the wire is made of materials with stable properties such as tungsten or platinum to avoid aging. The diameters of the wires can vary over a range of a few micrometers to tens of micrometers, with smaller wires offering better spatial resolution and frequency response [5] at the cost of being more fragile and more difficult to manufacture and repair.

The operating modes used in Hot-Wire Anemometry are explained in Section 2.1.1. The governing heat balance relations are outlined in Section 2.1.2.

2.1.1. Operational modes

Three operational modes of Hot-Wire Anemometry can be distinguished depending on the measuring circuit of the hot-wire - Constant Current Anemometry (CCA), Constant Temperature Anemometry (CTA), and Constant Voltage Anemometry (CVA).

Constant Current Anemometry operates on the simplest principle out of the three - as the electric current flowing through the wire is kept constant, the changes in the resistance of the wire, caused by the change in wire temperature due to changing convective heat transfer, are measured. Because of the finite time needed by the wire temperature to change with flow velocity (thermal inertia), the frequency response of the wire in CC mode is relatively poor [5]. Nowadays, CCA finds use almost exclusively for Cold-Wire Anemometry (CWA), where a wire operated at a low overheat ratio is used to increase sensitivity to fluid temperature, decreasing the sensitivity to velocity. This is due to the fact that CTA exhibits highly non-linear behaviors at low overheat ratios [5, 4].

Constant Temperature Anemometry places the hot-wire in a feedback loop that automatically compensates the current flowing through the wire to keep the temperature (resistance) of the wire constant. An example circuit is shown in Fig. 2.1. Because the thermal inertia of the wire is effectively eliminated and replaced with the delay of the electronic amplifier, the frequency response is orders of magnitude better than in CC mode. To date, CTA remains the main HWA technique.

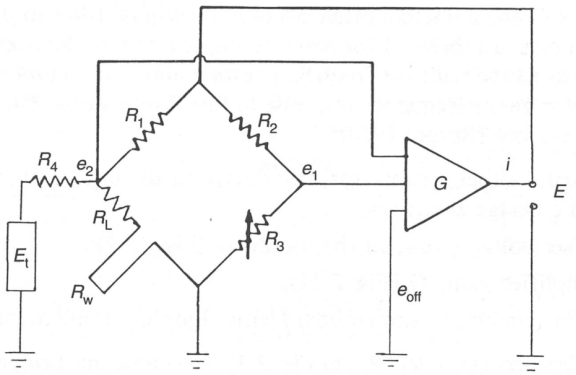

Figure 2.1: A CTA circuit containing a Wheatstone bridge, a feedback amplifier, and an electronic-testing subcircuit [5].

Constant Voltage Anemometry is a relatively new HWA technique, being proposed around 30 years ago [6], compared to more than almost a century for both CCA and CTA. In this case, the voltage across the hot-wire sensor is kept constant. This technique offers a significant improvement over CCA and CTA, due to the elimination of the effect of the capacitance of the cables on the dynamic response, and interference [6]. Nevertheless, CVA has yet to reach widespread adoption and is therefore not treated further.

Due to the continuing wide adoption of CTA for HWA, it is the main focus of this study. Therefore, all following derivations assume that the response of the feedback amplifier is sufficiently fast to guarantee constant wire resistance, and consequently con-

stant wire temperature. This can be assured by modern amplifiers in all but very-high-turbulence conditions [5].

2.1.2. Heat balance of a heated wire

The wire loses heat to the environment by means of forced convection (due to the velocity of the fluid), free convection (flow due to density gradients), radiation, and conduction to the prongs, which due to the significantly larger thermal mass and lower resistance act like heat sinks. The schematic representation of the heat losses of the wire is shown in Fig. 2.2a.

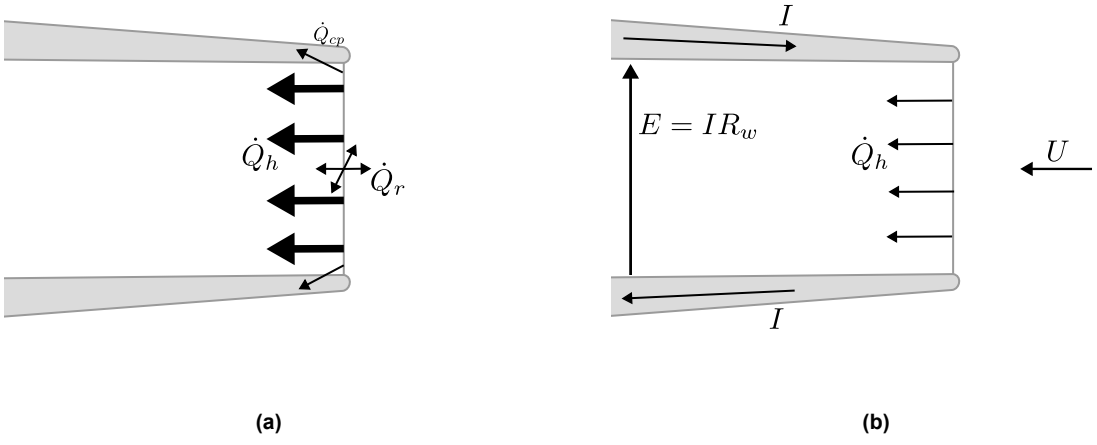

Figure 2.2: Photograph of a hot-wire with a schematic representation of (a) the heat losses of the wire (size of arrows indicates relative importance), and (b) the steady-state heat balance between Joule heating and heat loss due to forced convection. Based on Örlü and Vinuesa [7].

Assuming uniform composition and temperature of the wire T_w and uniform fluid temperature of the fluid around the wire T_a, the heat-balance equation of the wire can be expressed as

$$\frac{\pi}{4} d_w^2 l_w \rho_w c_w \frac{dT_w}{dt} = \dot{Q}_v - \dot{Q}_h - \dot{Q}_r - \dot{Q}_{cp}, \tag{2.1}$$

where $\dot{Q}_v$ denotes heat generated inside the wire, and $\dot{Q}_h$, $\dot{Q}_r$, and $\dot{Q}_{cp}$ denote the heat transfer due to convection, radiation, and conduction to prongs respectively. For typical hot-wire configurations, convection greatly outweighs all other modes of heat loss and they are all ignored. Fingerson and Freymuth [8] showed that convection can be reasonably accurately expressed for most hot-wires through Newton's law of cooling as $\dot{Q}_h = h\pi d_w l_w (T_w - T_a)$. Finally, for Constant-Temperature Anemometry, $dT/dt = 0$, allowing Eq. (2.1) to be expressed as

$$\dot{Q}_v = h\pi d_w l_w (T_w - T_a). \tag{2.2}$$

The heat transfer coefficient h is typically expressed through the Nusselt number $\mathrm{Nu} = \frac{h d_w}{\lambda}$. $\dot{Q}_v$ represents the heat generated inside the wire through Joule heating - for

uniform wire resistance (keeping the uniform material composition assumption), it can be expressed as $\dot{Q}_v = I^2 R_w = EI = \frac{E^2}{R_w}$. Thus, the heat balance is expressed as

$$\frac{E^2}{R_w} = \mathrm{Nu}\lambda\pi l_w d_w (T_w - T_a), \tag{2.3}$$

or after rearranging as

$$\mathrm{Nu} = \frac{E^2}{R_w \lambda\pi l_w d_w (T_w - T_a)}. \tag{2.4}$$

The Nusselt number for thin hot-wires is a complex function $\mathrm{Nu} = f(\mathrm{Re}, \mathrm{Gr}, \mathrm{Pr}, \mathrm{Kn}, T_f/T_a)$ [2]. In practice, the dependence on the Knudsen number is typically neglected, as molecular effects do not play a significant role in typical hot-wire application. Furthermore, the Prandtl number of air can be considered to be approximately constant with respect to temperature. Free convection is also typically either ignored or treated separately from forced convection, removing the dependence on the Grashof number. Thus, the Nusselt number is most dependent on the Reynolds number $\mathrm{Re} = \frac{U d_w}{\nu}$ and the most well-established relation describing this dependence is the classical form based on the work of King [9]:

$$\mathrm{Nu} = A + B\mathrm{Re}^n, \tag{2.5}$$

sometimes also written as

$$\mathrm{Nu} = A + BU_{eff}^n. \tag{2.6}$$

In both equations, A and B can still be considered functions of T_w and T_a. Both Eqs. (2.5) and (2.6) and other similar forms are commonly referred to as ”King’s law” [2, 1].

However, modern generalized approaches kept the Nusselt number as an undefined function of Reynolds number, often a third- or fourth-degree polynomial, a spline, or another power law determined during calibration:

$$\mathrm{Nu} = f(\mathrm{Re}), \tag{2.7}$$

or written in terms of voltage and velocity using Eq. (2.4) and the definition of the Reynolds number as

$$\frac{E^2}{\lambda(T_w - T_a)} = f\left(\frac{U}{\nu}\right). \tag{2.8}$$

Collis and Williams [2] proposed a modification to King’s law in the form of

$$\mathrm{Nu}\left(\frac{T_f}{T_a}\right)^{-0.17} = A + B\mathrm{Re}^n, \tag{2.9}$$

where T_a is the freestream temperature of the fluid and T_f is the film temperature. This correction has been substantiated by experiments by Chevray and Tutu [10] and Abdel-Rahman et al. [11]

The lack of a closed relation between the flow velocity and measured voltage means that in practice the probes always need to be calibrated before measurements.

2.2. Effect of fluid temperature in Hot-Wire Anemometry

The ultimate goal of Hot-Wire Anemometry is to extract the velocity of the fluid from the measured voltage of the anemometer. However, Section 2.1.2 showed that the heat transfer of the wire is dependent both on the flow speed and the flow temperature. This makes it impossible to discern an increase of fluid velocity from a drop of fluid temperature just from the hot-wire voltage. HWA is often used in applications with changing fluid temperature – sometimes undesirably as in open-loop or non-climate-controlled wind tunnels, and sometimes due to the nature of the experiment itself [12]. Therefore, the effects due to changes of fluid temperature do need to be accounted for in most real test conditions.

The most accurate method is always a direct calibration of the relation between anemometer voltage, flow velocity, and temperature, in other words $E = f(U, T_a)$. However, simultaneous calibration for velocity and temperature requires the use of a dedicated calibration facility, adding additional complexity and cost, as well as more time consumed by each calibration process.

Instead, the most common approach is to attempt to separate the effect of fluid temperature and velocity by assuming that their influence on heat transfer is independent of each other. In order to accomplish this, it is convenient to introduce the equivalent voltage E^* and the equivalent velocity U^*. Defining E^* as the voltage that would be read by the anemometer subjected to a fluid of the same Reynold's number, but at a reference fluid temperature T_a^*, Eq. (2.8) can be rewritten to

$$\frac{E}{\sqrt{\lambda(T_w - T_a)}} = f\left(\frac{U}{\nu}\right) = \frac{E^*}{\sqrt{\lambda^*(T_w - T_a^*)}}, \tag{2.10a}$$

where λ^* is the heat conductivity of the fluid at the reference temperature. After solving for E^*,

$$E^* = E\sqrt{\frac{\lambda^*(T_w - T_a^*)}{\lambda(T_w - T_a)}}. \tag{2.10b}$$

Correspondingly, U^* is the velocity of a fluid at the reference temperature T_a^* that would have the same Reynold's number as the actual fluid, so

$$\frac{U}{\nu} = \frac{U^*}{\nu^*} \tag{2.11a}$$

where ν^* is the kinematic viscosity at the reference temperature. Solving for U^*,

$$U^* = U\frac{\nu^*}{\nu}. \tag{2.11b}$$

The reference fluid temperature can be chosen freely, but it is often taken as the mean freestream temperature during calibration. The temperature-independent hot-wire velocity calibration is then performed for the equivalent velocity U^* and voltage

E^* as

$$U^* = f(E^*). \tag{2.12}$$

The simplest approach to correct the measured hot-wire voltage for temperature drift of the fluid is to assume that the change of fluid properties λ and ν is negligible. In other words,

$$E^* = E\sqrt{\frac{T_w - T_a^*}{T_w - T_a}}, \tag{2.13}$$

and $U^* = U$. Consequently, $U = f(E^*)$. This simple correction was recommended by Bearman [1] when the changes in flow temperature are small relative to the difference between wire and flow temperature, and further reinforced for relatively large flow temperature variations through experimental validation by Pessoni and Chao [13] and Ball et al. [14]. Abdel-Rahman et al. [11] has also shown this formula to work well, but only for flow velocities above $4\,\mathrm{m\,s^{-1}}$.

A more accurate method takes into account the change in the heat conductivity and the kinematic viscosity, and both the velocity and voltage are corrected during calibration using the full Eqs. (2.10b) and (2.11b). The fluid properties λ and ν are typically calculated at the film temperature T_f [2], defined as

$$T_f = \frac{T_w + T_a}{2}. \tag{2.14}$$

In this case, λ^* and ν^* are calculated at the reference film temperature $T_f^* = \frac{1}{2}(T_w + T_a^*)$. On the other hand, a study by Lundström et al. [15] suggested that the freestream fluid temperature T_a is a better reference for a temperature-independent caliberation of hot-wires with constant wire temperature, in which case λ^* and ν^* are also calculated at T_a^*.

To recover the fluid temperature from measurements, the voltage is corrected using Eq. (2.12), and the equivalent velocity is recovered from the calibration function. The real velocity is then calculated by inverting Eq. (2.11b).

Finally, if the additional factor proposed by Collis and Williams from Eq. (2.9) is included, the equivalent voltage can be defined through an analysis similar to Eqs. (2.10a) and (2.10b) as

$$E^* = E\sqrt{\frac{\lambda^*(T_w - T_a^*)}{\lambda(T_w - T_a)}\left(\frac{T_f T_a^*}{T_a T_f^*}\right)^{-0.17}}. \tag{2.15a}$$

However, since $(T_f^*/T_a^*)^{-0.17}$ is a non-dimensional constant close to unity, it can instead be defined for convenience as

$$E^* = E\sqrt{\frac{\lambda^*(T_w - T_a^*)}{\lambda(T_w - T_a)}\left(\frac{T_f}{T_a}\right)^{-0.17}}. \tag{2.15b}$$

If the effect of temperature on λ is not taken into account, Eq. (2.15b) can be reduced to

$$E^* = E\sqrt{\frac{T_w - T_a^*}{T_w - T_a}\left(\frac{T_f}{T_a}\right)^{-0.17}}. \tag{2.16}$$

In the end, there is a disagreement on the recommended temperature correction scheme for HWA. While some authors have recommended the Collis & Williams correction factor and calculating λ and ν at the film temperature [2], others omitted the additional correction factor while calculating λ and ρ either at the film temperature [16], or at the freestream temperature [15]. Furthermore, many studies reported sufficient accuracy while neglecting both the change in fluid properties and the additional correction factor under large temperature changes [11, 13, 14, 17]. Additionally, no comprehensive comparative study between all of these approaches appears to exist.

2.2.1. A note on the hot-wire temperature ambiguity

It is historically common to calculate the temperature of the hot-wire based on the measured resistance. The resistance-temperature of both tungsten and platinum can reliably be described with the linear relation

$$\frac{R_w(T)}{R_w(T^*)} = 1 + \alpha_{T^*}(T - T^*). \tag{2.17}$$

By applying Eq. (2.17) to Eq. (2.13), the simple correction can be written as

$$E^* = E\sqrt{\frac{R_w|_{T_w} - R_w|_{T_a^*})}{R_w|_{T_w} - R|_{T_a}}}. \tag{2.18}$$

This equation is enticing, as one does not need to know T_w. The hot resistance would then directly be known to the operator from the setting of the anemometer. The cold resistance of the probe could be measured at different ambient temperatures and used to fill in the other factors.

However, Van Dijk [18] deemed this method too unreliable, as the material properties can vary from wire to wire, with no possible standard temperature coefficient of resistance. Furthermore, another hidden inaccuracy in the resistance method was noted, as there will be a difference in the contact and internal instrument resistances between the operational CTA and the measurement at cold temperatures, Δ_1. To account for that, Eq. (2.18) was rearranged in the form

$$E^* = E\sqrt{\frac{R_{total}(T_w) - R_{total,cal}(T_a^*) + \Delta_1}{R_{total}(T_w) - R_{total,cal}(T_a) + \Delta_1}}, \tag{2.19}$$

where R_{total} are the total real cold resistances of the probe and all additional wire and contact resistances, and $R_{total,cal}$ are measured during temperature calibration.

Van Dijk has experimentally shown that if Eq. (2.18) is used, the lack of accounting for the resistance accuracy leads to the calibration data not collapsing on a single curve as expected. He proposed treating Δ_1 as a free parameter, and optimizing it until the χ^2 of a fourth-degree polynomial fit of the corrected data is minimum. The RMS-deviation of the polynomial fit of the data corrected with the optimized Δ_1 was reduced by an order of magnitude compared to Eq. (2.18).

Similarly, Van Dijk was the first to suggest abandoning the idea of calculating the hot-wire temperature from measured resistance or the overheat ratio, and instead

treating T_w in Eq. (2.13) as a free parameter to optimize. As long as a collection of measurements at a sufficient range of fluid temperatures is available, the correction can be applied to the data with a guessed value of T_w, and a fourth-degree polynomial $U = f(E^*)$ fitted to the entire set of data. Then T_w can be optimized until the χ^2 statistic is minimum. Van Dijk has found that this method allows for complete elimination of the uncertainty in hot-wire temperature that comes from estimating it through resistance. In his experiments, the post-calibration RMS-deviation is just $5.6\,\mathrm{cm\,s^{-1}}$, although the temperature span in his experiment was only around $6\,\mathrm{K}$.

Such approach can also be used for more complex relations including the effect of film temperature on the fluid properties λ and ν, as recently independently proposed by Takahashi et al. [19]. In this case, the optimized T_w is incorporated in the calculation of the film temperature, which is subsequently used to calculate the fluid properties.

2.3. X-wire Calibration

Multi-wire probes make use of multiple differently inclined wires to measure more than one velocity component. A schematic representation of an X-wire probe is shown in Fig. 2.3. The underlying principle of X-wire measurements is that a unique pair of flow velocity U and inclination angle ϕ should be linked to a unique pair of measured wire voltages E_1 and E_2. Many methods involving the deduction of flow speed and direction based in physical reasoning effective cooling velocity have been proposed and remain in use [20, 21], most notably the effective velocity methods discussed in Section 2.3.1, although they are often regarded as only somewhat accurate for at most $\pm 15°$ flow inclination. Over time, methods involving calibration look-up tables as described in Section 2.3.2 have been suggested instead. Another popular alternative aiming to improve the efficiency of data interpretation is the direct fitting method, elaborated on in Section 2.3.3.

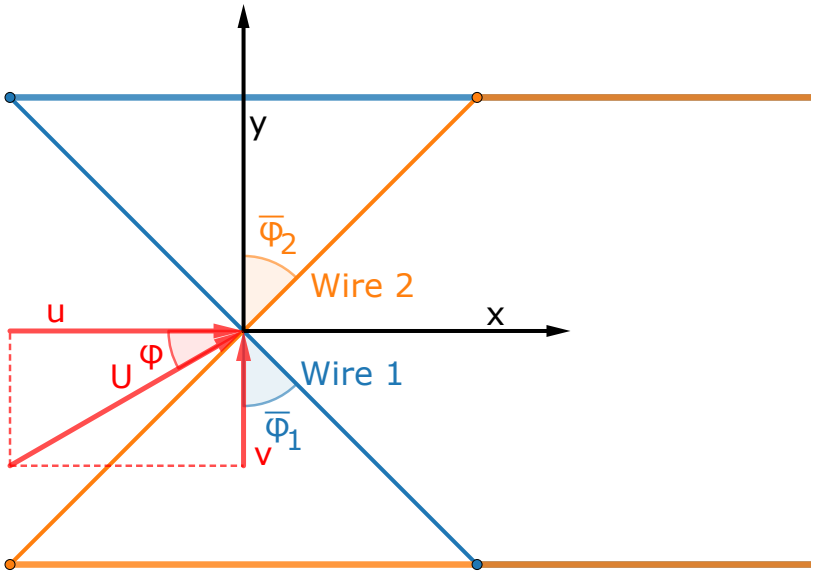

Figure 2.3: Schematic of an X-wire probe showing the velocity component definition

2.3.1. Effective velocity methods

Because of the underlying principle of multi-wire probes, it is no longer possible to assume that the flow is oriented perpendicular to the wires. Therefore, it is common to express the cooling relations as derived in Section 2.1.2, in terms of the effective cooling velocity U_e, which is a fictitious velocity magnitude that corresponds to the magnitude of a velocity vector aligned normal to the wire that would cause the same cooling of the wire as the real velocity vector U. The coordinate system of a single-wire probe can be defined as shown in Fig. 2.4.

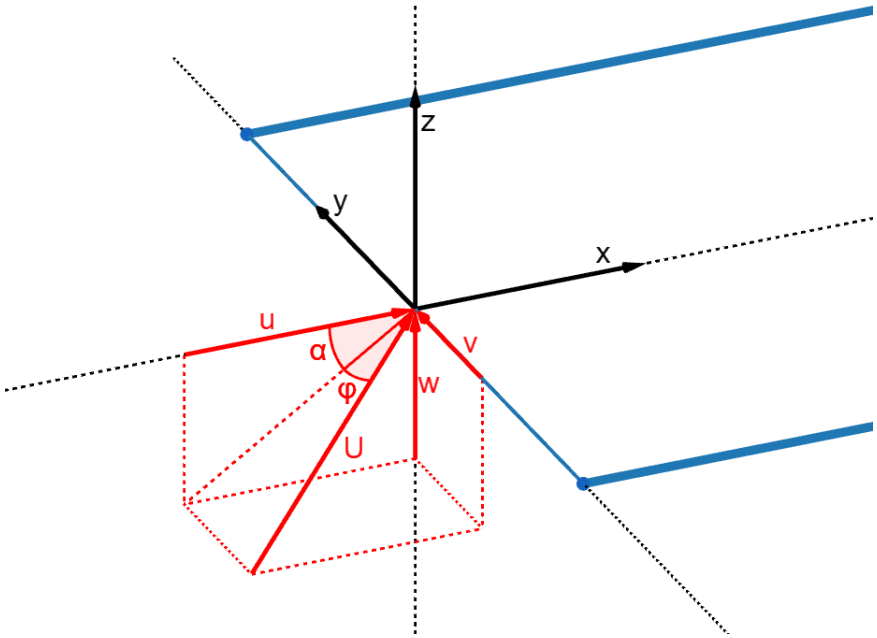

Figure 2.4: Velocity components in the sensor reference frame

The simplest approximation of off-angle cooling of a hot-wire is through the use of the cosine-cooling law:

$$U_e^* = U^* \cos\phi. \tag{2.20}$$

This is based on the assumption that only the wire-normal velocity component contributes to the convective heat transfer of the hot-wire. Real hot-wires do not show good agreement with this law. As an attempt to account for deviations from the cosine-cooling law, the law was expressed by Bradshaw [22] in terms of the effective yaw angle ϕ_e as

$$U_e^* = U^* \cos\phi_e. \tag{2.21}$$

The effective yaw angle is no longer the real angle between the velocity vector and the wire, and is instead found by fitting to calibration data.

As an attempt to better capture the effect of wire-parallel velocity components, Hinze [23] proposed including the effect of the wire-tangential velocity with the yaw parameter k:

$$U_e^{*2} = U^{*2}(\cos^2\phi + k^2 \sin^2\phi). \tag{2.22}$$

Others further expanded that approach by noting that the presence of the hot-wire prongs alter the flow field locally such that the response of the wire to the normal

velocity u and the bi-normal velocity w is in fact different, and better captured by

$$U_e^{*2} = u^{*2} + (kv^*)^2 + (hw^*)^2, \tag{2.23}$$

where k and h are the sensor's sensitivity coefficients in yaw and pitch. Equation (2.23) is often referred to as Jørgensen's law [5, 24, 18]. For typical hot-wire configurations, $k \approx 0.2$ and $h \approx 1.05$ [5], meaning that the sensitivity of the probe to the normal and bi-normal velocity components is very similar, and much higher than to the parallel component.

The effective velocity methods applied to X-wire calibration make use of individual fitted functions for $U^*_{e,1}(E^*_1)$ and $U^*_{e,1}(E^*_2)$, which can be based on King's-law-like relations or for example fourth-degree polynomial fits. According to Jiménez et al. [20], the effective cooling velocity of each wire can be described in the coordinate system from Fig. 2.3 using the cosine law as modified by Bradshaw with the effective yaw angle of each wire:

$$U^*_{e,1} = u^* \cos\bar{\phi}_{1,e} + v^* \sin\bar{\phi}_{1,e} \tag{2.24a}$$

and

$$U^*_{e,2} = u^* \cos\bar{\phi}_{2,e} - v^* \sin\bar{\phi}_{2,e}. \tag{2.24b}$$

The effective yaw angles $\bar{\phi}_{1,e}$ and $\bar{\phi}_{2,e}$ are similar to the real wire inclination angles $\bar{\phi}_1$ and $\bar{\phi}_2$, but are fitted to the data and are slightly different.

Equations (2.24a) and (2.24b) can be rearranged to

$$\frac{U_{e,1^*}}{\cos\bar{\phi}_{1,e}} = u^* + v^* \tan\bar{\phi}_{1,e} = f(E^*_1) \tag{2.25a}$$

and

$$\frac{U^*_{e,2}}{\cos\bar{\phi}_{2,e}} = u^* - v^* \tan\bar{\phi}_{2,e} = g(E^*_2), \tag{2.25b}$$

where functions $f(E^*_1)$ and $g(E^*_2)$ are fourth-degree polynomial fits, calculated from calibration data with flow aligned with probe axis ($v = 0$).

Angles $\bar{\phi}_{1,e}$ and $\bar{\phi}_{2,e}$ are found by inclining the probe to the flow during calibration by angle ϕ, so that $u^* = U^* \cos\phi$ and $v^* = U^* \sin\phi$. Then, with the assumption that yawing the probe by angle ϕ changes the effective cooling angle by the same amount, Eqs. (2.25a) and (2.25b) can be rewritten to

$$\cos\phi + \sin\phi \tan\bar{\phi}_{1,e} = \frac{f(E^*_1)}{U^*} \tag{2.26a}$$

and

$$\cos\phi - \sin\phi \tan\bar{\phi}_{2,e} = \frac{g(E^*_2)}{U^*}. \tag{2.26b}$$

The probe is yawed over a range of angles and $\bar{\phi}_{1,e}$ and $\bar{\phi}_{2,e}$ are regressed. From measurements, the velocity components are calculated using

$$u^* = \frac{f(E_1^*)\tan\bar{\phi}_{2,e} + g(E_2^*)\tan\bar{\phi}_{1,e}}{\tan\bar{\phi}_{1,e} + \tan\bar{\phi}_{2,e}} \tag{2.27a}$$

and

$$v^* = \frac{f(E_1^*) - g(E_2^*)}{\tan\bar{\phi}_{1,e} + \tan\bar{\phi}_{2,e}}. \tag{2.27b}$$

Alternatively, other effective cooling velocity expressions can be used, for example from Eq. (2.22) as

$${U_{e,1}^*}^2 = U^{*2}(\cos^2(\bar{\phi}_1 - \phi) + k_1^2\sin^2(\bar{\phi}_1 - \phi)) \tag{2.28a}$$

and

$${U_{e,2}^*}^2 = U^{*2}(\cos^2(\bar{\phi}_2 + \phi) + k_2^2\sin^2(\bar{\phi}_2 + \phi)). \tag{2.28b}$$

However, no direct solutions for U^* and ϕ exist, and the equations require solving iteratively.

2.3.2. Indirect methods

One of the first methods to avoid the inaccuracies of effective angle approach in multi-wire applications was developed by Willmarth and Bogar [25], who performed a full calibration of the probe on a grid of velocities and yaw angles, and recorded the response of the two wires at each combination. The data was interpreted during experiments through interpolation between the stored calibration points. A significant limitation of this approach is that the accuracy is limited by the density of the stored calibration grid. Furthermore, outliers in the calibration data could increase errors in their neighborhoods when using local interpolation schemes [18]. Initially, interpolation methods were introduced as a means to ”fill-in” relatively large gaps between calibration data in a more accurate manner than local interpolation directly from the calibration set, for example the following method by Lueptow et al.[3]. Another alternative was proposed by Browne et al. [26] and subsequently modified by Tropea et al. [4].

Lueptow method

In the approach described by Lueptow et al.[3], the initial relatively coarse calibration dataset is transferred to a finer rectangular $E_1^* - E_2^*$ grid by intermediate global polynomials fitted to the data. This also reduces the effect of individual bad samples during calibration. A typical X-wire calibration set has a range of velocities taken at the same probe yaw angles, such as the one shown in Fig. 2.5a. From this, polynomials $E_2^*(E_1^*)|_{\phi_i}$ and $U^*(E_1^*)|_{\phi_i}$ are fitted at each angle ϕ as shown for $E_2^*(E_1^*)|_{\phi_i}$ in Fig. 2.5b. Then, the values of E_2^* and U^* are evaluated at evenly spaced intervals of E_1^* for each angle using the fits, and new polynomials $\phi(E_2^*)|_{E_1^*}$ and $U^*(E_2^*)|_{E_1^*}$ are fitted for each

value of E_1^*, as shown symbolically in Fig. 2.5c. Finally, ϕ and U^* is evaluated from these functions at uniform intervals of E_2^*, as shown in Fig. 2.5d, leading to a uniform denser grid in E_1^* and E_2^*. U^* and ϕ are typically converted to u^* and v^*[3, 24] and stored. In this way, denser look-up tables could be generated.

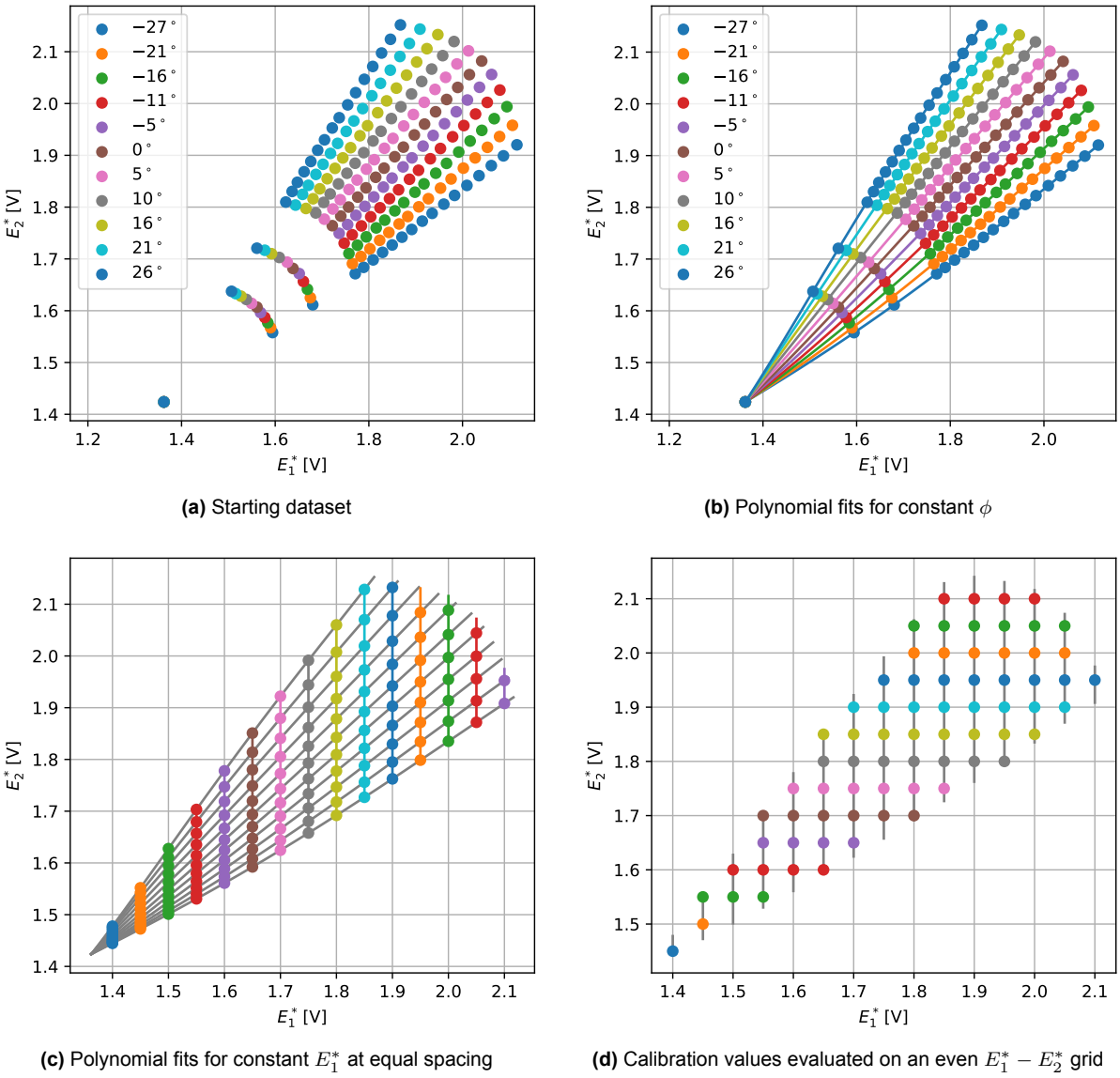

(a) Starting dataset

(b) Polynomial fits for constant ϕ

(c) Polynomial fits for constant E_1^* at equal spacing

(d) Calibration values evaluated on an even $E_1^* - E_2^*$ grid

Figure 2.5: Lueptow X-wire look-up table generation procedure

Figure 2.6 shows the 3D representation of the stored lookup table. For a measured pair of E_1^*, E_2^*, bilinear interpolation is used to find the corresponding u^* and v^*. The accuracy of the look-up table method depends on the spacing of the grid points.

For analyzing the accuracy of the Lueptow interpolation scheme itself, the method could be used as an indirect interpolation method, where only the original polynomial fits $E_2^*(E_1^*)|_\phi$ and $U^*(E_1^*)|_\phi$ are stored, and subsequent steps are repeated for each data inversion from measurement at exact values of E_1^* and E_2^*.

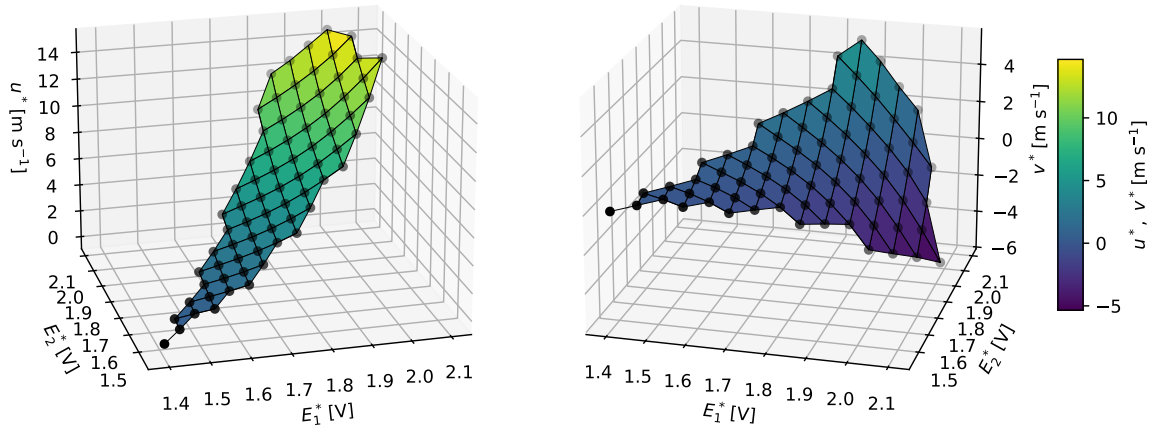

Figure 2.6: X-wire look-up table visualized

Browne method

The method proposed by Browne et al.[26] involves fitting fourth-degree polynomials $U^*\left(E_1^*\right)|_{\phi_i}$ and $U^*\left(E_2^*\right)|_{\phi_i}$ for every pitch angle ϕ_i. A representative calibration set with the fitted polynomials is shown in Fig. 2.7

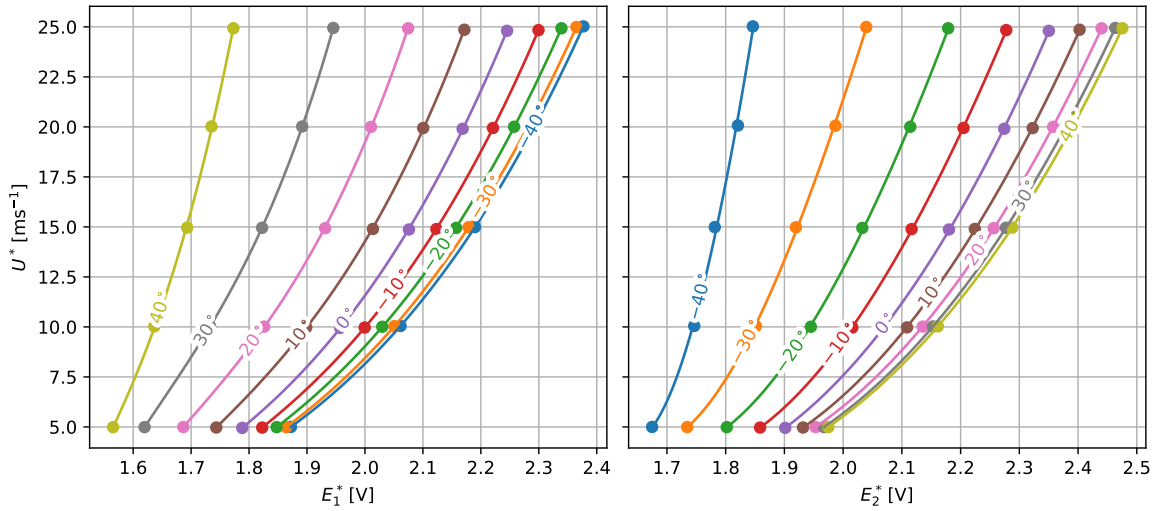

Figure 2.7: X-wire calibration set in Browne format

To retrieve the flow velocity and angle from a pair of measured voltages, the first step is to calculate the velocity corresponding to the voltage for each of the wires and each angle polynomial, as represented by the cyan points in Fig. 2.8.

Next, polynomial fits $U^*(\phi)|_{E_1}$ and $U^*(\phi)|_{E_2}$ are made for each wire at the given voltages, as shown in Fig. 2.9. The final value of the velocity and angle of the flow is read from the intersection of these two curves.

The disadvantage of the Browne approach was its difficulty in accurately inverting the data near the boundary of the calibration set.

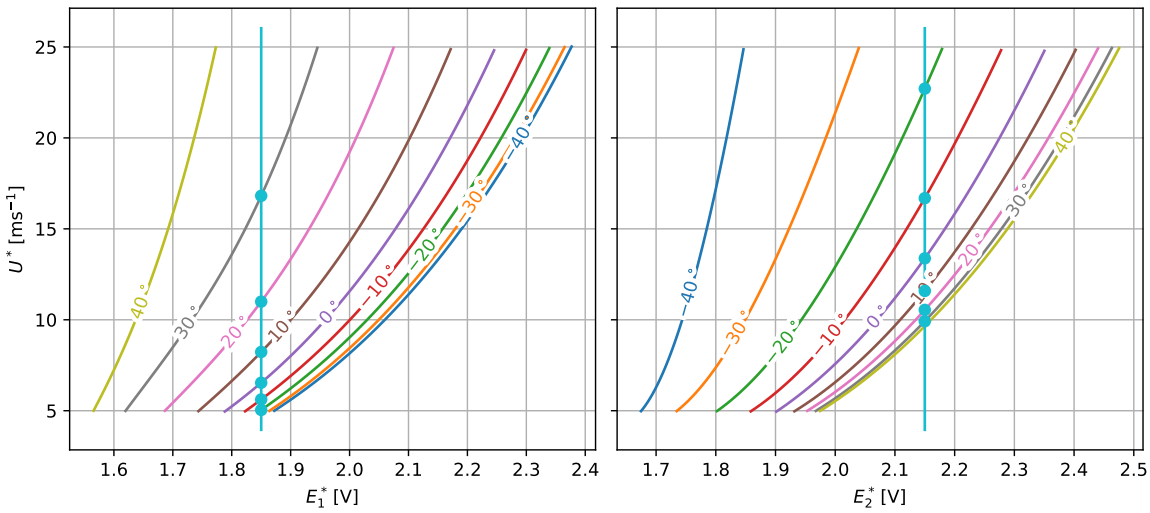

Figure 2.8: The first step of velocity and angle retrieval using the Browne method

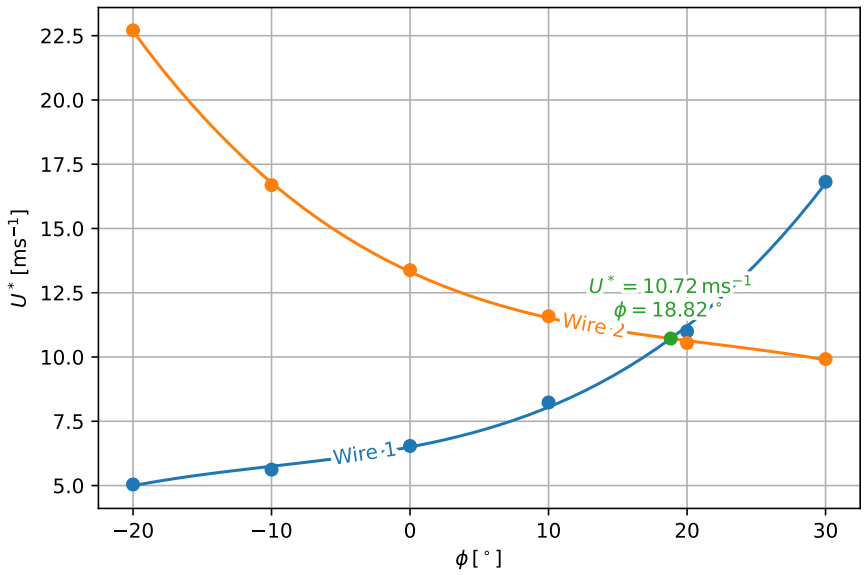

Figure 2.9: The second step of velocity and angle retrieval using the Browne method

Modified Browne method

Tropea et al. [4] made two adjustments to the Browne method. First, power laws inspired by King's law in the form

$$E_1^*(U^*)|_{\phi_i} = A_{1,i} + B_{1,i}(U^*)^{n_{1,i}} \tag{2.29a}$$

and

$$E_2^*(U^*)|_{\phi_i} = A_{2,i} + B_{2,i}(U^*)^{n_{2,i}} \tag{2.29b}$$

are regressed instead of polynomials for each angle ϕ_i . These can be easily inverted, and the intersection points for a given pair of E_1^* and E_2^* can be calculated as previously described.

Secondly, instead of fitting fourth degree polynomials for all intersections, the rough intersection point is found and a subset of points is used for fitting a lower degree polynomial. The suggested approach was to fit second-degree polynomials on three, or third-degree polynomials on the five points nearest to the intersection.

Unlike polynomials, the power law fits continue monotonously increasing outside the calibration domain in a stable manner for well-defined calibration data. Because of this, a further modification can be considered – instead of only finding intersections inside the calibration range, slight excursions from the domain can be considered for edge cases where there would otherwise not be enough intersections for subsequent fits.

The individual fits can be seen in Fig. 2.10. For a pair of voltages E_1^* and E_2^* indicated with black vertical lines in the figure, intersection points with all regressed curves are found, as plotted in the left side of Fig. 2.11. Then, after finding the angle closest to the intersection, the nearest points to that are selected, and polynomial fits are used to find the result as shown in the right side of the figure. The approximate intersection point can be found by subtracting the velocities calculated from each voltage at each angle and finding the change in sign. Intersections outside the calibration domain are only used if there is otherwise insufficient number of points for a subsequent fit.

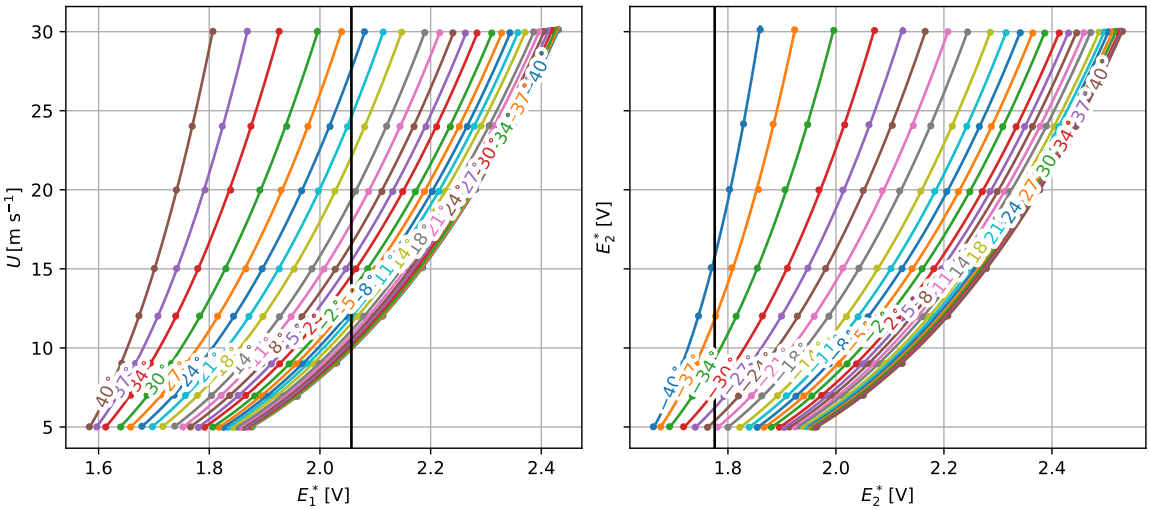

Figure 2.10: X-wire calibration set in Tropea format

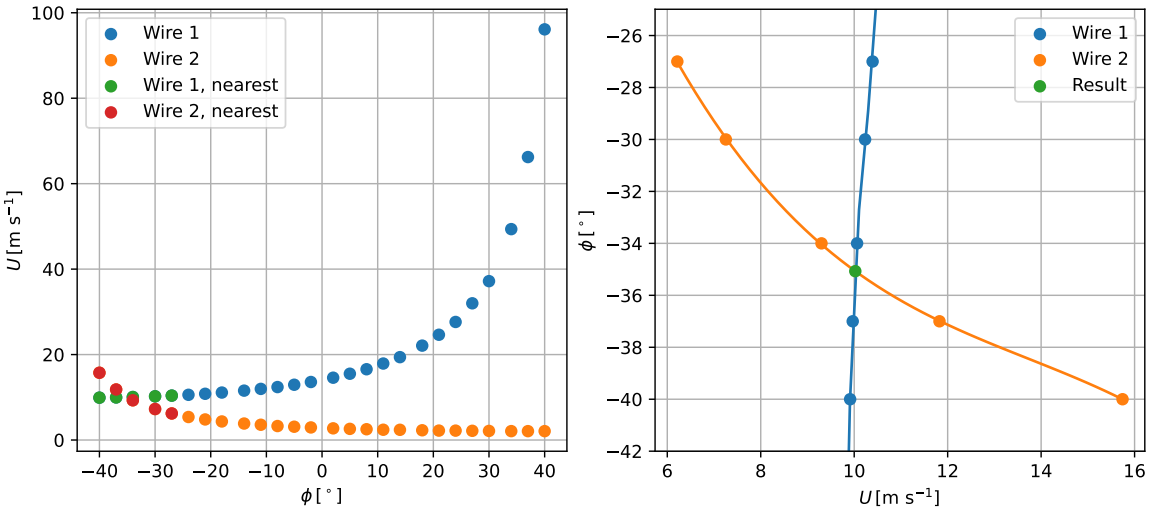

Figure 2.11: Retrieval of U and ϕ using the Tropea method

2.3.3. Direct methods

Since a unique relationship exists between a pair of voltages, and the flow magnitude and direction within the domain of interest of an x-wire, it was suggested to directly evaluate the flow variables from measured voltages.

Velocity magnitude and angle polynomials

One of the first to propose direct polynomial fitting of calibration data were Oster and Wyganski already in 1982[27]. The suggested approach consisted of using least-squares regression to directly fit two polynomial surfaces to the calibration data – $U^* = f(E_1^*, E_2^*)$ and $\phi = f(E_1^*, E_2^*)$. In the original work, third-degree expressions in the forms

$$U^* = \sum_{i=0}^{3} \sum_{j=0}^{3-i} \left(a_{ij} E_1^{*i} E_2^{*j} \right) \tag{2.30a}$$

and

$$\phi = \sum_{i=0}^{3} \sum_{j=0}^{3-i} \left(b_{ij} E_1^{*i} E_2^{*j} \right) \tag{2.30b}$$

were used.

Generally, fourth-degree polynomial expressions have generally been found to capture hot-wire calibration data better than third-degree, and so the fitted functions can be fourth-degree expressions instead:

$$U^* = \sum_{i=0}^{4} \sum_{j=0}^{4-i} \left(a_{ij} E_1^{*i} E_2^{*j} \right) \tag{2.31a}$$

and

$$\phi = \sum_{i=0}^{4} \sum_{j=0}^{4-i} \left(b_{ij} E_1^{*i} E_2^{*j} \right) . \tag{2.31b}$$

Velocity component polynomials

An alternative direct calibration approach involves the representation of calibration data in the two velocity components instead of U and ϕ:

$$u^* = U^* \cos \phi \tag{2.32a}$$

and

$$v^* = U^* \sin \phi \tag{2.32b}$$

Then, functions $u^* = f(E_1^*, E_2^*)$ and $v^* = f(E_1^*, E_2^*)$ are fitted to the calibration data. This variation can offer an advantage over the previously described U-ϕ method, since the hot-wire response to velocity might be better represented by a polynomial expression than to angle. This form was used by Chang & Blackwelder [28], and was more recently shown by Nguyen [29] to offer good measurement when using fourth-degree polynomial fits. However, no direct comparison to U-ϕ methods has been made.

3

Research framework

This chapter presents the reasoning behind the research by identifying the research gap in Section 3.1, defining the research objective in Section 3.2, formulating the research questions in Section 3.3, and finally outlining the approach used to answer them in Section 3.4.

3.1. Research gap

As underlined in Chapter 1, Hot-Wire Anemometry continues to find wide use in research today. This is also the case at the LSL, where they are an essential part of aerodynamics research. Despite the maturity of HWA, the brief overview of hot-wire measurement background in Chapter 2 has identified two main issues limiting its practical use:

- Temperature correction - literature disagrees on how to best decouple the effects of flow velocity and temperature on hot-wire readings. Researchers must choose between several correction schemes without a comprehensive cross-dataset comparison of their performance.
- Multi-wire calibration - there is a wide variety of models relating the voltage of multi-wire probes and the magnitude and direction of velocity. Yet, there is no comprehensive comparison of their accuracy or the required calibration grid resolution.

Additionally, at the LSL, there is a third major obstacle to multi-component velocity measurements using HWA: a lack of an existing universal calibration system. The existing setup requires removing the probe from the test setup, risking probe damage, misalignment, and loss of calibration accuracy, while at the same time consuming valuable wind-tunnel time.

Together, these gaps serve as a barrier to the use of HWA to obtain reliable HWA data in environments with multi-component velocity or with high temperature fluctuations.

3.2. Research objective

The goal of this research is to develop an automated in-situ calibration framework for X-wire Constant Temperature Anemometers, ensuring accurate and efficient calibration within restricted test environments such as small-scale wind tunnel test sections, and use it to evaluate the performance of calibration schemes.

This framework must:

- Operate directly in restricted wind-tunnel sections with minimal disturbance.
- Enable repeatable and efficient calibration for future LSL experiments.

3.3. Research questions

For the evaluation of calibration schemes, the main research question is

How can a two-wire constant-temperature anemometer be calibrated in-situ under variable flow temperature conditions while maintaining high measurement accuracy and reliability?

To aid in answering it, the following sub-questions can be posed:

1. Temperature correction
    - Can the effects of temperature and fluid velocity be effectively separated, or are more complex combined calibration methods required?
    - Does the change in fluid properties with temperature need to be taken into account, and if so which reference temperature (freestream or film) yields most consistent correction?
    - Is the Collis & Williams correction term required?
    - Can the wire temperature be calculated from the overheat ratio, or does it need to be optimized?
2. X-wire calibration
    - How do the different look-up and direct calibration methods compare in measurement error across a dense calibration grid?
    - What calibration grid resolution (velocity and angular spacing) is required for accurate calibration?

3.4. Research approach

To answer these questions, the analysis is divided into two chapters:

1. Temperature correction study, where 6 correction models with both optimized and estimated wire temperature are evaluated on datasets obtained from literature and a newly collected dataset spanning a wide temperature and velocity range.
2. X-wire calibration study:
    - Develop a new miniature and automated yaw calibration system

- Collect a high-density calibration grid
- Evaluate the accuracy of calibration methods
- Perform a grid resolution convergence study

4

Design of calibrators and experimental evaluation

The conducted research can be split in two separate main parts. First, the investigation of the different temperature correction methods as outlined in Section 4.1. Second, the comparison of X-wire calibration schemes as described in Section 4.2.

4.1. Temperature correction

Different temperature correction models (Bearman, Collis & Williams, direct evaluation of fluid properties) is evaluated using a combination of datasets from literature listed in Table 4.1.

Table 4.1: Overview of datasets used for evaluation temperature correction methods.

Dataset source	Temperature range	Velocity range
Pessoni & Chao [13]	$6\,\mathrm{m\,s^{-1}}$ to $30\,\mathrm{m\,s^{-1}}$	$21\,^{\circ}\mathrm{C}$ to $63\,^{\circ}\mathrm{C}$
Koppius & Trines [30]	$0.5\,\mathrm{m\,s^{-1}}$ to $5\,\mathrm{m\,s^{-1}}$	$10\,^{\circ}\mathrm{C}$ to $80\,^{\circ}\mathrm{C}$
Fiedler [31]	$2\,\mathrm{m\,s^{-1}}$ to $20\,\mathrm{m\,s^{-1}}$	$21\,^{\circ}\mathrm{C}$ to $50\,^{\circ}\mathrm{C}$
Artt & Brown [32]	$2.7\,\mathrm{m\,s^{-1}}$ to $14.8\,\mathrm{m\,s^{-1}}$	$18\,^{\circ}\mathrm{C}$ to $40\,^{\circ}\mathrm{C}$

In order to quantify correction effectiveness, the corrected data is fitted with fourth-degree direct polynomial fits $U^* = f(E^*)$, and used for the calculation of velocity from a measured voltage. The temperature correction step is inverted, and the real velocities U_m compared with U_c calculated from the fits. The goodness of fit can be described by the "normalized standard deviation" as described by Bruun et al. [5] and Wubben [24]:

$$\varepsilon_U = \sqrt{\frac{1}{N}\sum_{i=1}^{N}\left(\frac{U_c^{(i)} - U_m^{(i)}}{U_c^{(i)}}\right)^2}, \tag{4.1}$$

which is in fact the root mean square percentage error (RMSPE). In this equation, N is the total number of calibration points, and i denotes the specific calibration point.

For the purpose of collecting additional temperature correction data, a TSI model 112700 hot-wire calibrator unit was modified to include flow-heating capabilities with an AHP-3742 in-line air heater from Omega Engineering. The heater connected to a $230\,\mathrm{V}$ AC supply provides $200\,\mathrm{W}$ of heating power. The heater is controlled with a Selec TC544C-CE temperature controller with feedback from a T-type thermocouple placed in the settling chamber of the calibrator. The calibrator setup is connected to a filtered and regulated $0.4\,\mathrm{MPa}$ compressed air supply. To indirectly control the outlet velocity, two parallel manual needle valves are used, with one providing coarse and the other fine regulation. The flow velocity can be calculated by measuring the difference in pressure between the settling chamber of the calibrator and the ambient. The TSI calibrator is shown in Fig. 4.1.

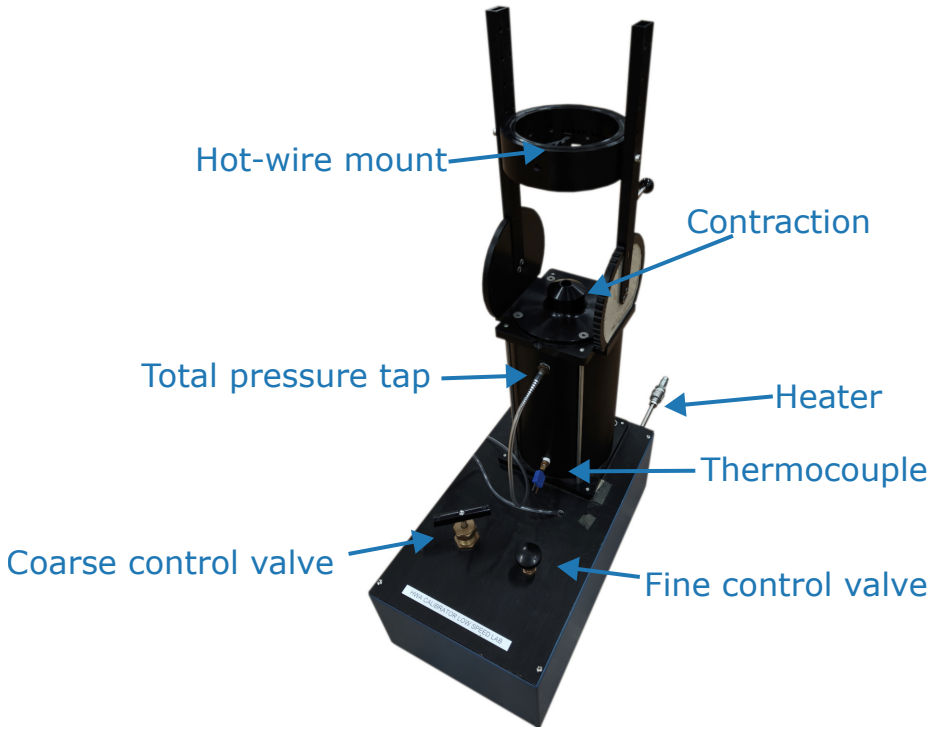

Figure 4.1: Hot-wire temperature calibrator

In the end, it was not possible to collect additional experimental data in time, and only the reference datasets obtained from literature are used for evaluation of temperature correction methods.

4.2. X-wire calibration

In this section, the design of the new X-wire calibration setup is described in Section 4.2.1 first, and the experimental methodology to collect the dataset for calibration scheme evaluation is described in Section 4.2.2.

4.2.1. Calibrator design

Previously, the calibration of multi-wire probes at the LSL was performed using the system shown in Fig. 4.2. The use of this calibrator forced the removal of the hot-wire

probe from the test setup that it was going to be used in, and re-installation after the calibration had been performed. This was a time-consuming process that further risked the accuracy of the hot-wire measurements in the experiment or physical damage to the fragile wires.

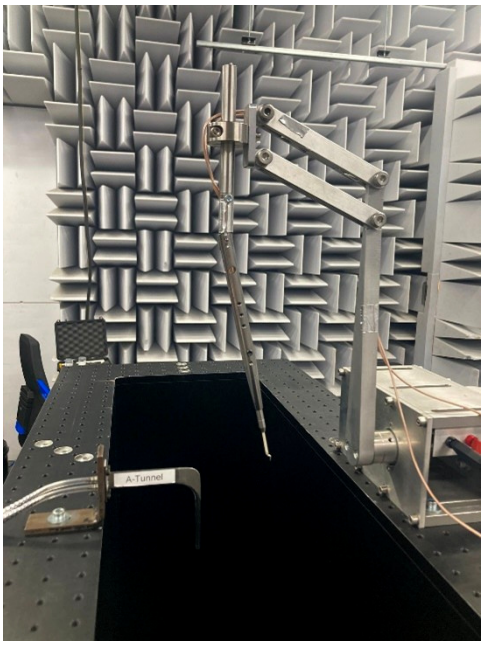

Figure 4.2: Old X-wire probe calibrator

Due to the importance of carefully controlled calibration on the validity of hot-wire measurements and the need for frequent recalibration, a new setup which would allow effortless calibration directly in the experiment setup was needed. This calibrator would also need to be easily adaptable to a variety of potential experiments performed at the LSL in different wind tunnel facilities. The research in turbulent transition of cooled boundary layers at the TU Delft [12] served as an example of a challenging application, as the hot-wire probes were inserted into a narrow test section of less than $5\,\mathrm{cm}$ in width on a long arm. Because of the restricted size of the test section, removal of the probe from the test section was previously necessary for calibration.

To make the calibrator universal, it was not possible to use an externally mounted pivoting system as in the old design. Instead the motion system needed to be integrated closer to the hot-wire probes. The motor powering the yaw mechanism of the probe had to be miniature, while maintaining sufficient holding torque to resist the aerodynamic forces and keep the probe firmly at the desired angle. Similar requirements for RC model airplanes' control surfaces have led to fairly powerful and inexpensive commercially available servo motors. For the calibrator, the Chaservo LV06 model was used. It was found to have low backlash, and had a quoted holding torque of $1.9\,\mathrm{kg\,cm}$ thanks to the combination of a high-quality DC motor and gearbox. This servo, shown in Fig. 4.3, was among the smallest available, and had a much higher torque output than other comparable models.

The precision demanded from RC components was not adequate for a precision calibration, and the positional accuracy was one of the specifications provided by the

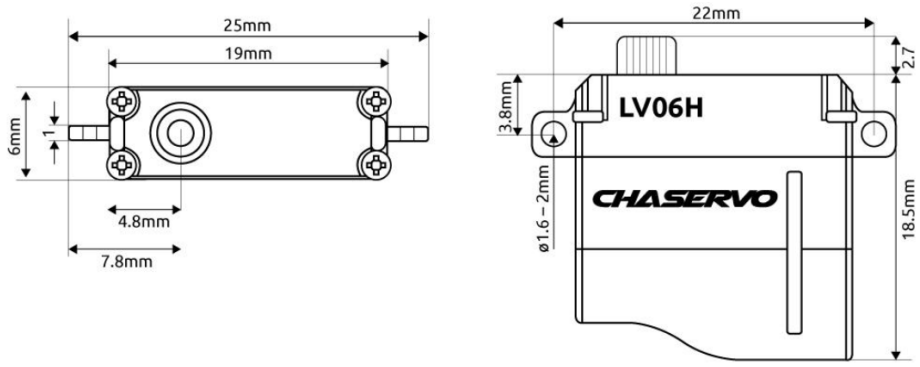

Figure 4.3: The dimensioned drawing of the Chaservo LV06 from the manufacturer

manufacturer. It was, however, estimated to be in the order of a few degrees by testing, which is insufficient for hot-wire calibration. Instead of the low precision potentiometer feedback from the servo, a more accurate source of angle measurement was needed. Magnetic rotary encoders are devices which can measure the angle of a special diametrically-magnetized magnet using the hall effect. Given relatively accurate alignment requirements between the magnet and the chip, the MagnTek MT6835 could offer accuracy of $\pm 0.5^\circ$ out of the box. The chip also supports programming of an user non-linearity compensation, which can bring the accuracy below $\pm 0.02^\circ$. However, no high-precision encoder was available at the time of this study to perform this, and it remained at the factory setting. Additional non-linearity compensation remains as a recommendation for future applications of the calibrator. The precision of this encoder is $< 0.0002^\circ$, which will allow the calibrator to match the target angles very well during calibration.

To maximize the accuracy of the encoder, the magnet needed to be aligned both with the axis of rotation and with the center of the chip. To ensure satisfactory alignment of the magnet with the servo, the magnet was positioned during the adhesion process using a milling machine with precise digital readout components with a positional accuracy of $< 0.01\,\mathrm{mm}$. The center of rotation of the servo was found using a $< 0.01\,\mathrm{mm}$ precision dial indicator rigidly mounted to the arm of the servo. A precision ground reference cylinder was mounted in the spindle of the milling machine. The arm of the servo was continuously rotated, and the bed of the milling machine was moved until the servo arm with the dial indicator ran true with the spindle of the mill (the needle did not move throughout the rotation). Figure 4.4 shows a picture taken during this process.

At that point, the position of the center of rotation of the servo was saved in the digital readout system of the milling machine, the dial indicator removed from the servo, and the reference cylinder removed from the spindle of the mill. One of the larger surfaces of the magnet was previously lightly sanded to remove some of the nickel plating while taking care to keep it flat and perpendicular to the axis of the magnet. The sanded magnet was gently placed in a $6\,\mathrm{mm}$ collet in the spindle of the milling machine, and touched to a precision ground part of the mill perpendicular to the spindle axis. Then, with the magnet aligned flat, the collet was lightly tightened, and moved back to the position of the servo's axis of rotation. Both the surface of the magnet and the servo

Figure 4.4: Locating the center of rotation of the servo

arm were cleaned with acetone. Then, a small drop of J-B Weld steel-reinforced epoxy adhesive was applied to the servo arm, and the magnet gently lowered onto the arm of the servo by moving the milling machine. Figure 4.5 shows a picture taken during curing of the epoxy adhesive, with the magnet partially visible in the collet above the servo.

After the epoxy was allowed a 24-hour curing period, the vice holding the servo was loosened. Afterwards, the bed of the milling machine was lowered away from the spindle, while making sure to avoid hitting the servo. With the servo clear from any obstacles the collet was loosened, and the servo with magnet removed. The servo shown in Fig. 4.6 was thus fitted with a diametrically-magnetized magnet, with $< 0.02\,\mathrm{mm}$ off-axis deviation.

For the alignment of the rotating magnet with the stationary encoder chip, an alignment piece made of acrylic is used. The detail view rendering of interface of the part is shown in Fig. 4.7. Looking on the image, the board with the encoder chip is mounted from the top side, and the chip fits snugly in the rectangular cutout in the alignment piece. The magnet sits in the circular cutout partially visible in the back of the part. The round cutout is machined to a close running tolerance with the diameter of the magnet, and the two cutouts are machined with high alignment to each other. The magnet side of the alignment piece is visible in Fig. 4.8, with the encoder chip visible in the cutout.

The calibrator assembly is shown in Fig. 4.9. The swinging part is highlighted in green. The angle of the final part of the hot-wire arm can be adjusted depending on the used probe, as the axis of rotation should be perpendicular to the plane formed by the wires.

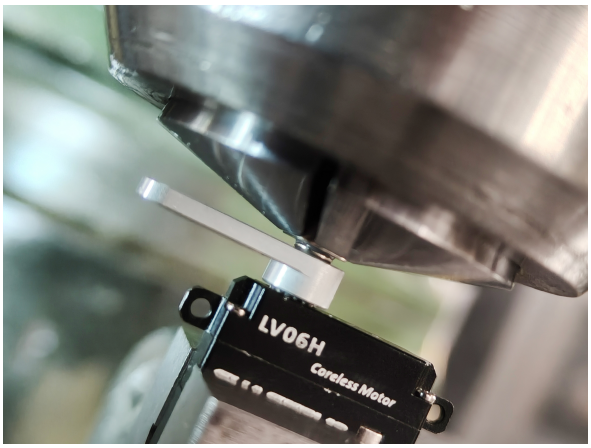

Figure 4.5: Adhesion of the magnet to the servo arm

Figure 4.6: Servo with the magnet aligned and adhered

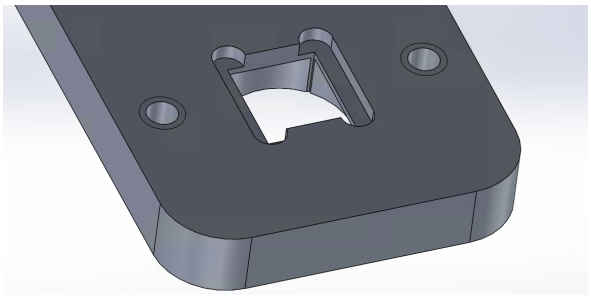

Figure 4.7: Magnetic encoder alignment piece closeup

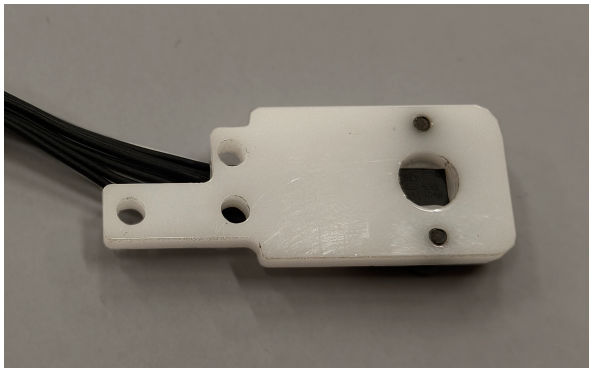

Figure 4.8: Magnetic encoder installed in the alignment piece

In the figure, the calibrator is shown in the configuration for a boundary layer V-shaped probe, whereas for an X-wire probe the arm would be kept straight. The manufacturing drawings of the calibrator components can be found in Chapter A.

The block diagram of the calibrator system is shown in Fig. 4.10. The calibration process is coordinated from a host computer running LabView, using the interface shown in Fig. 4.11. An Arduino Pro Micro type board acts as as a position controller between the magnetic encoder and the servo motor. The target angle is received from the host, and the position setting is sent to the servo motor via PWM. The target position of the servo is controlled through the reading from the magnetic encoder, which is also forwarded back to the host. The host also collects the data from the wind tunnel DAQ system and from the CTA bridges, and can control a traverse system. A sequence of points can be uploaded to the LabView script, which can proceed through the entire calibration domain automatically, sending the target commands to the separate controllers and waiting for the position to stabilize before logging the response and proceeding to the next point.

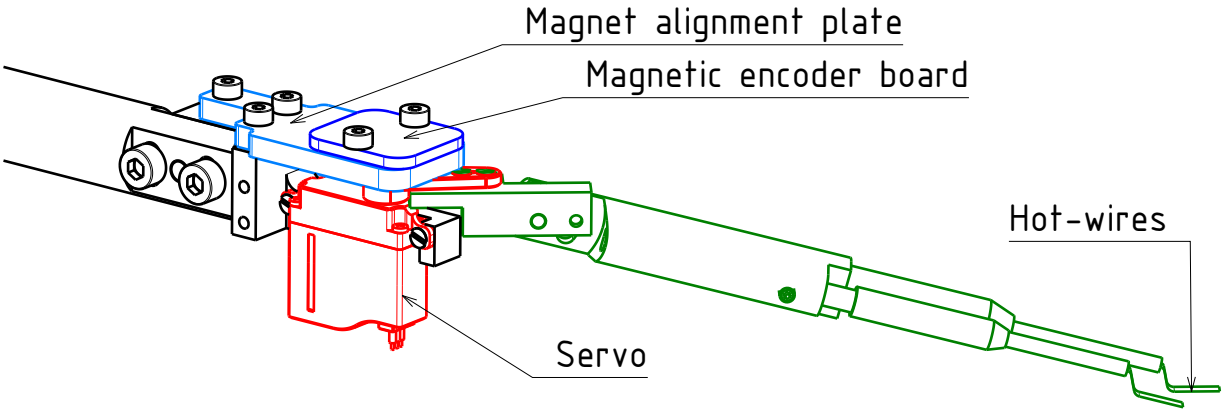

Figure 4.9: Schematic view of the calibrator

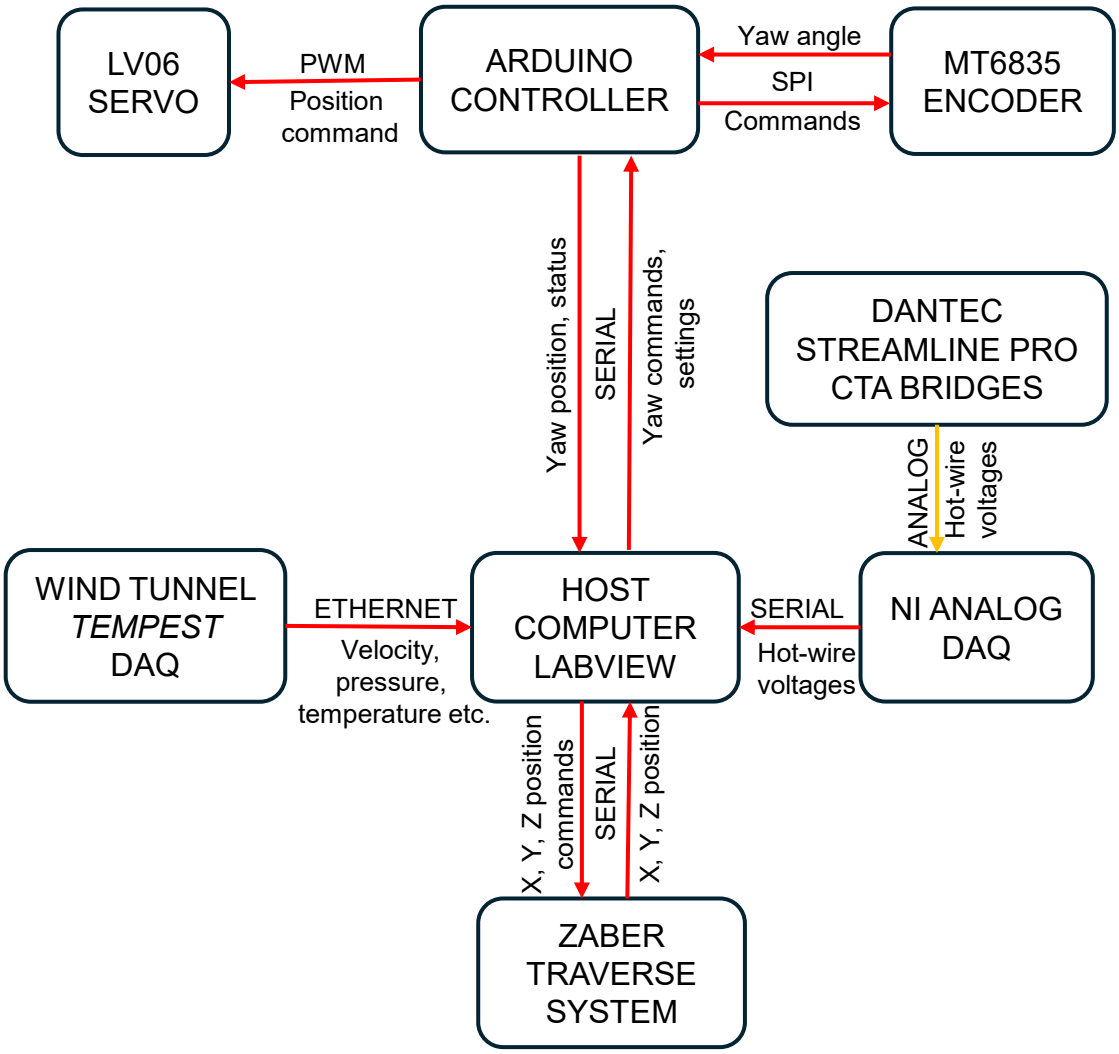

Figure 4.10: Block diagram of the calibrator system

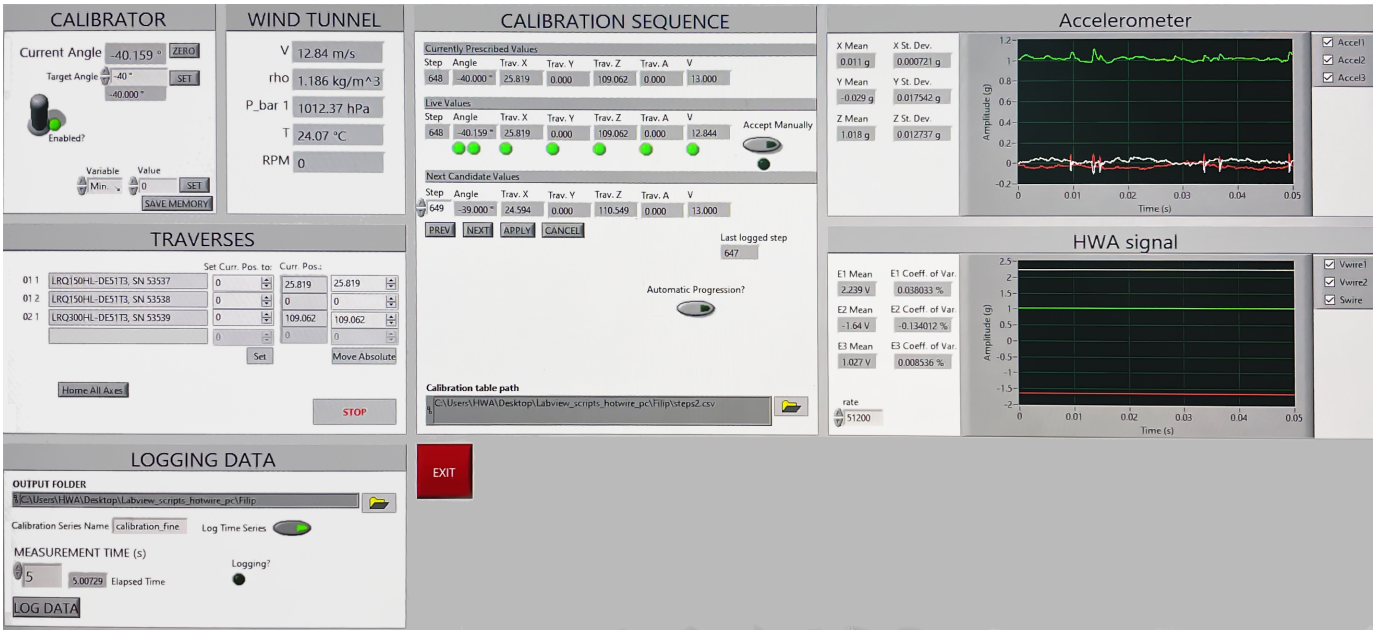

Figure 4.11: Calibrator LabView interface

4.2.2. Experimental evaluation

In order to facilitate robust verification of different interpolation schemes, the effect of calibration angle span, and convergence with respect to the calibration grid fineness, the X-wire response was measured on a fine $U - \phi$ grid. The wind tunnel velocity was varied in the range of $5\,\mathrm{m\,s^{-1}}$ to $30\,\mathrm{m\,s^{-1}}$ at steps of $1\,\mathrm{m\,s^{-1}}$, and the probe was yawed from $-40°$ to $40°$ at steps of $1°$. To decouple the variation of flow velocity and temperature, which would gradually increase during the measurement period, the velocity of the wind tunnel was changed in a random order. A set of angle measurements from $-20°$ to $20°$ with step of $2°$ at $26\,\mathrm{m\,s^{-1}}$ was repeated at multiple points during the long experiment duration to rule out any drift of probe properties.

Raw voltages were temperature-corrected, then transformed into velocity and angle fields using calibration relations. The primary performance metric for each calibration method was the modified RMSPE of the u^* and v^* velocity components, defined as

$$\varepsilon_u = \sqrt{\frac{1}{N}\sum_{i=1}^{N_i}\sum_{j=1}^{N_j^{(i)}}\left(\frac{u_c^{*(i,j)} - u_m^{*(i,j)}}{U_m^{*(i,j)}}\right)^2} \tag{4.2a}$$

and

$$\varepsilon_v = \sqrt{\frac{1}{N}\sum_{i=1}^{N_i}\sum_{j=1}^{N_j^{(i)}}\left(\frac{v_c^{*(i,j)} - v_m^{*(i,j)}}{U_m^{*(i,j)}}\right)^2}, \tag{4.2b}$$

where similar to Eq. (4.1) the subscript c indicates the value calculated from the voltage by the calibration method and m the measured value. N is the total number of calibration points, N_i is the number of angle steps, and $N_j^{(i)}$ is the number of velocity steps at the angle step ϕ_i. This metric is similar to the one used for evaluation of temperature correction for a single-wire probe from Eq. (4.1), and was proposed by Wubben [24], since the normalization of errors by v is impossible due to passing through 0.

The calibration set was collected using the 55P51 X-wire probe manufactured by DANTEC Dynamics. This probe had gold-plated tungsten wires with length of approx. $1\,\mathrm{mm}$ and diameter of $5\,\mu\mathrm{m}$. The probe was connected to a DANTEC Streamline Pro CTA module, with target $T_w = 242.223\,°\mathrm{C}$. The angle of the probes during calibration was measured with the built-in magnetic encoder, with a worst-case error of $\pm 0.5°$. The precision of the encoder was roughly $1.7e-4°$ and the measurement repeatability seemed to be similar. The calibrator was mounted on a sting inserted from the downstream side into the test section of the M-tunnel facility of the LSL, which is an open wind-tunnel with a square $0.4\,\mathrm{m}$ test section and a maximum speed of $35\,\mathrm{m\,s^{-1}}$.

The temperature of the flow was measured in the settling chamber of the wind-tunnel by a P-L-1/3-3-50-M6-PS-6 Pt100 probe from Omega with an accuracy above $\pm 0.11\,°\mathrm{C}$ in the relevant temperature range, read by the MAX31865 analog-to-digital converter. The absolute pressure was measured using a Bosch Sensortec BMP280 digital barometer with an accuracy of $\pm 0.50\,\mathrm{hPa}$. The facility was equipped with an array of the 2.5MD, 002ND, and 005ND Honeywell TruStability RSC differential pressure sensors

connected to the total pressure in the settling chamber, and the static pressure after the contraction. The sensor with the lowest range was automatically chosen based on the wind tunnel conditions, providing an accuracy and total error bound of $\pm 0.5\,\mathrm{Pa}$ and $\pm 2.5\,\mathrm{Pa}$ up to $q = 250\,\mathrm{Pa}$, $\pm 1\,\mathrm{Pa}$ and $\pm 5\,\mathrm{Pa}$ up to $q = 497.7\,\mathrm{Pa}$, and $\pm 2.5\,\mathrm{Pa}$ and $\pm 12.4\,\mathrm{Pa}$ up to $q = 1244.2\,\mathrm{Pa}$. Since the total error bound is listed for the full temperature range of the sensor, and the experiment was conducted around room temperature, the thermal effects should have been minimal and the error should have been closer to the quoted accuracy.

In addition, a single 005ND differential pressure sensor with an accuracy of $\pm 2.5\,\mathrm{Pa}$ and total error bound of $\pm 12.4\,\mathrm{Pa}$ was connected to a pitot tube positioned near the hot-wires. A close-up picture of the calibrator and the pitot tube can be seen in Fig. 4.12.

Figure 4.12: Calibrator and pitot tube in the M-tunnel of the LSL

The sting with the calibrator was mounted on a traverse system to allow full three-axis positional control, which was used to keep the center of the X-wire probe stationary. A picture of the complete setup can be seen in Fig. 4.13.

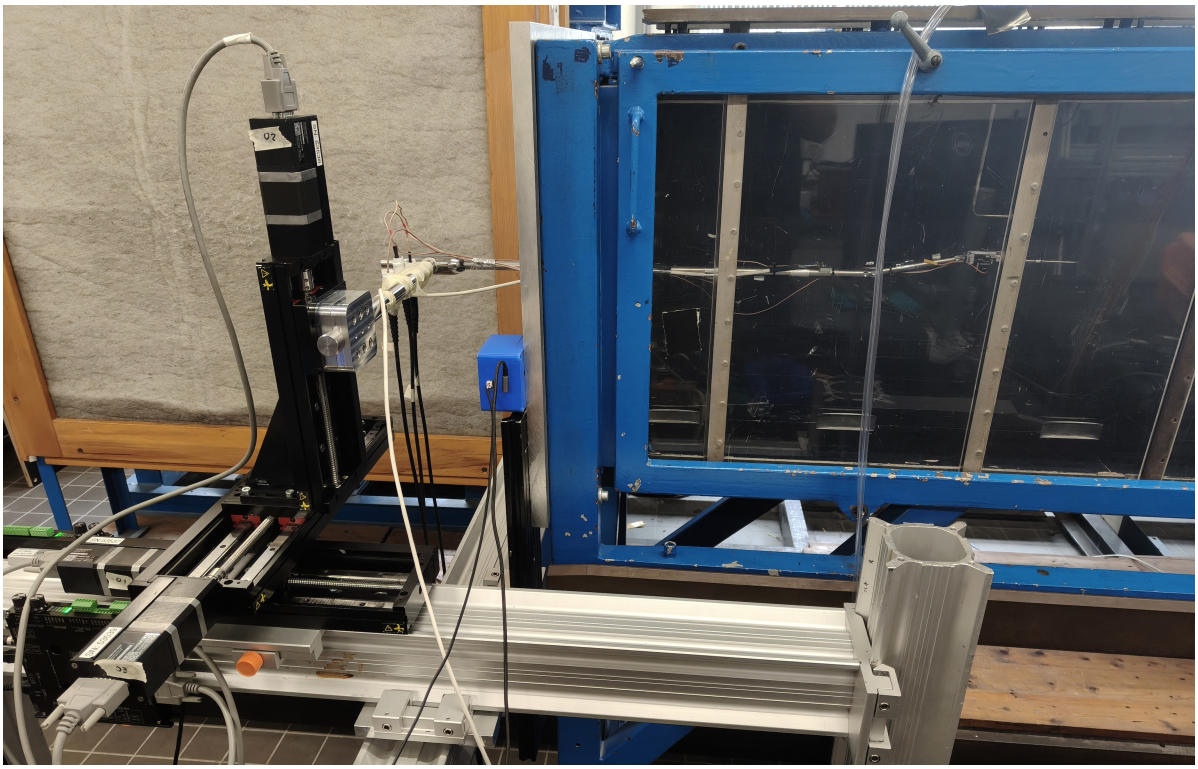

Figure 4.13: Traverse setup in the M-tunnel of the LSL

5

Results of calibration evaluation

This chapter presents the results of the evaluation of the hot-wire calibration methods. The results are split for the first study on fluid temperature correction in Section 5.1 and the second part on X-wire calibration in Section 5.2.

5.1. Temperature correction

Based on Section 2.2, six different temperature correction schemes were compared. These were split based on the reference temperature which was used for voltage and velocity correction, denoted as T_w (wire temperature), T_a (freestream temperature), and T_f (film temperature). T_w means that the change of fluid properties was neglected, and T_a or T_f mean that the fluid kinematic viscosity ν and the thermal conductivity λ were calculated at the freestream or film temperature of the fluid respectively. Furthermore, the application of the Collis & Williams correction term $(T_f/T_a)^{-0.17}$ was indicated with the abbreviation C&W. Thus, for example, for a correction labelled '$T_x, \mathrm{C\&W}$', where T_x is T_a or T_f, the corrected hot-wire voltage was

$$E^* = E\sqrt{\frac{\lambda_x^*(T_w - T_a^*)}{\lambda_x(T_w - T_a)}\left(\frac{T_f}{T_a}\right)^{-0.17}}, \tag{5.1}$$

and the velocity was

$$U^* = U\frac{\nu_x^*}{\nu_x}, \tag{5.2}$$

where λ_x and ν_x were calculated at the temperature T_x of each measurement, and λ_x^* and ν_x^* were calculated at the reference temperature T_x^*, taken as the mean from all the measurements. On the other hand, if $T_x = T_w$, the correction for the voltage was

$$E^* = E\sqrt{\frac{T_w - T_a^*}{T_w - T_a}} \tag{5.3}$$

and the velocity was unaltered, i.e. $U^* = U$.

The heat conductivity was calculated using the relation by Kannuluik & Carman [33]:

$$\lambda[\mathrm{W\,m^{-1}\,K^{-1}}] = 418.4(0.0000575(1 + 0.00317(T[^\circ\mathrm{C}]) - 0.0000021(T[^\circ\mathrm{C}])^2)) \tag{5.4}$$

The kinematic viscosity was calculated as $\nu = \mu/\rho$, where the dynamic viscosity μ was calculated using the Sutherland law

$$\mu[\mathrm{Pa\,s}] = 0.00001716 \left(\frac{T[\mathrm{K}]}{273}\right)^{3/2} \frac{273 + 110.4}{T[\mathrm{K}] + 110.4} \tag{5.5}$$

and the density ρ from the Ideal Gas Law $\rho = \frac{p}{RT}$.

For the purpose of the analysis, fourth-degree polynomials in the form $U^* = \sum_{i=0}^{4} c_i E^{*i}$ were fitted to the corrected data using the least-squares method. The correction schemes were evaluated both using the reported overheat ratio (if available) and with T_w optimized as a free parameter optimized in the least-squares method. As T_w was changed, this was also reflected in the calculation of the film temperature during temperature correction.

As an example, the raw measurements by Pessoni & Chao [13] and fits for all variations of correction scheme are shown in Fig. 5.1. The hot-wire temperature used is indicated in the legends, where $T_w = 461.15\,\mathrm{K}$ is based on the value reported in the source paper, and the other values were found by optimization.

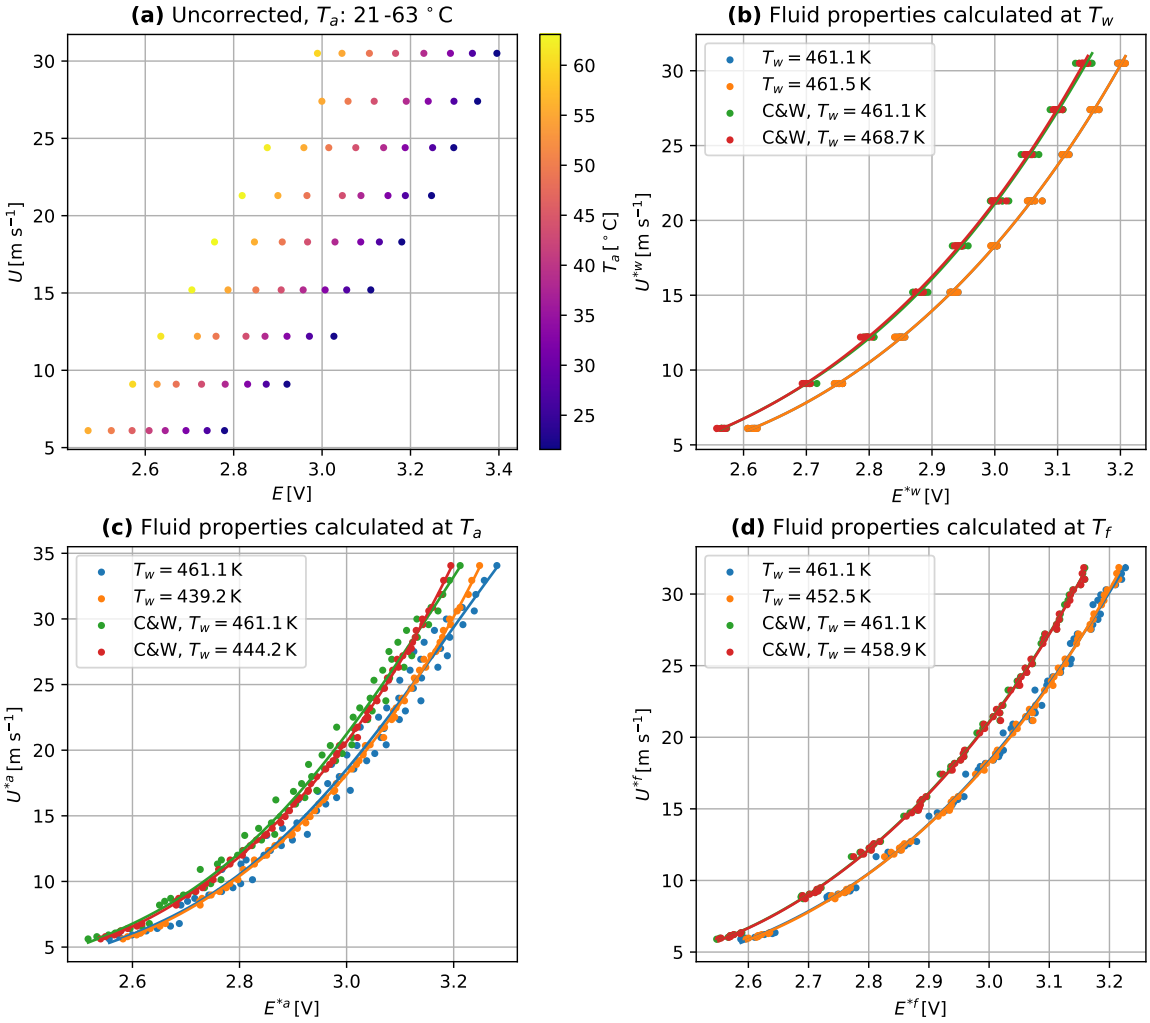

Figure 5.1: Temperature correction comparison for the data from Pessoni & Chao [13]

5.1.1. Comparison of temperature correction methods

First, for best-case scenario for each correction method, the correction schemes are compared in Fig. 5.2 with only optimized T_w. The data is grouped on the x axis by dataset, and colored by the correction scheme. Judging by the relatively similar values of the RMSPE for a given dataset, on first glance the methods can perform similarly if T_w is optimized. Also the Collis & Brown correction term does not seem to have an effect on the attainable accuracy of velocity. The exception is the high errors of the T_a methods in the Koppius & Trines measurements. From these four datasets, T_a methods seem to either be either slightly better (slightly lower error levels in the Artt & Brown, Fiedler, and to a lesser extent Pessoni & Chao), or significantly worse as in the Koppius & Trines dataset. Because of this inconsistency, they do not seem to be a good candidate for temperature correction.

Finding the optimal value of T_w requires a calibration set spanning a sufficiently wide freestream temperature range, so it might not always be possible. Figure 5.3 shows the RMSPE in velocity for corrections based on the reported T_w estimated from the overheat of the wire. The Fiedler dataset is not included, as the overheat of the wire

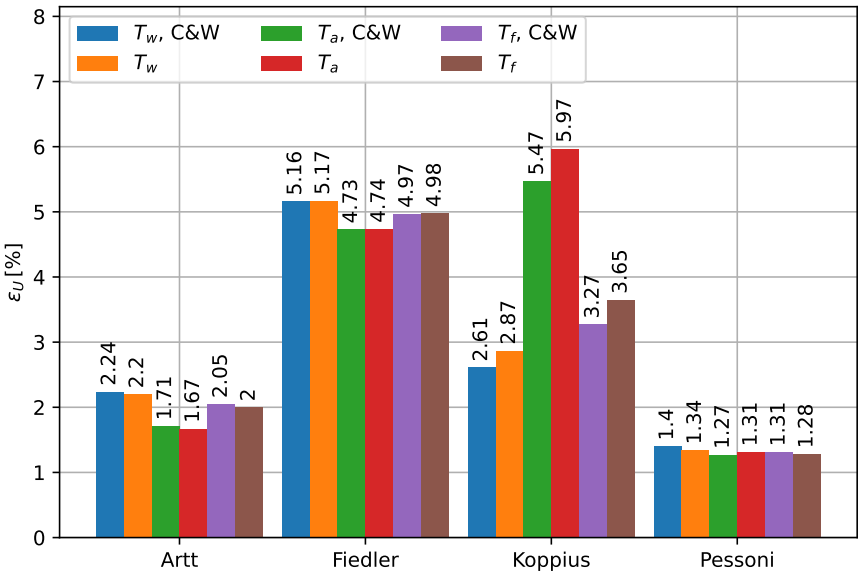

Figure 5.2: RMSPE of velocity depending on correction method, optimized T_w

was not reported. In this plot, there is a significant difference between the methods. From the height of the bars, it is immediately obvious that the T_a methods perform in this case consistently worse than the other two. Furthermore, the $C\&W$ correction reduces the errors in T_f and T_a methods, but surprisingly increases them for the constant fluid properties method T_w. The most important observation is that the RMSPE for the methods evaluating the fluid properties at T_f and incorporating the C&W correction term are consistently the lowest. Looking back at Fig. 5.2 and comparing the RMSPE of the 'T_f, C&W' method with Fig. 5.3, it appears almost unchanged. This leads to the conclusion that the optimal value of T_w for this method is actually close to the value estimated from the overheat of the wire, meaning that temperature calibration might not be necessary if this method is used.

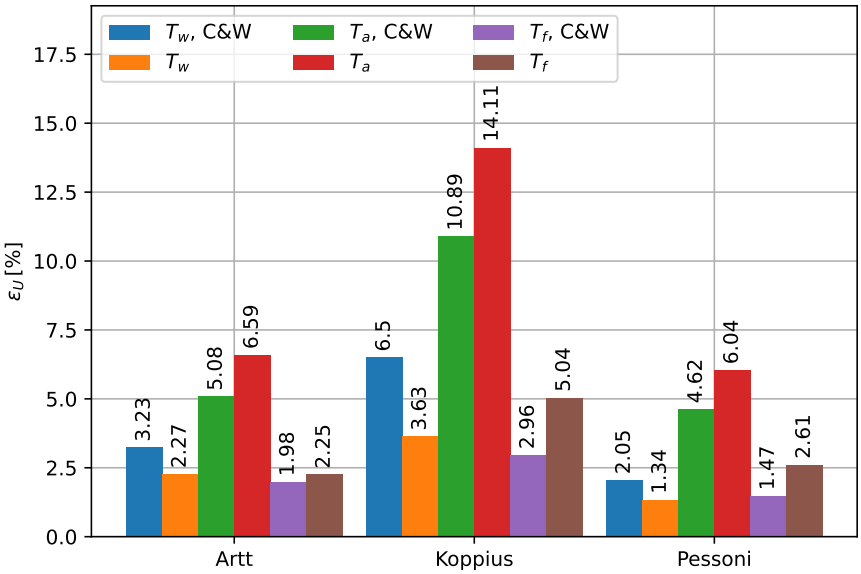

Figure 5.3: RMSPE of velocity depending on correction method, T_w from overheat

Figures 5.4 to 5.6 show how the velocity error grows depending on the departure from optimal T_w for the three datasets which specified the hot-wire temperature in the original paper, indicated in the plots with the black vertical line. Looking at these graphs agrees with the previous conclusion. For every plot, similar trends can be spotted - the estimated hot-wire temperature falls completely outside the optimum for T_a methods, and almost exactly at the optimum for 'T_f, C&W'. Thus, it seems that T_a is indeed not a good physical representation of the hot-wire response. It can only be considered if T_w is treated as an optimization parameter. On the other hand, the C&W correction with fluid properties evaluated at the film temperature is optimal for correcting the hot-wire measurements using the hot-wire temperature estimated from the overheat ratio.

The graphs can also be used to judge the sensitivity of each method to the correct estimation of T_w. For example, T_a methods exhibit a relatively narrow range of T_w where the maximum velocity errors are kept low, seen visually by the width of the "valley" formed by the curves; and show a rapid growth rate of the errors outside the optimum range. Meanwhile, T_w and to a lesser extent T_f methods exhibit a wider range of T_w where the error remains low. In practice, this means that it is safer to use T_f and T_w methods even if T_w is optimized. If an incorrect T_w is found from a biased calibration set, T_a methods increase the likelihood of higher errors. Therefore, T_f or T_w methods are a safer choice even if T_w is optimized.

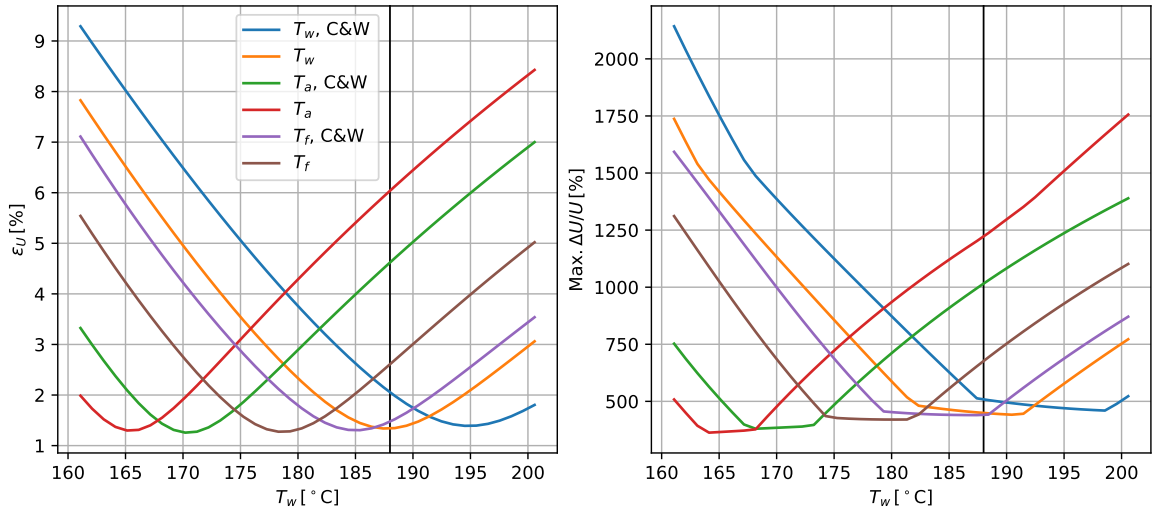

Figure 5.4: Sensitivity of RMSPE of velocity and maximum relative velocity error to T_w depending on correction for Pessoni & Chao data

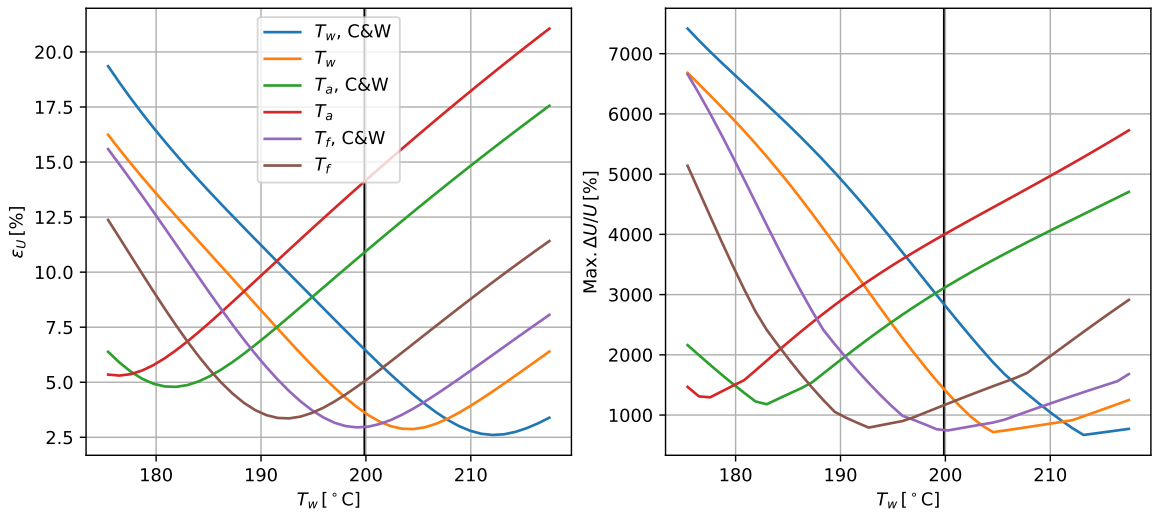

Figure 5.5: Sensitivity of RMSPE of velocity and maximum relative velocity error to T_w depending on correction for Koppius & Trines data

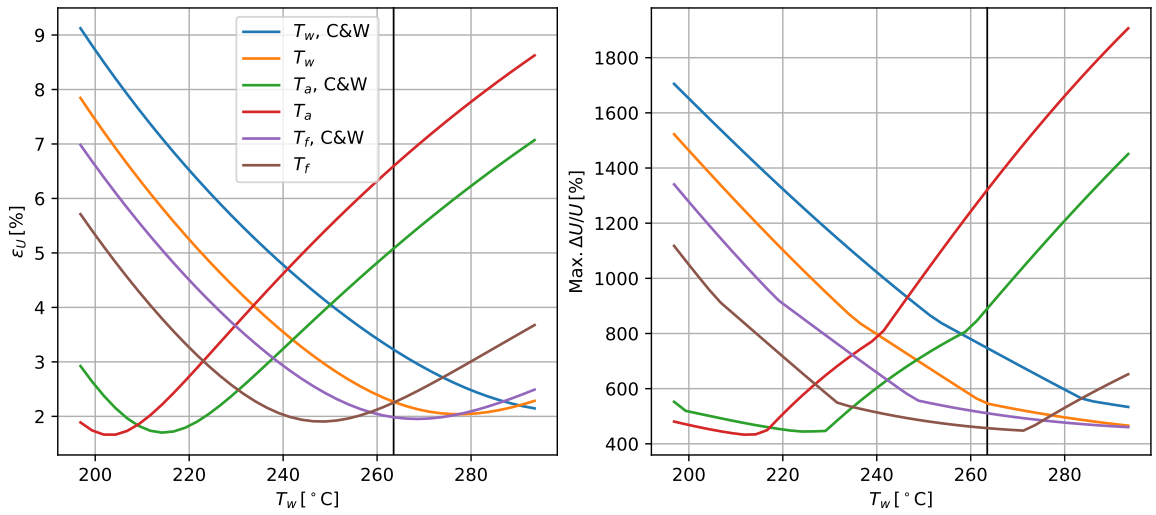

Figure 5.6: Sensitivity of RMSPE of velocity and maximum relative velocity error to T_w depending on correction for Artt & Brown data

5.1.2. Concluding remarks

In conclusion, if a calibration set spanning a wide temperature range is available, T_w optimization can be successfully employed to ensure the minimization of velocity errors. In this case, even the simplest correction assuming invariant fluid properties performs close to the best. The Collis & Brown correction does not change the RMS error noticeably. Since the T_a correction methods offer no meaningful advantage in simplicity (still requiring the evaluation of fluid properties) and provide no accuracy benefit, showing at best marginal improvement over T_f methods and at worst complete inadequacy (as in the Koppius & Trines dataset), and because they are notably more sensitive to accurate estimation of T_w, these methods should be avoided.

If T_w is only estimated from the overheat ratio, calculating the fluid properties at the film temperature and incorporating the Collis & Brown correction term leads to by far the lowest errors.

Therefore, regardless of whether T_w is optimized or not, the calculation of the fluid properties at T_f with the use of the C&W correction offers the best accuracy. The basic correction with constant fluid properties can also lead to reasonable results if the C&W correction is omitted. Calculating the fluid properties at the freestream temperature of the fluid should not be done.

It is also worth noting that none of the correction methods were able to fit the data from Fiedler adequately. A potential explanation for this disagreement is that the $\mathrm{Re}_d = Ud_w/\nu$ values were too low. This was the result of a combined low diameter and velocity than other datasets. Therefore, more complex calibration methods are likely required for HWA at low Re_d numbers.

5.2. X-wire calibration

With the experiment setup described in Section 4.2, a very fine calibration dataset was collected. The final dataset contained 2102 points, spanning the velocity range $5\,\mathrm{m\,s^{-1}}$ to $30\,\mathrm{m\,s^{-1}}$ and yaw angle range $-40\,^\circ$ to $40\,^\circ$, with the exception of $\phi < 36^\circ$ at $U = 22\,\mathrm{m\,s^{-1}}$, which were not recorded due to an error. The complete grid of points can be seen in Fig. 5.7.

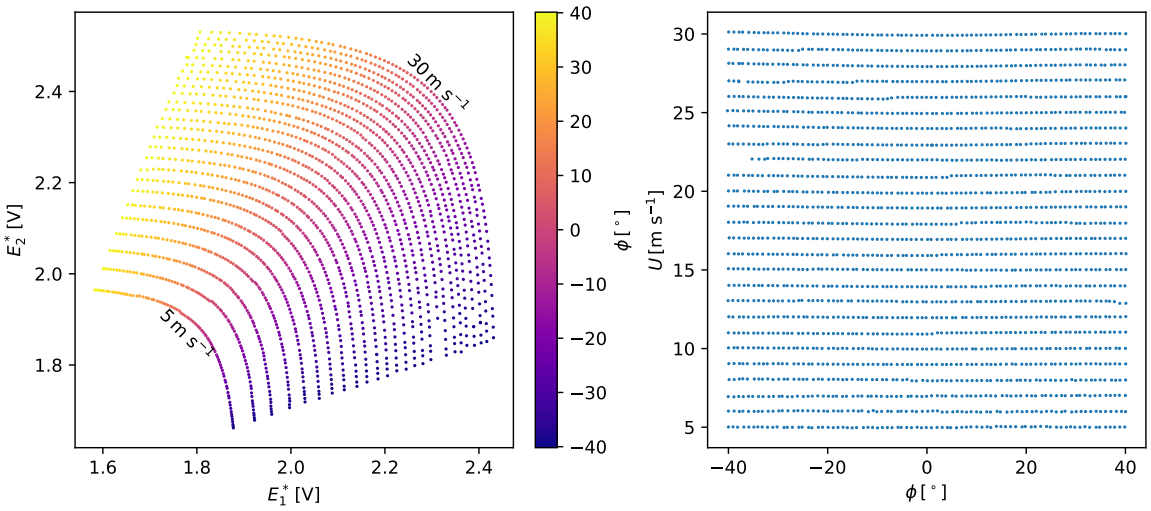

Figure 5.7: Calibration grid in U^*-ϕ and E_1^*-E_2^* space

Nine X-wire calibration schemes from Section 2.3 were compared. The first group were the direct polynomial fits of U^* and ϕ (Dir. U,phi) and u^* and v^* (Dir. u,v), both with polynomials of third and fourth degree. The second group was the look-up methods of Lueptow with third-, fourth-, and fifth-degree polynomials used for intermediate fits, and modified Browne with second- and third-degree fits. Finally, an effective cooling velocity method was included for reference. The errors of U^* and ϕ of each method can be qualitatively seen in Fig. 5.8. An interesting observation is that the errors tend to be higher at high deflection angles and low velocities. This is especially true for the effective velocity and the direct polynomial fit in U^* and ϕ, which can be seen as the departure of the colored symbols indicating ”measured” values from the true values marked with ”x”.

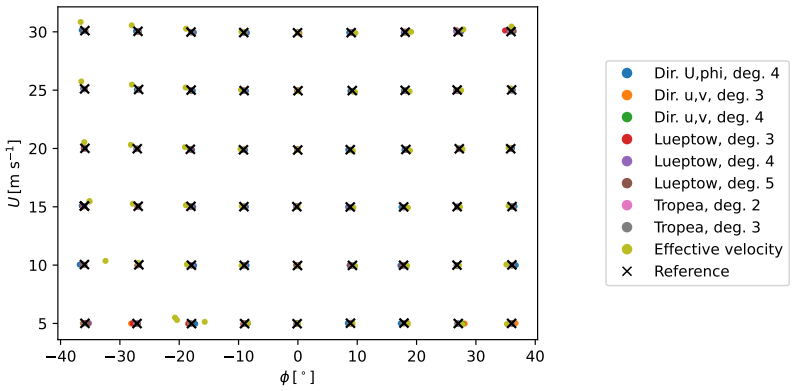

Figure 5.8: Reference and predicted U^* and ϕ

To compare the calibration schemes, the RMSPE of the predicted velocity components u^* and v^* as defined in Eqs. (4.2a) and (4.2b) is shown in Fig. 5.9. From the especially high bars in both velocity components is immediately clear that the effective velocity method is not able to accurately calculate velocities with this wide yaw angle range. Similarly, the direct polynomial fitting methods in U^* and ϕ are not able

to correctly match the data - even if the polynomial of fourth degree is used, the errors in v^* are much higher than for the other models. The fourth-degree polynomial fitting of u^* and v^* seems to fit the X-wire calibration data well, as seen by error levels not much higher than the look-up methods. The modified method of Browne performs consistently best, with RMSPE of around 0.15% regardless of the degree of the polynomial used. The performance of the Lueptow methods is worse, seemingly even fifth-degree polynomials lead to higher errors.

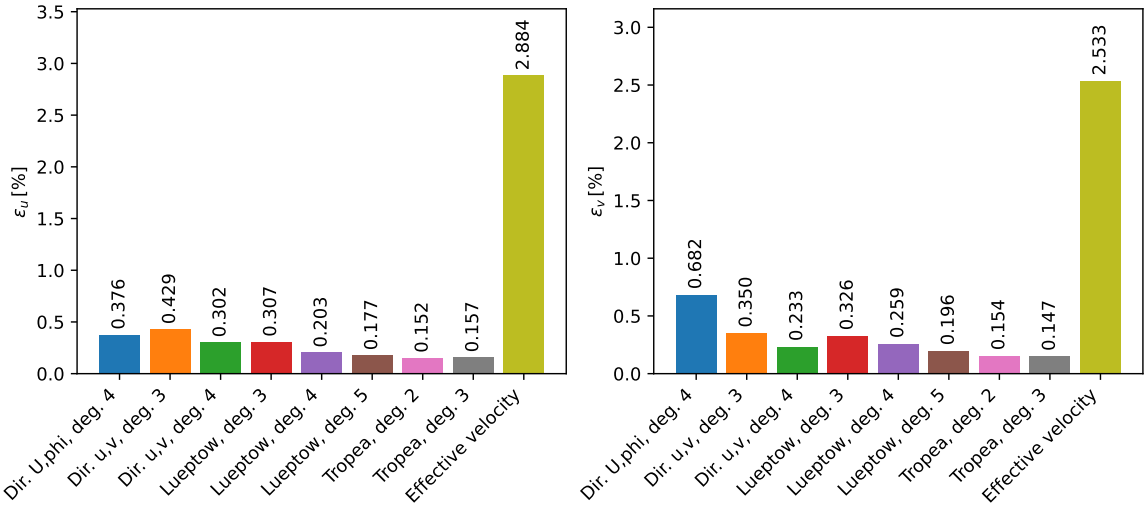

Figure 5.9: RMSPE of u^* (Eq. (4.2a)) and v^* (Eq. (4.2b)) velocity components depending on calibration scheme

For a more detailed analysis, only four of the best performing methods as judged by the global RMSPE were chosen, namely direct fourth-degree polynomial fitting of u^* and v^*, the look-up method by Lueptow in degree 5, and both modified Browne methods.

Figure 5.10 shows the RMSPE in u^* and v^* as a function of yaw angle. In this case, the RMSPE is not computed for the global range of U and ϕ like in Eq. (4.2), but over a range of velocities for the specific angle ϕ_i. Letting i represent an angle step and j a velocity step in calibration,

$$\varepsilon_u^{(i)} = \sqrt{\frac{1}{N_j^{(i)}} \sum_{j=1}^{N_j^{(i)}} \left(\frac{u_c^{*(i,j)} - u_m^{*(i,j)}}{U_m^{*(i,j)}} \right)^2} \tag{5.6a}$$

and

$$\varepsilon_v^{(i)} = \sqrt{\frac{1}{N_j^{(i)}} \sum_{j=1}^{N_j^{(i)}} \left(\frac{v_c^{*(i,j)} - v_m^{*(i,j)}}{U_m^{*(i,j)}} \right)^2}, \tag{5.6b}$$

where $N_j^{(i)}$ is the number of different velocity calibration points at an angle step ϕ_i. Looking at the graph of the error of v^*, the Lueptow method underperforms in predicting v^* at high flow deflection compared to the rest of the look-up methods. The

periodic trends in the plot of the u error of the direct polynomial u-v fit mean that this method might still be underfitting the data.

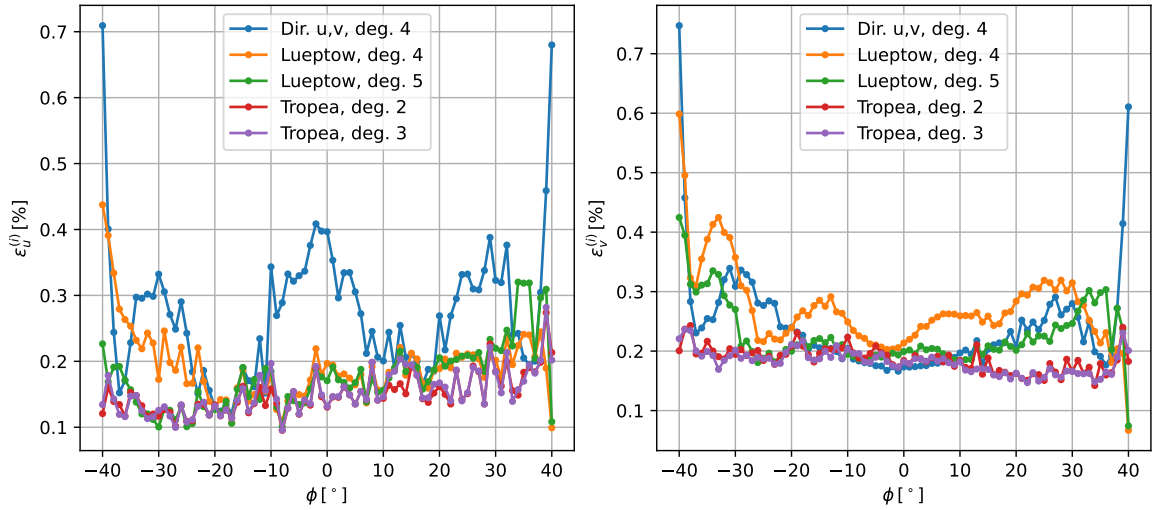

Figure 5.10: $\varepsilon_u^{(i)}$ (Eq. (5.6a)) and $\varepsilon_v^{(i)}$ (Eq. (5.6b)) as a function of ϕ

Figure 5.11 shows the dependence of errors on velocity magnitude. Here, the RMS of the error is calculated over the range of yaw angles for a given velocity step in calibration, according to

$$\varepsilon_u^{(j)} = \sqrt{\frac{1}{N_i^{(j)}} \sum_{i=1}^{N_i^{(j)}} \left(\frac{u_c^{*(i,j)} - u_m^{*(i,j)}}{U_m^{*(i,j)}} \right)^2} \tag{5.7a}$$

and

$$\varepsilon_v^{(j)} = \sqrt{\frac{1}{N_i^{(j)}} \sum_{i=1}^{N_i^{(j)}} \left(\frac{v_c^{*(i,j)} - v_m^{*(i,j)}}{U_m^{*(i,j)}} \right)^2}, \tag{5.7b}$$

where $N_i^{(j)}$ is the number of angle steps at a specific velocity step U_j. As an interesting observation, all methods exhibit highest errors at low velocities. The fit of the direct polynomial method is especially poor compared to the look-up methods, with the RMS percentage error more than twice as high.

Overall, the look-up methods seem to be the best suited for X-wire calibration. The errors of these method were consistently among the lowest out of all methods across the entire range. The modified Browne methods seem to be more stable than Lueptow, potentially thanks to the replacement of polynomials with more stable power laws.

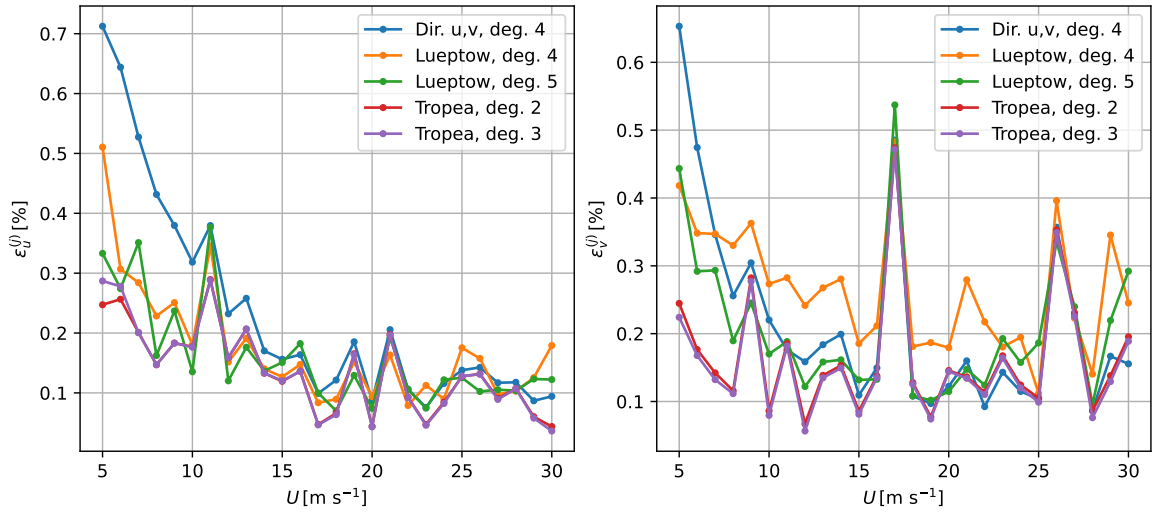

Figure 5.11: $\varepsilon_u^{(j)}$ (Eq. (5.7a)) and $\varepsilon_v^{(j)}$ (Eq. (5.7b)) as a function of U^*

5.2.1. Calibration grid convergence study

First, the change in velocity prediction errors was compared while reducing the number of U steps in calibration and keeping the full span of yaw angles. While reducing the number of U levels, the values of U were chosen at even spacing in $U^{0.25}$ to keep them roughly equally spaced on the E grid (since the voltage varies roughly with $U^{0.25}$, see Kings law). The example reduced dataset for eight U steps chosen in this method is shown in Fig. 5.12a. The values of ϕ were chosen at even spacing in $\cos\phi$ to include more points at high ϕ, which was found to offer good polynomial fitting across the domain through trial-and-error. The example reduced calibration set for 11 ϕ levels can be seen in Fig. 5.12b. These reduced grids were used for fitting of the polynomials, which were subsequently evaluated on the complete calibration grid and the prediction errors computed.

Initially, unexpected trends were observed in the errors at different number of velocity steps. The explanation for this was found to be the fact that a few velocity levels seemed to be outliers, performing poorly for every model - $11\,\mathrm{m\,s^{-1}}$, $17\,\mathrm{m\,s^{-1}}$, $19\,\mathrm{m\,s^{-1}}$, $21\,\mathrm{m\,s^{-1}}$, and $26\,\mathrm{m\,s^{-1}}$, as evident from the spikes in Fig. 5.11. The effect of the inclusion of these erroneous velocity steps on the error seemed to be higher than the effect of fitting on coarser grids, and also negatively affected specific numbers of steps which landed on those erroneous U levels. Therefore, these steps of velocity were omitted from the analysis, which is visible from the gaps in Fig. 5.12a.

Figure 5.13 show the RMSPE of the errors in the u^* and v^* velocity components. For both modified Browne methods and the higher-degree Lueptow method, the prediction errors remained relatively low for down to approximately 8 steps of U before starting to rise more sharply. On the other hand, the errors of the Lueptow method in fourth-degree and the direct polynomial fit method were stable above 4 velocity steps, indicating that they were not limited by the calibration grid.

The convergence of the RMSPE of the u^* and v^* velocity components in terms of the ϕ resolution is shown in Fig. 5.14. The error levels of the modified Browne methods

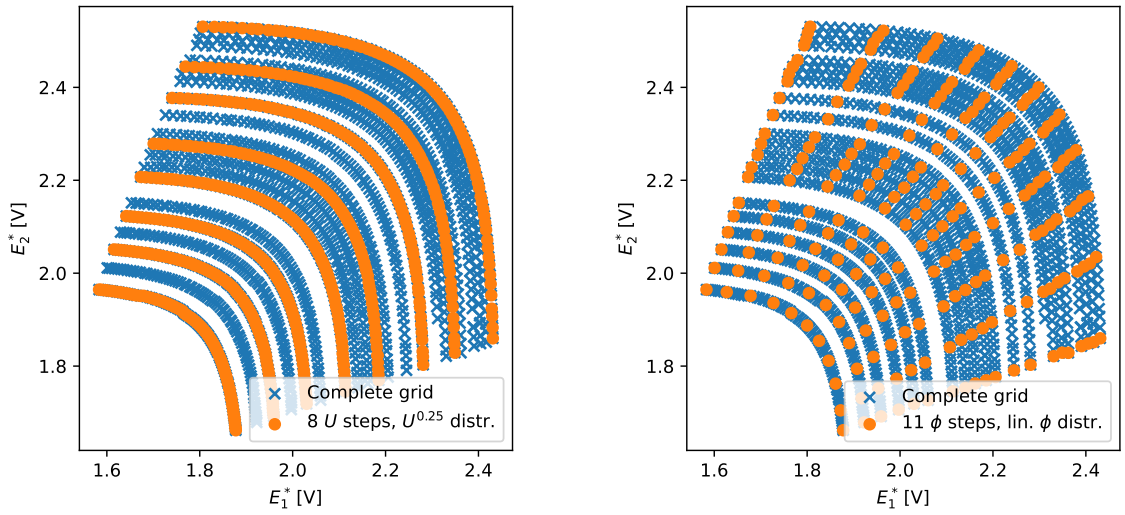

(a) 8 U levels and all ϕ levels

(b) 11 ϕ levels and all U levels

Figure 5.12: Example reduced grids

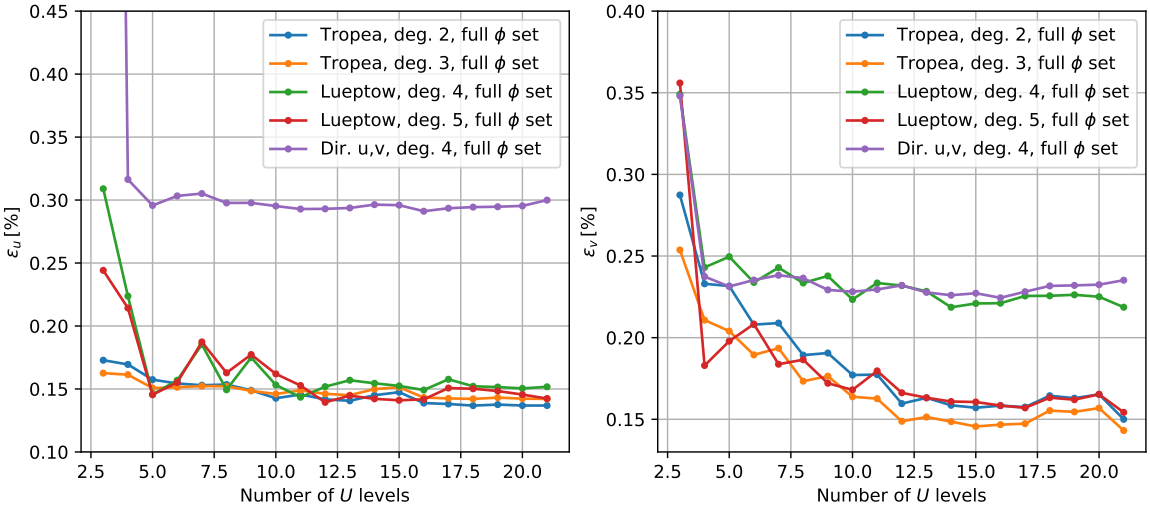

Figure 5.13: RMSPE of u^* (Eq. (4.2a)) and v^* (Eq. (4.2a)) depending on number of U levels

remained stable above around 25 ϕ levels, while rising sharply below that. The direct polynomial fit is the least sensitive to the resolution of the calibration grid in ϕ, as the error rates only started rising sharply below 15 steps of ϕ. The Lueptow methods were very sensitive to the reduction in number of ϕ steps.

To confirm the validity of the independent convergence studies in U and ϕ, the convergence study of the ϕ grid was repeated with the number of velocity steps reduced to 8. The result was the same recommended size of the ϕ grid as with the full U study. The corresponding plots can be found in Chapter C together with plots for additional metrics.

Thus, looking at the convergence in U and in ϕ combined, the modified Browne methods seemed to offer the best accuracy, but the calibration grid needed to be above 8x25 points. If the lower but still reasonable accuracy of the direct polynomial fit

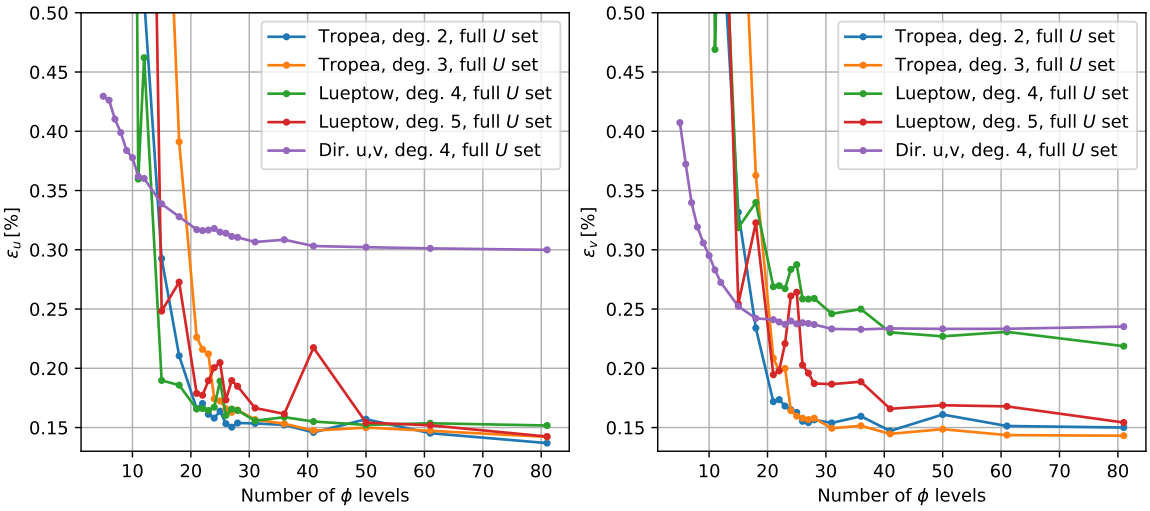

Figure 5.14: RMSPE of u^* (Eq. (4.2a)) and v^* (Eq. (4.2a)) depending on number of ϕ levels

method is acceptable, it can be used for grids as small as 5x15 points.

5.2.2. Concluding remarks

The effective-velocity method produced errors an order of magnitude higher than the rest, therefore it was confirmed unsuitable for the wide angular range considered in this study. The direct polynomial fitting in U and ϕ also showed significantly higher errors than the other approaches even with fourth-degree polynomials.

In contrast, the modified Browne look-up methods exhibited the best accuracy out of all the calibration approaches. Over the full grid, their errors remained low and stable, including in regions of high flow deflection. However, these methods showed a strong dependence on the calibration grid resolution. The convergence studies demonstrated that maintaining good accuracy requires a grid of at least 8 velocity levels and 25 yaw-angle levels, below which the errors increased sharply.

The Lueptow methods also provided reasonably good agreement with the calibration data but were notably more sensitive to reductions in angular resolution than the modified Browne schemes. Their accuracy fell rapidly when the number of ϕ steps was reduced. They were also found to be unreliable at the edges of the calibration grid. It is possible that they could be improved by fitting functions more stable outside the calibration grid, such as the modification of the Browne method by Tropea et al. For example, power laws for the $U^*(E_1^*)|_\phi$ and linear equations for the $E_2^*(E_1^*)|_\phi$ fits. If the stability of this method is sufficiently improved, it would be a better alternative to the modified Browne method due to simpler evaluation of measurements.

While the error levels of the direct polynomial fitting of u^* and v^* on the full dataset were somewhat higher than the look-up methods, the errors remained low on substantially coarser grids. The method preserved acceptable accuracy with as few as 5 velocity steps and 15 yaw-angle steps (three times smaller than the grid required for the look-up methods), making it attractive in situations where the accuracy requirements are less strict and the time saving in calibration is desirable.

Overall, the results show that the choice of calibration method must consider both desired accuracy and practical requirements. The modified Browne look-up methods offer the highest accuracy when a relatively fine grid can be obtained, whereas direct polynomial fitting of the velocity components can be an attractive alternative for slightly looser accuracy requirements.

6

Conclusion

This thesis aimed to enable more robust calibration at the LSL by addressing two issues: the lack of a compact universal calibration system, and uncertainties in best practices for temperature correction methods and X-wire calibration.

For temperature correction, the evaluation across four independent datasets showed that the errors of the simplest schemes, where changes in fluid properties with temperature were neglected, remain surprisingly low over a wide temperature range. Nevertheless, correction based on the evaluation of fluid properties at the film temperature combined with the Collis & Williams correction term consistently produced the lowest errors regardless of the dataset. Corrections based on the evaluation of fluid properties at freestream temperature performed poorly and showed high sensitivity to the used wire temperature T_w, and should not be used. If T_w is estimated from the overheat ratio, the film-temperature correction should be used. Overall, the temperature-correction study showed that reasonable correction is possible without excessive model complexity, provided that the wire temperature is predicted carefully. However, since in most datasets the RMSPE was still above 2% with the best method, more complex calibration relations might be required for a further improvement of accuracy. Finally, the hot-wire calibrator at the LSL was fitted with flow-heating capability, and can be used in the future to test these conclusions and evaluate different calibration schemes.

For X-wire calibration, a new miniature yaw-actuation system was designed, built, and tested by collecting a dense calibration set at the LSL. This dataset made it possible to evaluate the accuracy of common calibration schemes and their sensitivity to calibration-grid resolution. The modified Browne indirect approach showed the lowest errors and the most stable distribution of errors across the calibration domain, though at the cost of requiring a relatively fine calibration grid of 8 velocity steps by 25 angle steps. The Lueptow interpolation method was more sensitive to angular calibration data, with errors growing rapidly at coarser grids. The direct polynomial fit in u and v offered a good middle-ground, offering reasonable accuracy while being more tolerant to sparse grids down to 5 velocity by 15 angle steps, making it attractive when low calibration time is favored over lower errors. Taken together, the results show that accurate multi-wire CTA calibration can be achieved robustly within restricted test sec-

tions. The new calibrator proved sufficiently stable and repeatable for dense mapping of the calibration domain, and the comparative assessment clarifies the trade-offs between accuracy, robustness, and practical setup constraints. The framework developed here provides a foundation for future multi-wire HWA measurements at the LSL under both thermally stable and thermally variable conditions.

In the end, to answer to the research questions from Section 3.3:

1. Temperature correction
    - Can the effects of temperature and fluid velocity be effectively separated, or are more complex combined calibration methods required?
      For moderate temperature changes up to $40\,^{\circ}\mathrm{C}$ and moderate flow velocities - yes, the RMSPE is less than 2%. For higher temperature span or lower wire Reynold's number, more complex calibration is required.
    - Does the change of fluid properties with temperature need to be taken into account, and if so which reference temperature (freestream or film) yields most consistent correction?
      Neglecting the change in fluid properties increases the RMSPE slightly. If calculating the change in fluid properties, always calculate them at the film temperature and never at the freestream temperature.
    - Is the Collis & Williams correction term required?
      The Collis & Williams correction term lowers the RMSPE slightly if the change of fluid properties is calculated. If the change of fluid properties is neglected, it increases the RMSPE.
    - Can the wire temperature be calculated from the overheat ratio, or does it need to be optimized?
      Optimizing T_w will always lead to the lowest possible error. If it is not possible, the calculated wire temperature can be used if the fluid properties are evaluated at T_f and the Collis & Williams term is included.
2. X-wire calibration
    - How do the different look-up and direct calibration methods compare in measurement error across a dense calibration grid?
      The modified Browne look-up method leads to the lowest RMSPE in u^* and v^* velocity components, and performs well throughout the entire calibration domain. The Lueptow look-up method fails to accurately predict the velocity components at high flow deflections and low velocities. From the direct methods, only direct polynomial fitting of u and v offers leads to errors competitive with look-up methods, but higher at severe flow deflections and low velocities.
    - What calibration grid resolution (velocity and angular spacing) is required for accurate calibration?
      Look-up methods require a grid of at least 8 velocities and 25 angles. On the other hand, direct polynomial fitting of u and v can be used on a grid one-third in size – 5 velocities and 15 angles.

The main research question posed in this study was:

How can a two-wire constant-temperature anemometer be calibrated in-situ under variable flow temperature conditions while maintaining high measurement accuracy and reliability?

In combination, the findings show that high-accuracy in-situ calibration is achieved by:

1. Applying a temperature-correction model that incorporates fluid-property variation and optimizes wire temperature.
2. Using an automated yaw-calibration system that provides dense, repeatable calibration datasets in-situ, without requiring probe removal.
3. Employing robust calibration-reconstruction methods: either indirect schemes with sufficiently dense grids or direct polynomial fits for more compact grids.

Together, these elements enable a two-wire CTA probe to be calibrated in-situ for use under varying flow temperatures while maintaining both high accuracy and operational reliability, directly addressing the limitations previously present at the LSL.

6.1. Recommendations

The results of this work suggest several practical steps to further improve the reliability and usability of multi–wire CTA calibration at the LSL.

Calibration methods

- Extend the temperature–correction experiments using the modified TSI calibrator, including a combined study of both direction and temperature variation to confirm the application of the recommended calibration methods to temperature-varying X-wire measurements.
- Investigate more complex combined temperature-velocity calibration schemes.
- Investigate an improvement to the Lueptow calibration algorithm by changing the functions used to interpolate the data.

Calibration framework

- Implement the non–linearity compensation of the magnetic encoder to reduce the angle accuracy to above 0.05° angular accuracy.
- Standardise the full calibration workflow—including temperature correction, grid selection and generation, calibration and experiment and data logging, and data inversion into a single LabView routine to reduce operator burden and improve repeatability.
- Integrate the controller, magnetic encoder, and existing accelerometer on a single compact circuit board mounted on the calibrator, reducing the amount of cables.
- Find more accurate and quicker methods for alignment of the hot-wire calibrator with the wind-tunnel, for example based on the accelerometer.

References

[1] P. W. Bearman. *Corrections for the Effect of Ambient Temperature Drift on Hot-Wire Measurements in Incompressible Flow*. DISA Inf. 11. 1971.

[2] D. C. Collis and M. J. Williams. “Two-Dimensional Convection from Heated Wires at Low Reynolds Numbers”. In: *Journal of Fluid Mechanics* 6.3 (1959), pp. 357–384. ISSN: 0022-1120. DOI: 10.1017/S0022112059000696.

[3] R. M. Lueptow, K. S. Breuer and J. H. Haritonidis. “Computer-Aided Calibration of X-probes Using a Look-up Table”. In: *Experiments in Fluids* 6.2 (1988), pp. 115–118. ISSN: 0723-4864, 1432-1114. DOI: 10.1007/BF00196462.

[4] C. Tropea, A. L. Yarin and J. F. Foss, eds. *Springer Handbook of Experimental Fluid Mechanics*. Berlin, Heidelberg: Springer Berlin Heidelberg, 2007. ISBN: 978-3-540-25141-5 978-3-540-30299-5. DOI: 10.1007/978-3-540-30299-5.

[5] H. H. Bruun. *Hot-Wire Anemometry : Principles and Signal Analysis*. Oxford Science Publications. Oxford: Oxford University Press, 1995. ISBN: 0-19-856342-6 978-0-19-856342-6.

[6] S. M. Mangalam, G. R. Sarma, S. Kuppa and L. R. Kubendran. “A New Approach to High - Speed Flow Measurements Using Constant Voltage Anemometry”. In: AIAA 17th Aerospace Ground Testing Conference. Nashville, TN: American Institute of Aeronautics and Astronautics, 1st July 1992. DOI: 10.2514/6.1992-3957.

[7] R. Örlü and R. Vinuesa. “Thermal Anemometry”. In: *Experimental Aerodynamics*. CRC Press Taylor & Francis Group, 1st May 2017, pp. 393–428. ISBN: 978-1-315-37173-3. DOI: 10.1201/9781315371733-9.

[8] L. M. Fingerson and P. Freymuth. “Thermal Anemometers”. In: *Fluid Mechanics Measurements*. Washington, D.C.: Hemisphere Pub. Corp., 1983, pp. 99–154. ISBN: 978-0-89116-244-5.

[9] L. V. King. “XII. On the Convection of Heat from Small Cylinders in a Stream of Fluid: Determination of the Convection Constants of Small Platinum Wires with Applications to Hot-Wire Anemometry”. In: *Philosophical Transactions of the Royal Society of London. Series A, Containing Papers of a Mathematical or Physical Character* 214.509–522 (Jan. 1914), pp. 373–432. ISSN: 0264-3952, 2053-9258. DOI: 10.1098/rsta.1914.0023.

[10] R. Chevray and N. K. Tutu. “Simultaneous Measurements of Temperature and Velocity in Heated Flows”. In: *Review of Scientific Instruments* 43.10 (1st Oct. 1972), pp. 1417–1421. ISSN: 0034-6748, 1089-7623. DOI: 10.1063/1.1685457.

[11] A. Abdel-Rahman, C. Tropea, P. Slawson and A. Strong. “On Temperature Compensation in Hot-Wire Anemometry”. In: *Journal of Physics E: Scientific Instruments* 20.3 (Mar. 1987), pp. 315–319. ISSN: 0022-3735. DOI: 10.1088/0022-3735/20/3/017.

[12] M. Barahona, T. A. F. van de Weijer, A. F. Rius-Vidales and M. Kotsonis. “Stability of Swept Wing Boundary Layers under Non-Adiabatic Wall Conditions”. In: AIAA SCITECH 2024 Forum. Orlando, FL: American Institute of Aeronautics and Astronautics, 4th Jan. 2024. DOI: 10.2514/6.2024-0695.

[13] D. H. Pessoni and B. T. Chao. “A Simple Technique for Turbulence Measurements in Nonisothermal Air Flows”. In: *Proceeding of International Heat Transfer Conference 5*. International Heat Transfer Conference 5. Tokyo, Japan: Begellhouse, 1974, pp. 278–282. DOI: 10.1615/IHTC5.2740.

[14] S. Ball, S. Ashforth-Frost, K. Jambunathan and C. Whitney. “Appraisal of a Hot-Wire Temperature Compensation Technique for Velocity Measurements in Non-Isothermal Flows”. In: *International Journal of Heat and Mass Transfer* 42.16 (Aug. 1999), pp. 3097–3102. ISSN: 00179310. DOI: 10.1016/S0017-9310(98)00371-8.

[15] H. Lundström, M. Sandberg and B. Mosfegh. “Temperature Dependence of Convective Heat Transfer from Fine Wires in Air: A Comprehensive Experimental Investigation with Application to Temperature Compensation in Hot-Wire Anemometry”. In: *Experimental Thermal and Fluid Science* 32.2 (1st Nov. 2007), pp. 649–657. ISSN: 0894-1777. DOI: 10.1016/j.expthermflusci.2007.08.002.

[16] M. Hultmark and A. J. Smits. “Temperature Corrections for Constant Temperature and Constant Current Hot-Wire Anemometers”. In: *Measurement Science and Technology* 21.10 (Aug. 2010), p. 105404. ISSN: 0957-0233. DOI: 10.1088/0957-0233/21/10/105404.

[17] A. van Dijk and F. T. M. Nieuwstadt. “The Calibration of (Multi-) Hot-Wire Probes. 1. Temperature Calibration”. In: *Experiments in Fluids* 36.4 (Apr. 2004), pp. 540–549. ISSN: 0723-4864, 1432-1114. DOI: 10.1007/s00348-003-0677-y.

[18] A. van Dijk. “Aliasing in One-Point Turbulence Measurements : Theory, DNS and Hotwire Experiments”. PhD thesis. Delft: Delft University of Technology, 1999. 278 pp.

[19] H. Takahashi, M. Kurita, H. Iijima and S. Koga. “Simplified Calibration Method for Constant-Temperature Hot-Wire Anemometry”. In: *Applied Sciences* 10.24 (24 Jan. 2020), p. 9058. ISSN: 2076-3417. DOI: 10.3390/app10249058.

[20] J. M. Jiménez, M. Hultmark and A. J. Smits. “The Intermediate Wake of a Body of Revolution at High Reynolds Numbers”. In: *Journal of Fluid Mechanics* 659 (25th Sept. 2010), pp. 516–539. ISSN: 0022-1120, 1469-7645. DOI: 10.1017/S0022112010002715.

[21] C. P. Finke. “Temperature-Compensated Calibration and Measurements with Cross-Style Hotwire Anemometers”. MSc thesis. College Station, TX: Texas A&M University, Dec. 2021. HDL: 1969.1/196256.

[22] P. Bradshaw. *An Introduction to Turbulence and Its Measurement*. Oxford: Pergamon Press, 1971. ISBN: 978-0-08-016620-9.

[23] J. O. Hinze. *Turbulence*. New York St. Louis Paris [etc.]: McGraw-Hill, 1959.

[24] F. Wubben. *Single and Cross Hot Wire Anemometry in Incompressible Flow*. Delft: Delft University of Technology, 1991.

[25] W. W. Willmarth and T. J. Bogar. “Survey and New Measurements of Turbulent Structure near the Wall”. In: *The Physics of Fluids* 20.10 (1st Oct. 1977), S9–S21. ISSN: 0031-9171. DOI: 10.1063/1.861765.

[26] L. W. B. Browne, R. A. Antonia and L. P. Chua. “Calibration of X-probes for Turbulent Flow Measurements”. In: *Experiments in Fluids* 7.3 (1st Dec. 1988), pp. 201–208. ISSN: 1432-1114. DOI: 10.1007/BF02332985.

[27] D. Oster and I. Wygnanski. “The Forced Mixing Layer between Parallel Streams”. In: *Journal of Fluid Mechanics* 123 (1982), pp. 91–130. ISSN: 0022-1120. DOI: 10.1017/S0022112082002973.

[28] S.-I. Chang and R. F. Blackwelder. “Modification of Large Eddies in Turbulent Boundary Layers”. In: *Journal of Fluid Mechanics* 213 (Apr. 1990), pp. 419–442. ISSN: 0022-1120, 1469-7645. DOI: 10.1017/S0022112090002385.

[29] B. T. Nguyen. “Calibration of an X-wire with Assessment of a Moderately High Reynolds Number Flow”. MSc thesis. Irvine, CA: University of California, Irvine, 2015.

[30] A. Koppius and G. Trines. “The Dependence of Hot-Wire Calibration on Gas Temperature at Low Reynolds Numbers”. In: *International Journal of Heat and Mass Transfer* 19.9 (Sept. 1976), pp. 967–974. ISSN: 00179310. DOI: 10.1016/0017-9310(76)90177-0.

[31] H. Fiedler. “On Data Acquisition in Heated Turbulent Flows”. In: *Proceedings of the Dynamic Flow Conference 1978 on Dynamic Measurements in Unsteady Flows*. Dynamic Flow Conference. Ed. by B. W. Hansen. Dordrecht: Springer Netherlands, 1978, pp. 81–100. ISBN: 978-94-009-9567-3 978-94-009-9565-9. DOI: 10.1007/978-94-009-9565-9_5.

[32] D. W. Artt and A. Brown. “The Simultaneous Measurement of Velocity and Temperature”. In: *Journal of Physics E: Scientific Instruments* 4.1 (Jan. 1971), pp. 72–74. ISSN: 0022-3735. DOI: 10.1088/0022-3735/4/1/020.

[33] W. Kannuluik and E. Carman. “The Temperature Dependence of the Thermal Conductivity of Air”. In: *Australian Journal of Chemistry* 4.3 (1st Sept. 1951), pp. 305–314. ISSN: 0004-9425, 1445-0038. DOI: 10.1071/CH9510305.

A

Calibrator Documentation

The technical drawings for the custom parts required for the calibrator can be found in this section.

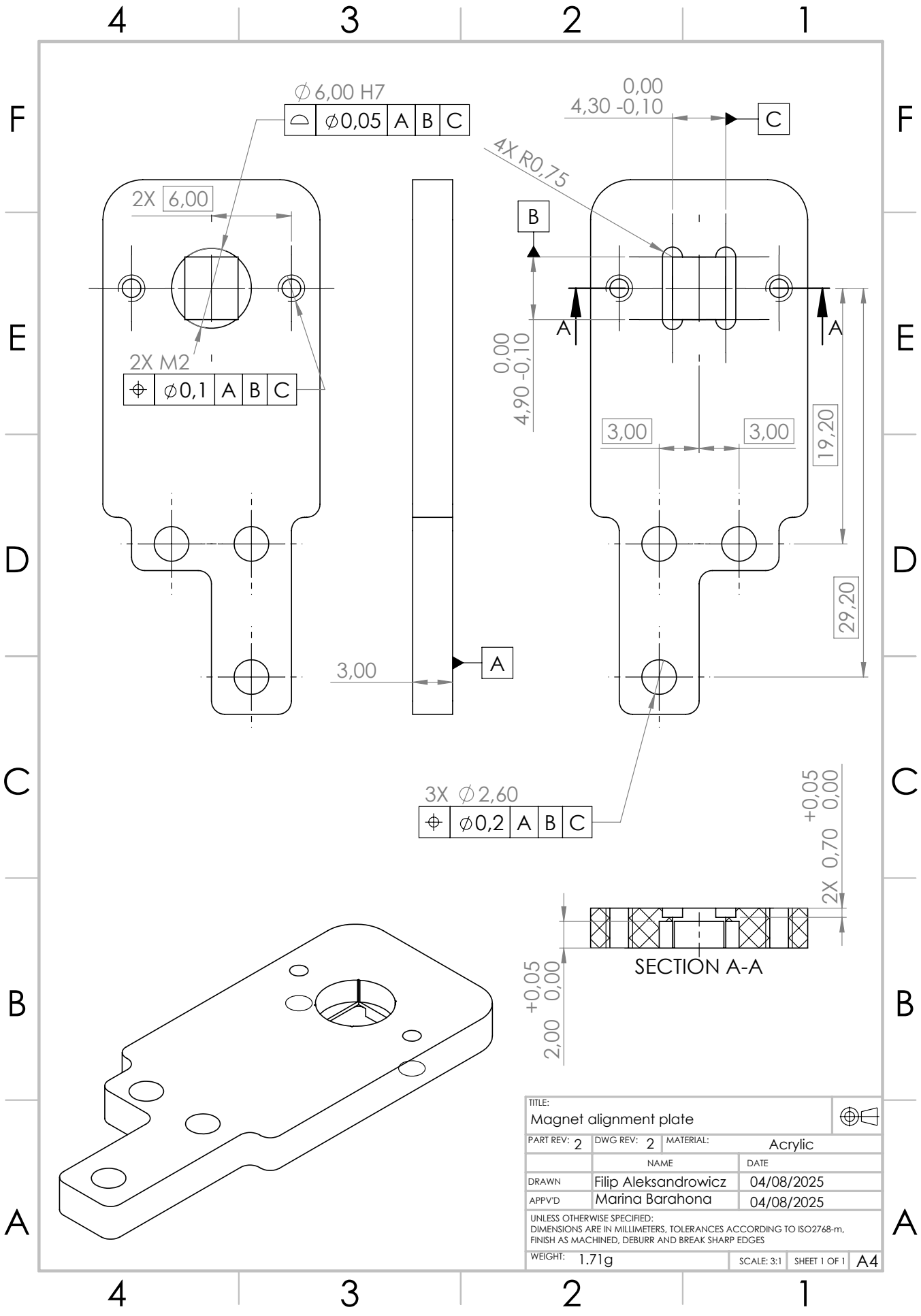

Figure A.1: Magnet alignment plate

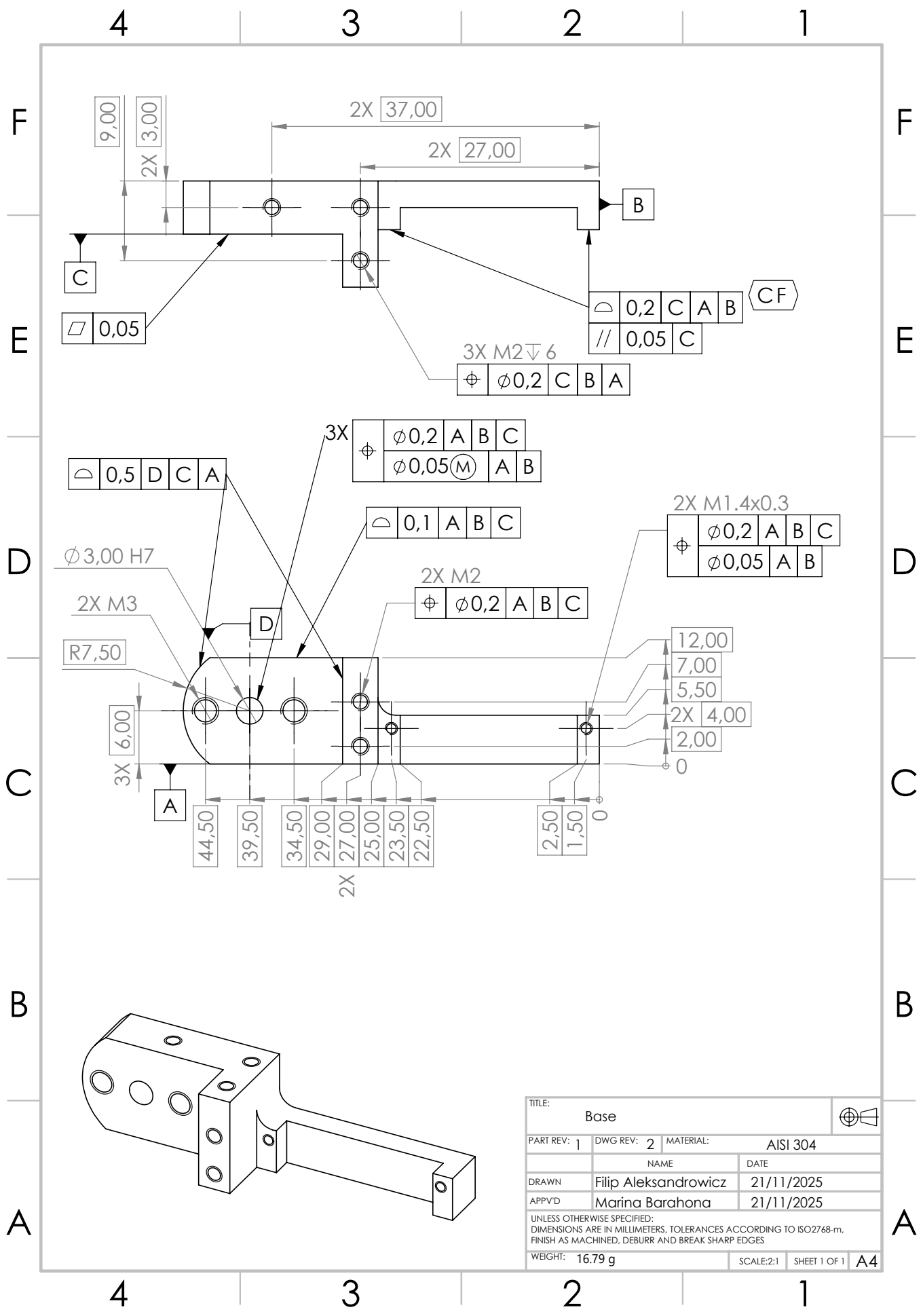

Figure A.2: Base

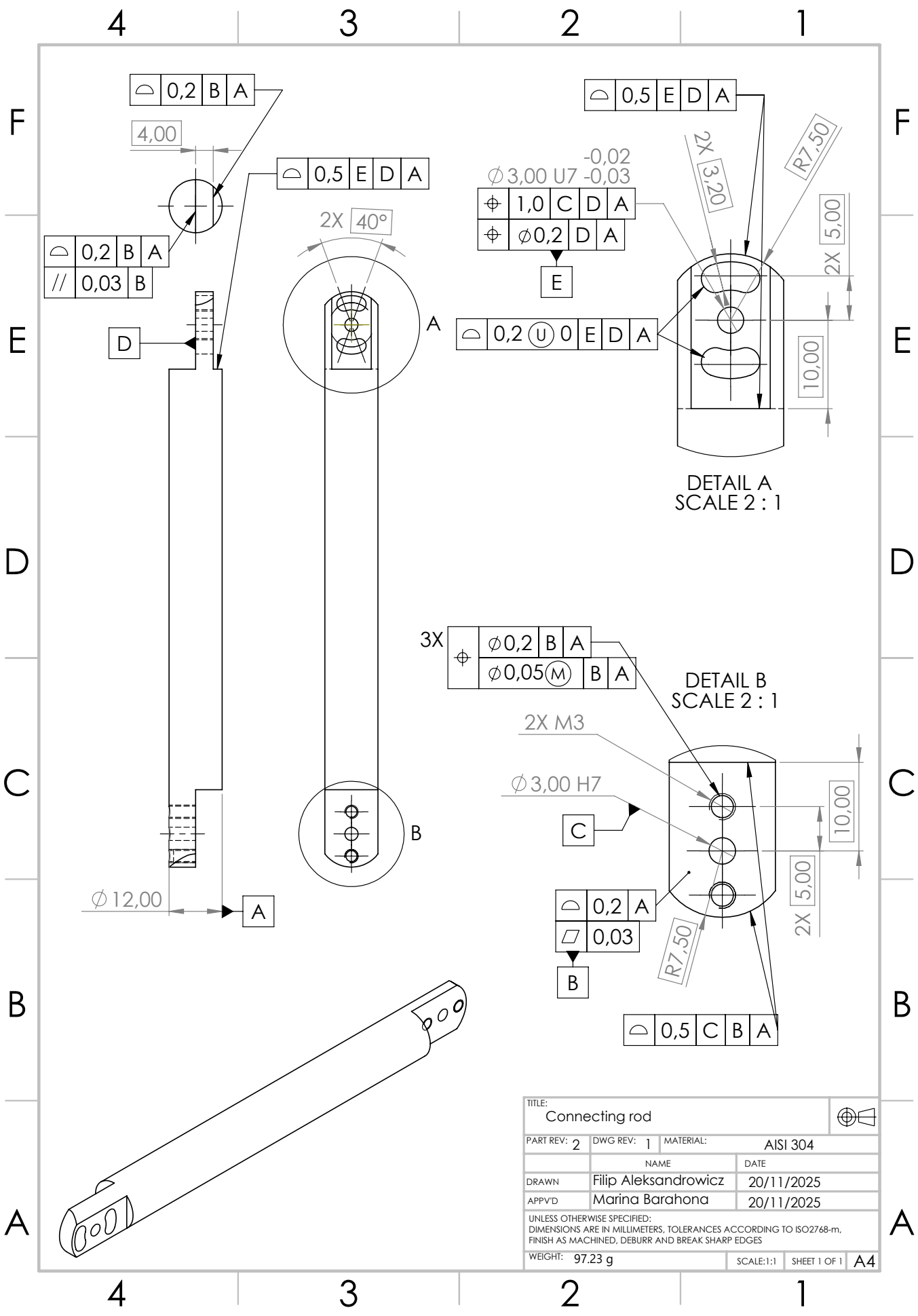

Figure A.3: Connecting rod

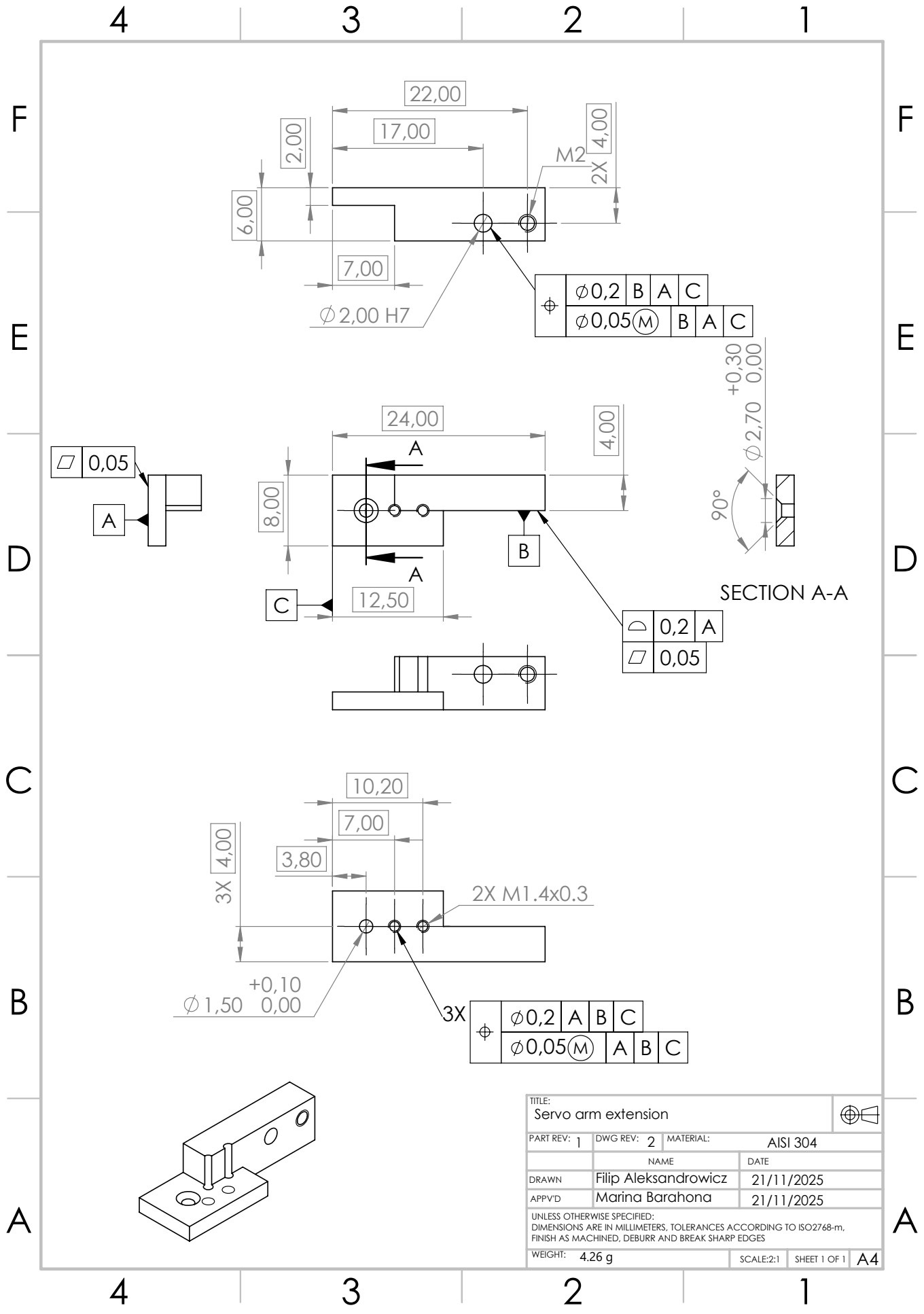

Figure A.4: Servo arm extension

B

Temperature Correction Data

B.1. Pessoni & Chao data

Based on measurements from [13], with a reported $T_w = 461.1\,\mathrm{K}$.

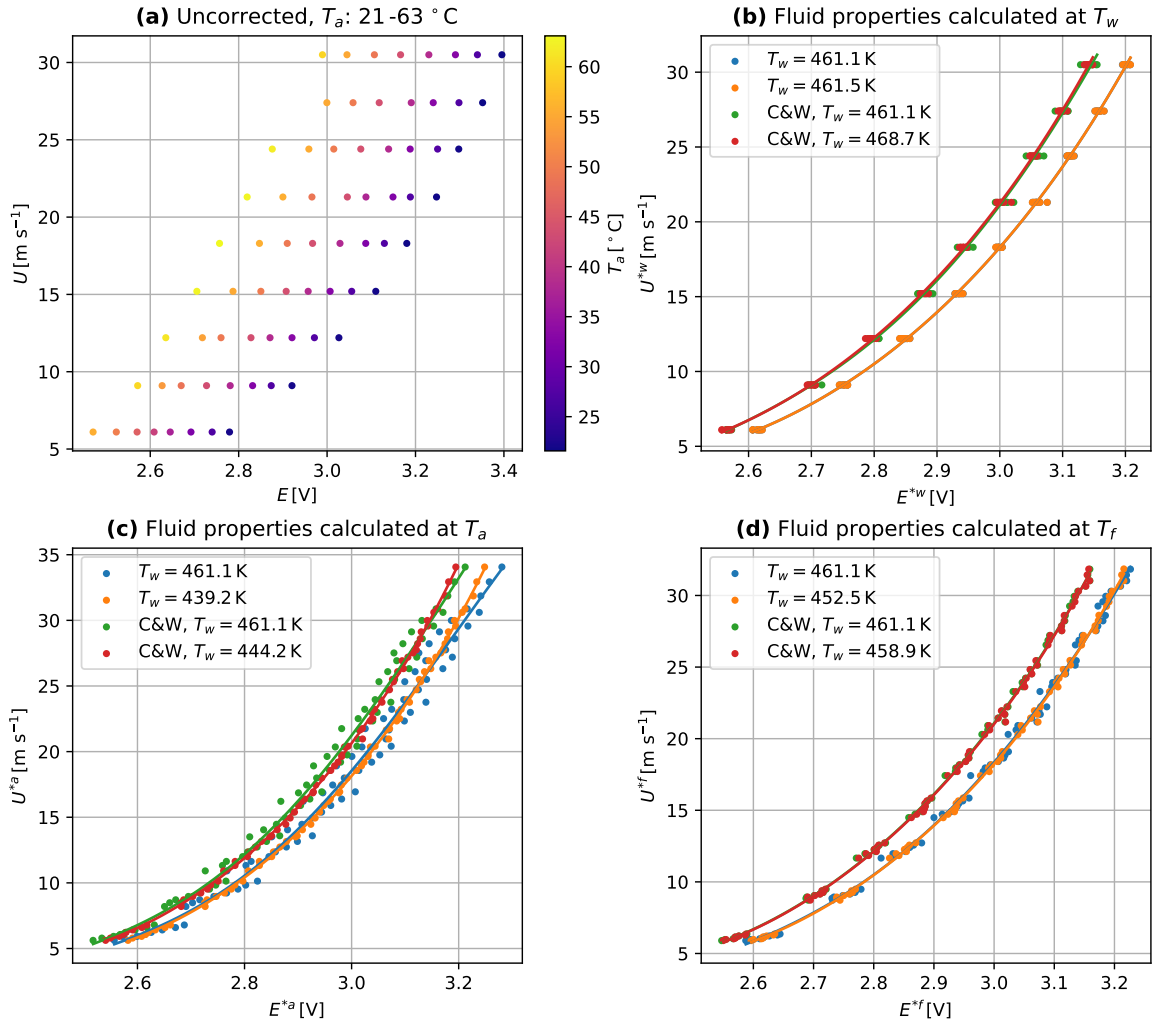

Figure B.1: Temperature correction comparison for Pessoni & Chao data

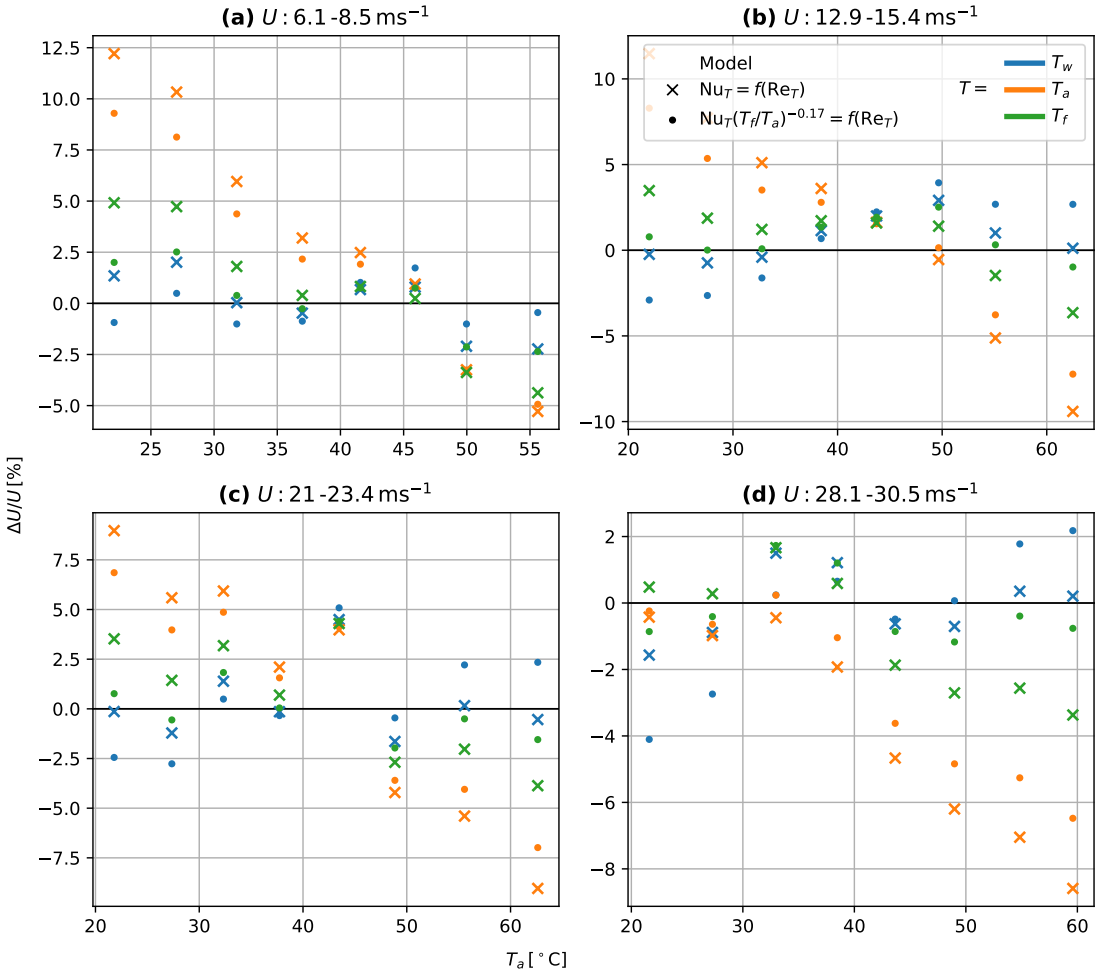

Figure B.2: Velocity error of calibration depending on correction for Pessoni&Chao data, $T_w = 473\,\mathrm{K}$

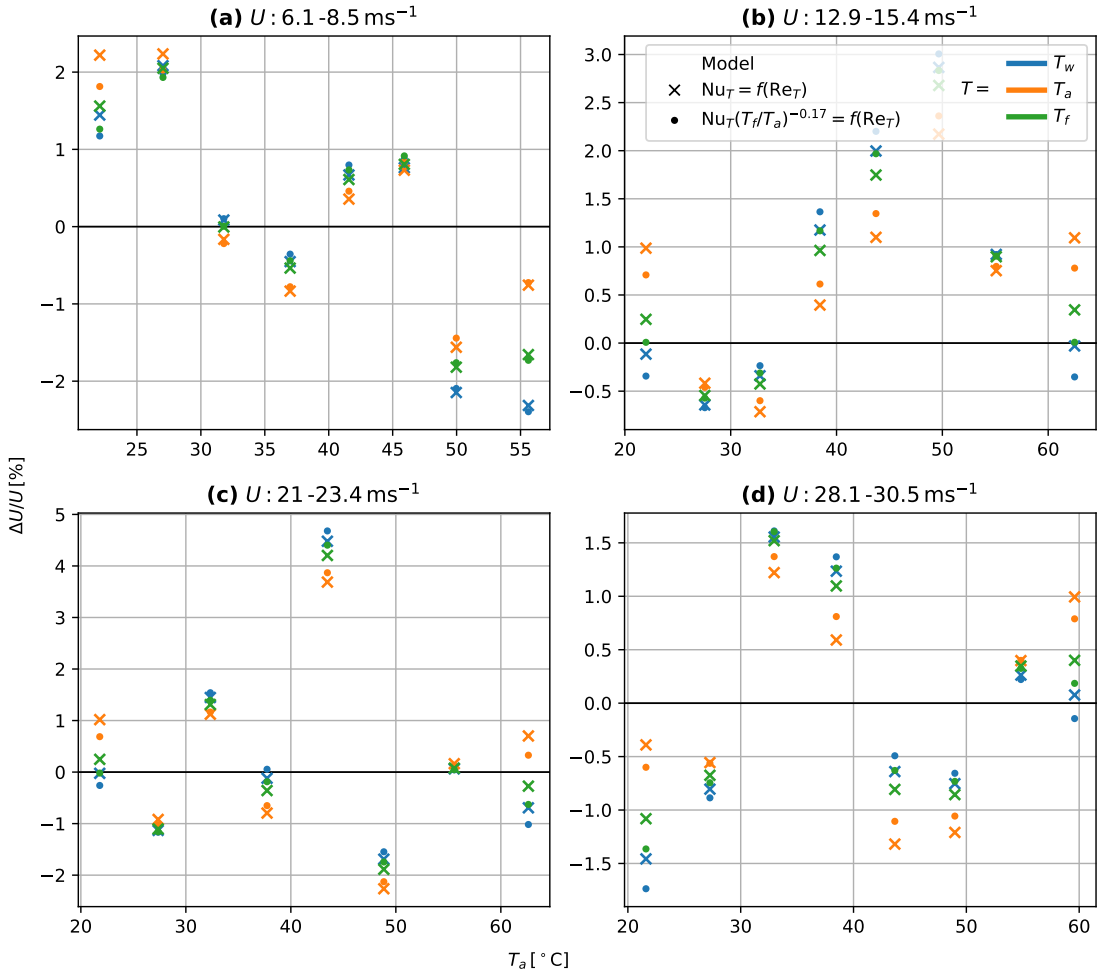

Figure B.3: Velocity error of calibration depending on correction for Pessoni&Chao data, T_w optimized

Correction	T_w [K]	σ_U [m s^{-1}]	Max.ΔU [m s^{-1}]	ϵ_U [%]	Max.$\Delta U/U$ [%]
T_w	**461.1**	0.242	0.957	1.34	4.49
T_w	461.5	0.242	0.954	1.34	4.48
T_w, C&W	**461.1**	0.413	1.252	2.05	5.08
T_w, C&W	468.7	0.255	0.997	1.4	4.68
T_a	**461.1**	1.056	2.62	6.04	12.21
T_a	439.2	0.231	0.785	1.31	3.69
T_a, C&W	**461.1**	0.81	1.976	4.62	10.16
T_a, C&W	444.2	0.226	0.824	1.27	3.87
T_f	**461.1**	0.462	1.028	2.61	6.77
T_f	452.5	0.23	0.895	1.28	4.2
T_f, C&W	**461.1**	0.26	0.937	1.47	4.4
T_f, C&W	458.9	0.24	0.938	1.31	4.4

Table B.1: Velocity errors depending on the temperature correction of the Pessoni&Chao data

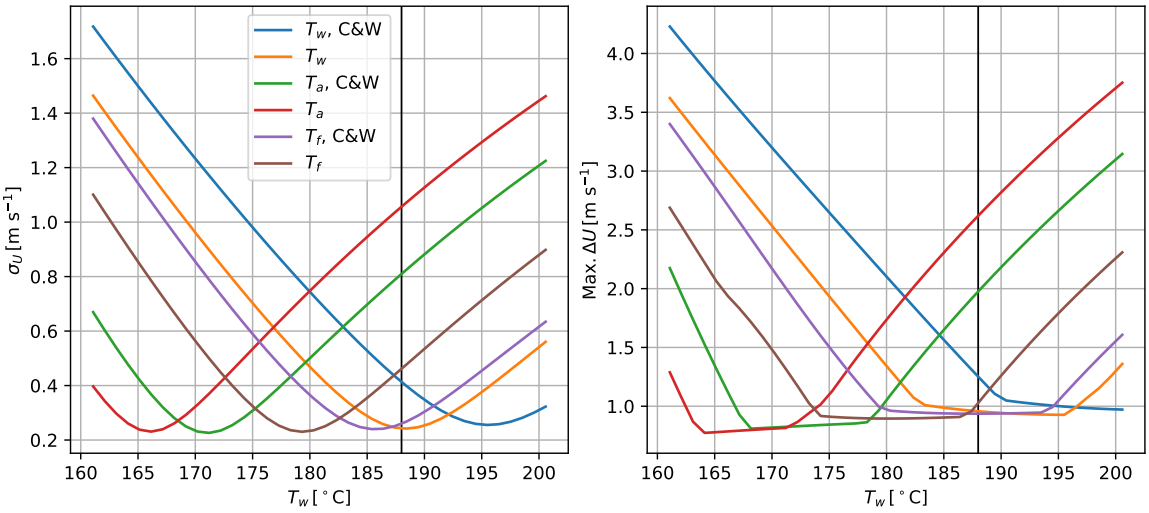

Figure B.4: Sensitivity of velocity error to T_w depending on correction for Pessoni& Chao data

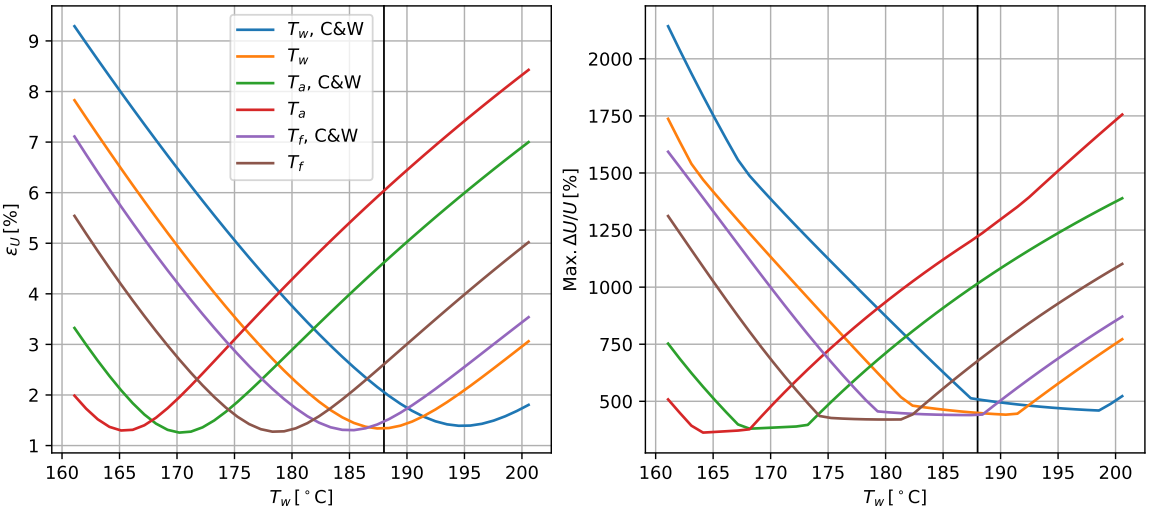

Figure B.5: Sensitivity of relative velocity error to T_w depending on correction for Pessoni& Chao data

B.2. Fiedler data

Based on measurements from [31]. Original overheat ratio was not reported, only optimized T_w in results.

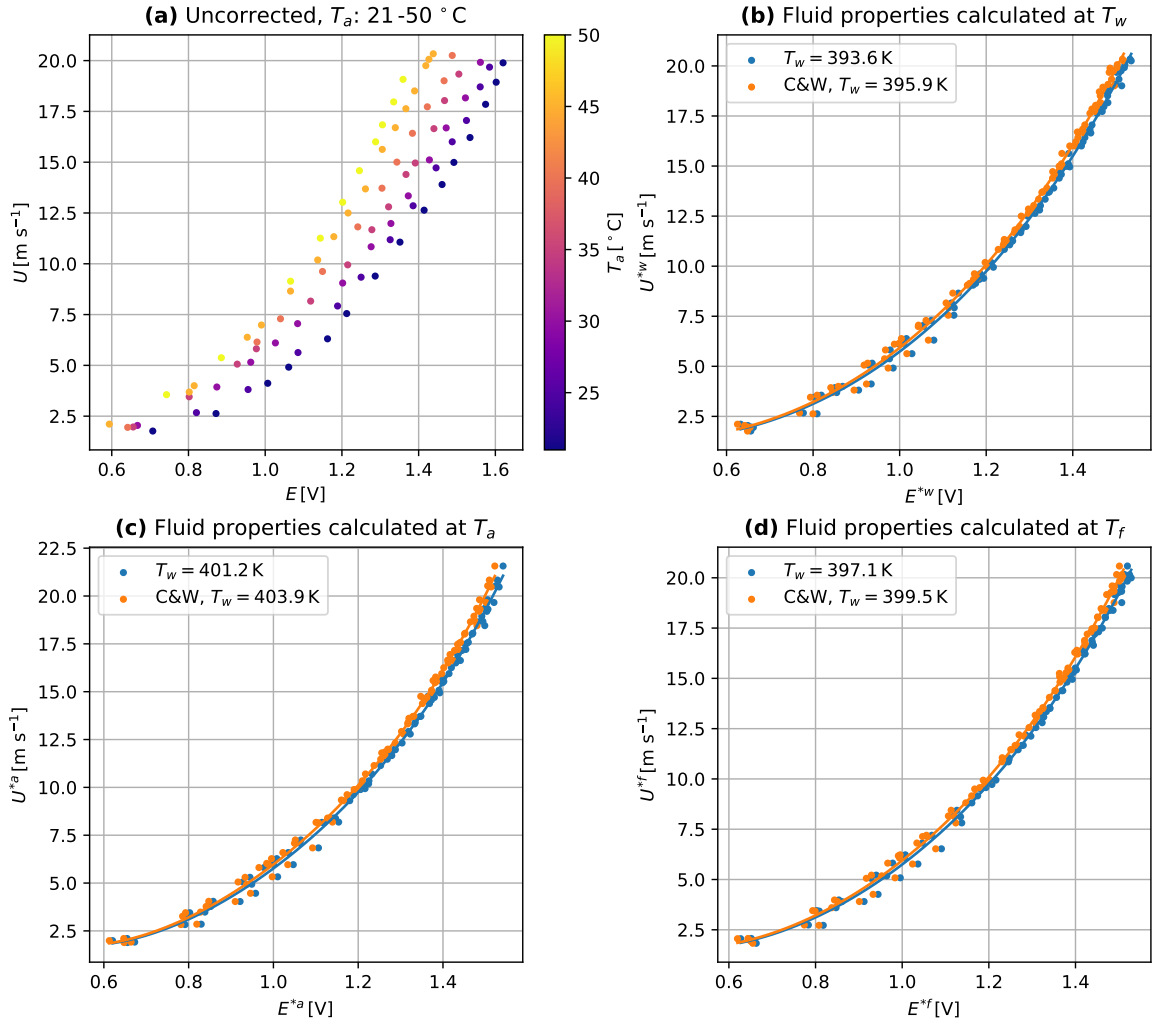

Figure B.6: Temperature correction comparison for Fiedler data

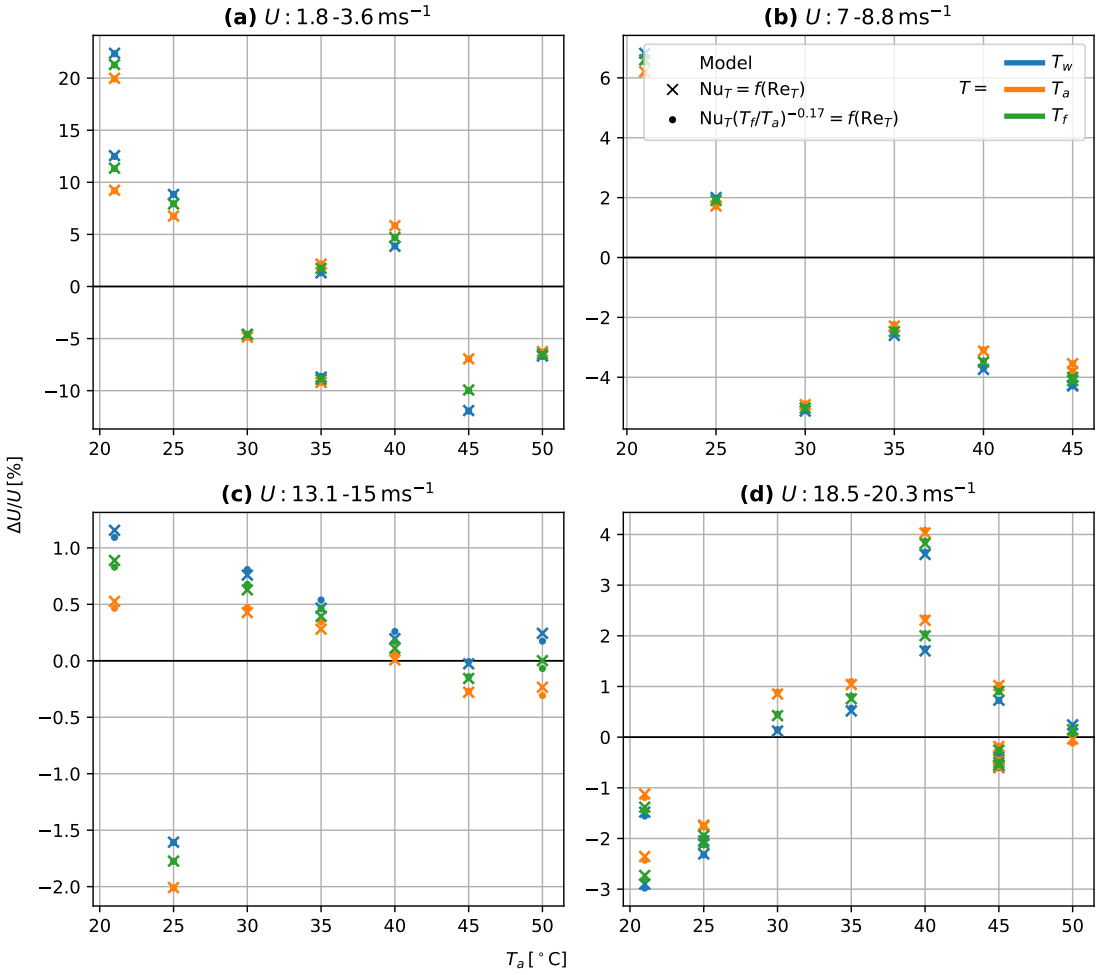

Figure B.7: Velocity error of calibration depending on correction for Fiedler data

Correction	T_w [K]	σ_U [m s^{-1}]	Max.ΔU [m s^{-1}]	ϵ_U [%]	Max.$\Delta U/U$ [%]
T_w	393.6	0.278	0.827	5.17	22.38
T_w, C&W	395.9	0.279	0.821	5.16	22.34
T_a	401.2	0.268	0.793	4.74	19.99
T_a, C&W	403.9	0.269	0.788	4.73	19.92
T_f	397.1	0.274	0.814	4.98	21.31
T_f, C&W	399.5	0.275	0.809	4.97	21.26

Table B.2: Velocity errors depending on the temperature correction of the Fiedler data

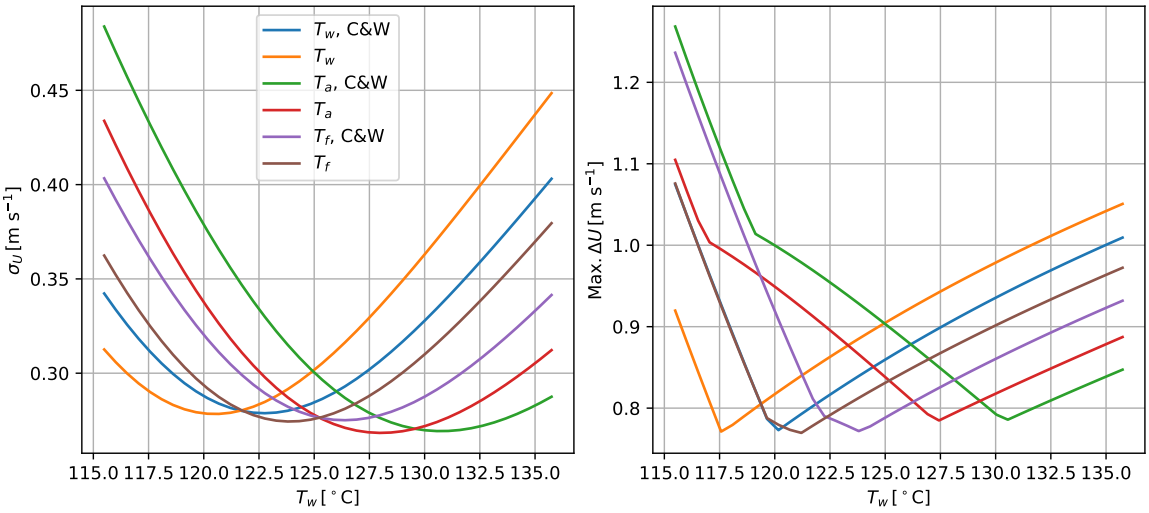

Figure B.8: Sensitivity of velocity error to T_w depending on correction for Fiedler data

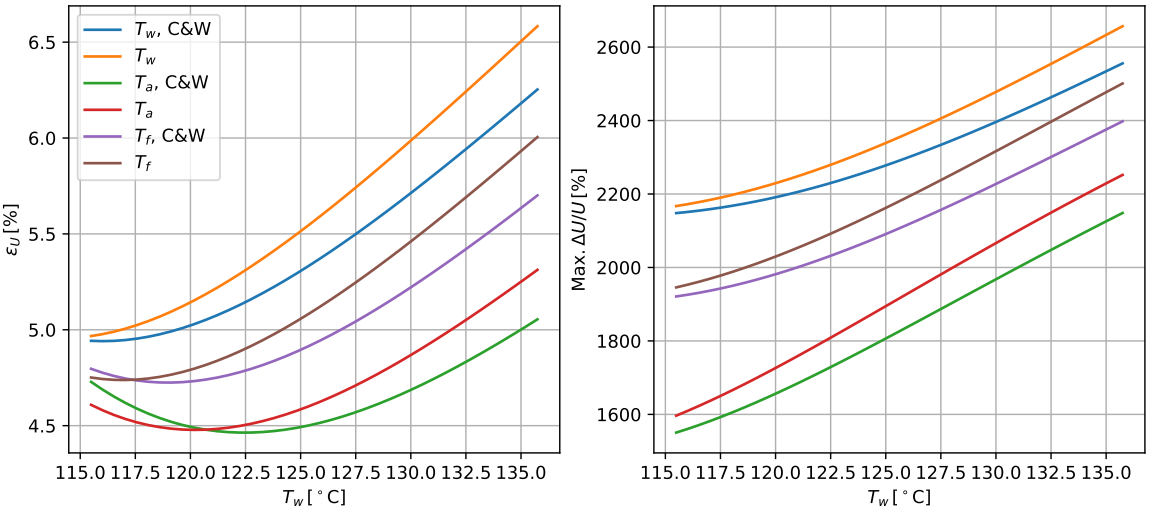

Figure B.9: Sensitivity of relative velocity error to T_w depending on correction for Fiedler data

B.3. Koppius & Trines data

Based on measurements from [30], with reported $T_w = 473\,\mathrm{K}$. Also included in the plots, in bold in Table B.3, and as vertical lines in Fig. B.13 and 5.5.

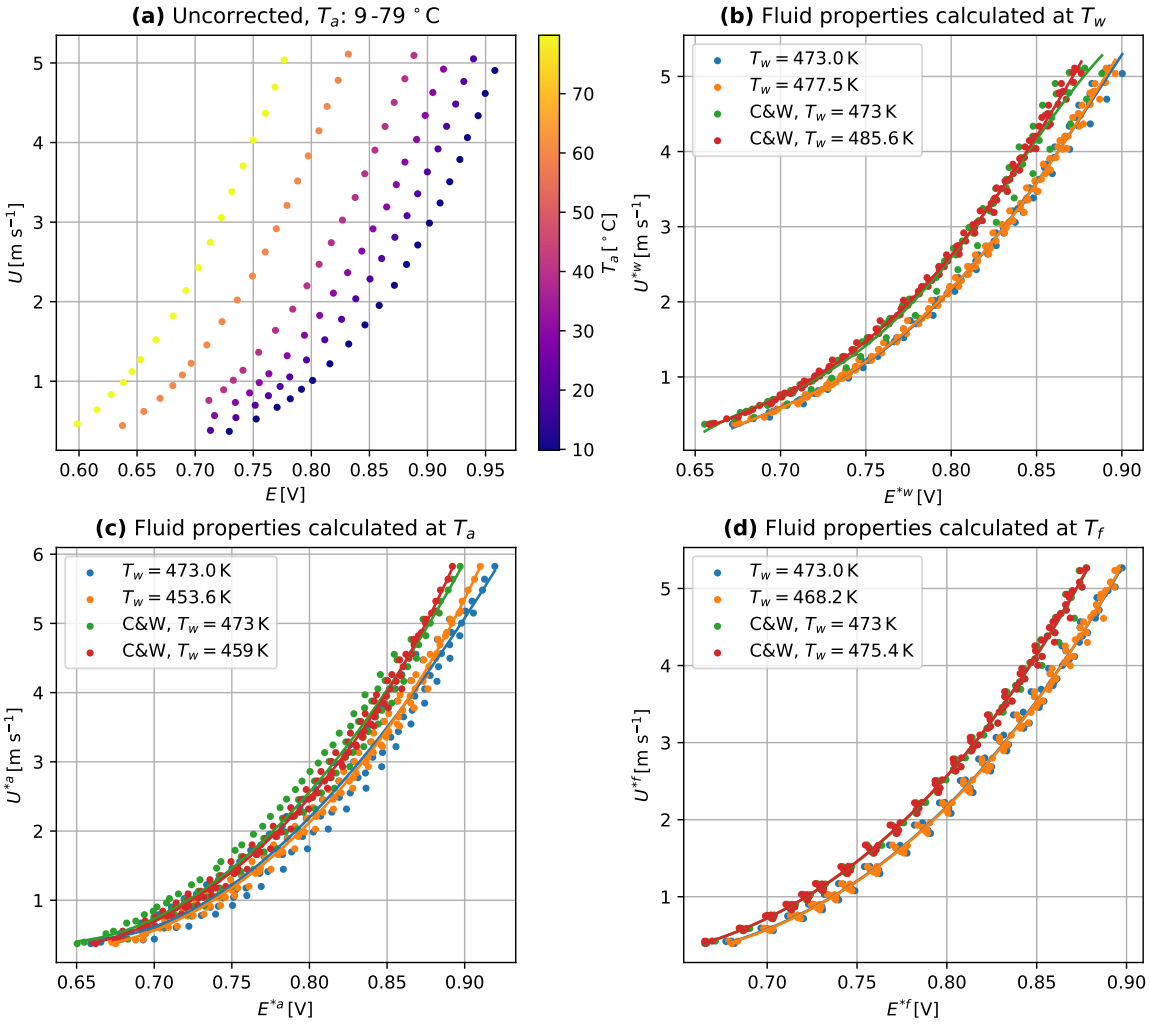

Figure B.10: Temperature correction comparison for Koppius & Trines data

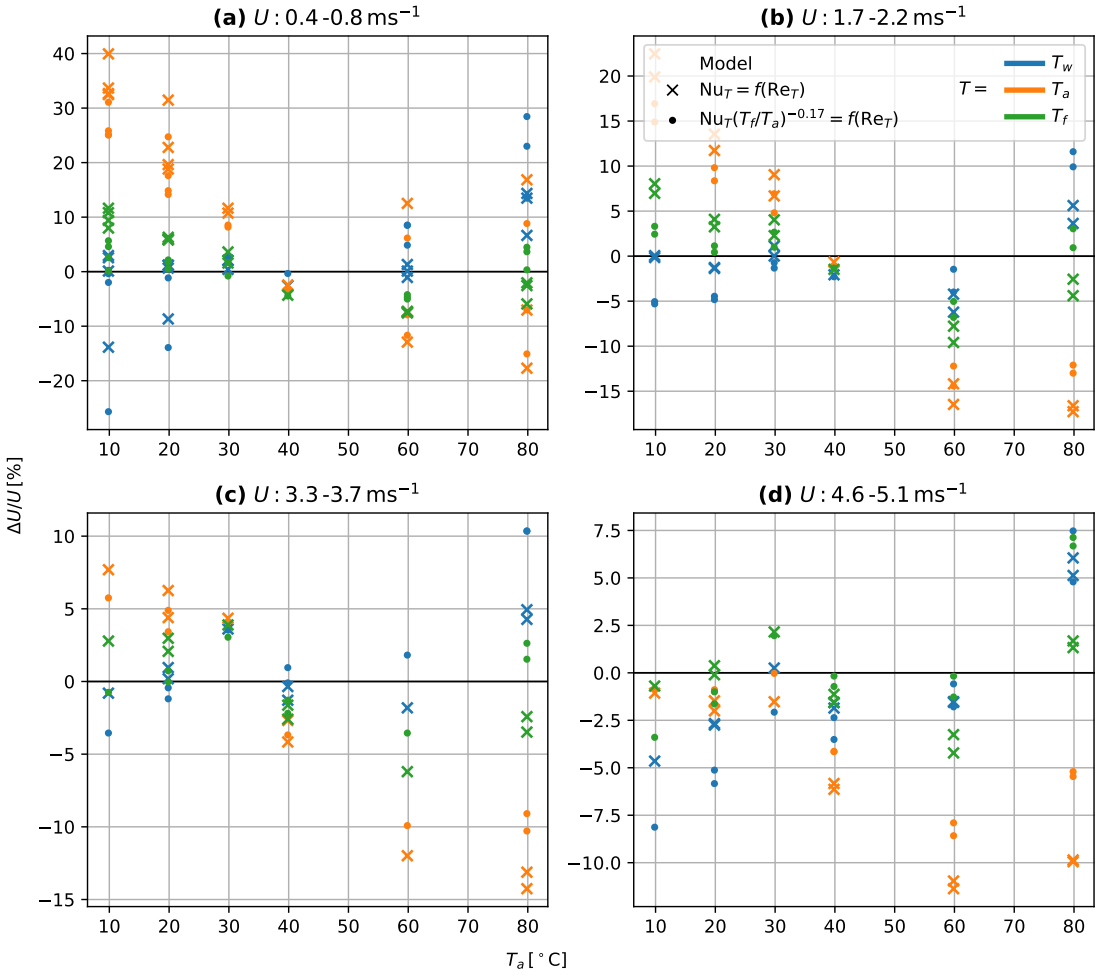

Figure B.11: Velocity error of calibration depending on correction for Koppius & Trines data, $T_w = 473\,\mathrm{K}$

Correction	T_w [K]	σ_U [m s^{-1}]	Max.ΔU [m s^{-1}]	ϵ_U [%]	Max.$\Delta U/U$ [%]
T_w	**473**	0.083	0.284	3.63	14.35
T_w	477.5	0.068	0.184	2.87	7.15
T_w, C&W	**473**	0.137	0.409	6.5	28.44
T_w, C&W	485.6	0.064	0.17	2.61	7.39
T_a	**473**	0.26	0.56	14.11	39.94
T_a	453.6	0.116	0.398	5.97	15.46
T_a, C&W	**473**	0.195	0.434	10.89	31.07
T_a, C&W	459.0	0.105	0.378	5.47	14.12
T_f	**473**	0.099	0.253	5.04	11.63
T_f	468.2	0.082	0.29	3.65	8.73
T_f, C&W	**473**	0.08	0.359	2.96	7.33
T_f, C&W	475.4	0.075	0.265	3.27	8.08

Table B.3: Velocity errors depending on the temperature correction of the Koppius & Trines data

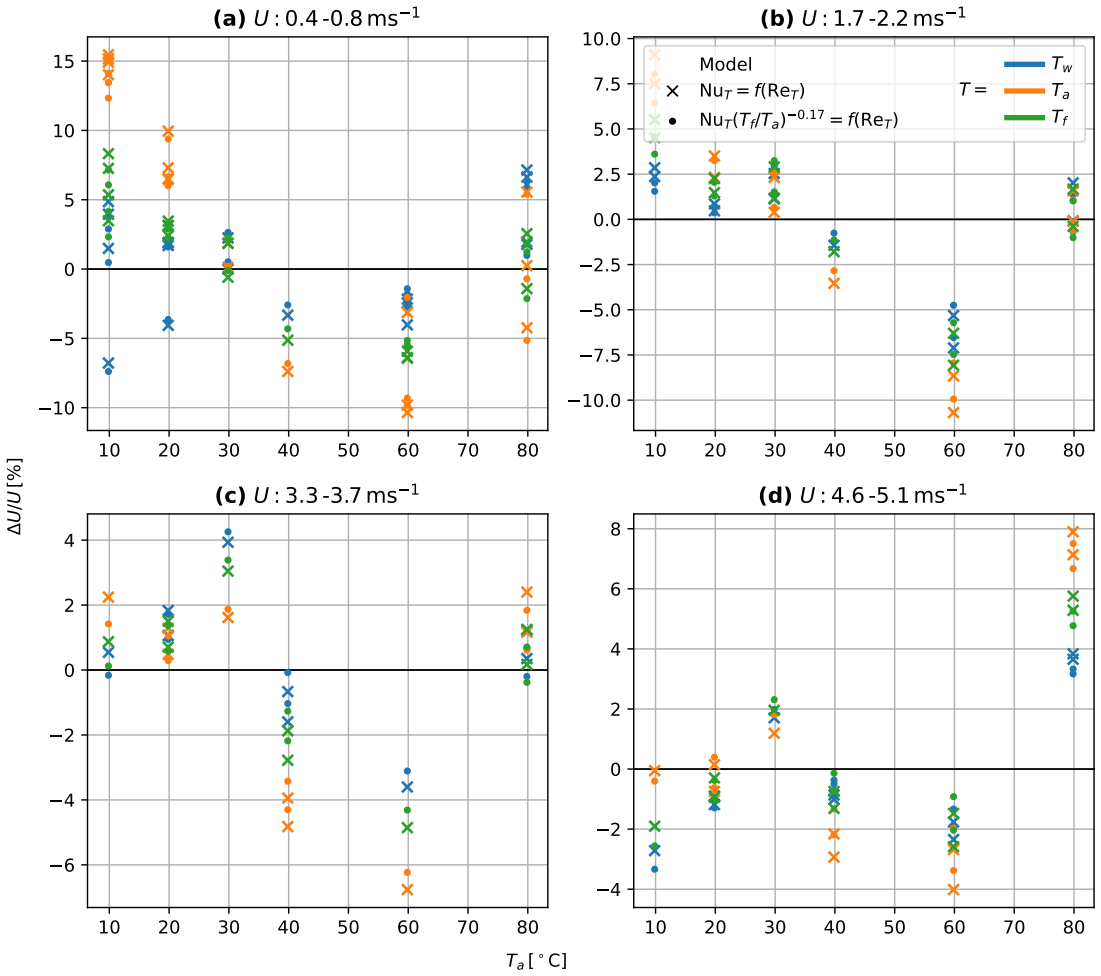

Figure B.12: Velocity error of calibration depending on correction for Koppius & Trines data, T_w optimized

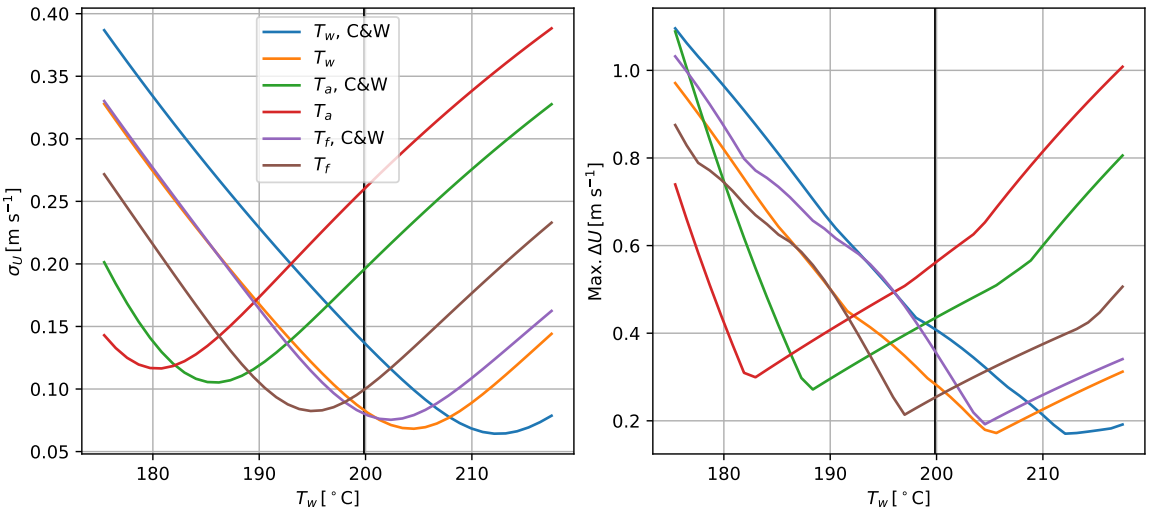

Figure B.13: Sensitivity of velocity error to T_w depending on correction for Koppius & Trines data

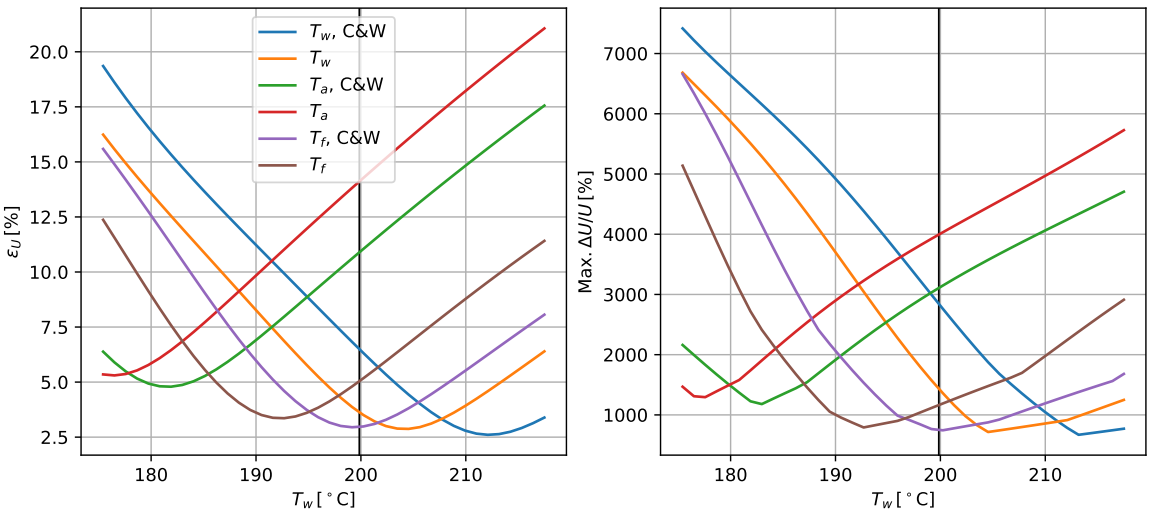

Figure B.14: Sensitivity of relative velocity error to T_w depending on correction for Koppius & Trines data

B.4. Artt & Brown data

Based on measurements from [32], with a reported overheat ratio of 1.8, assuming $T_0 = 25\,°\mathrm{C}$ -> $T_w = 1.8(25 + 273.15) = 536.7\,\mathrm{K}$. Also included in the plots, in bold in Table B.4, and as vertical lines in Fig. B.18 and 5.6

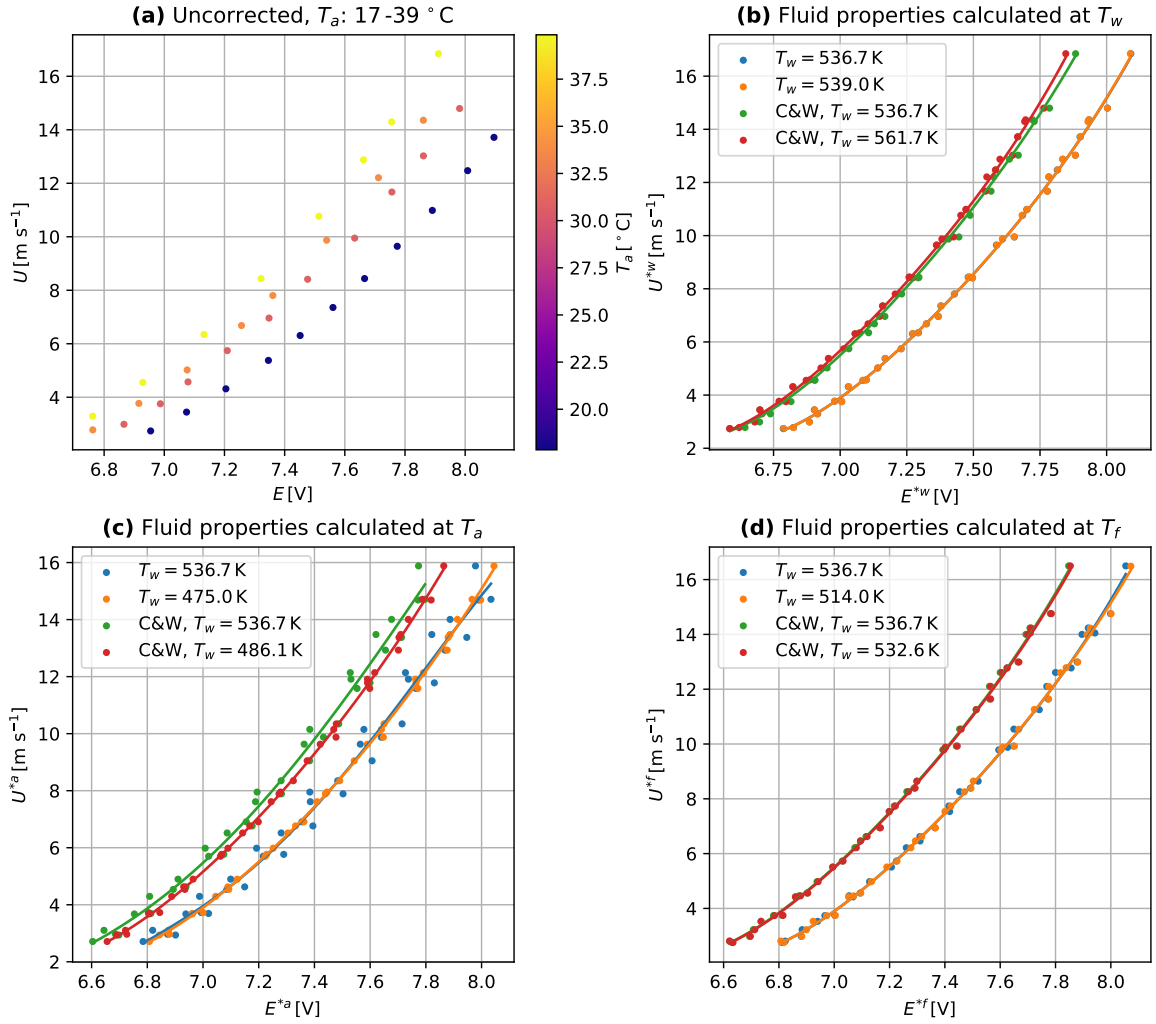

Figure B.15: Temperature correction comparison for Artt & Brown data

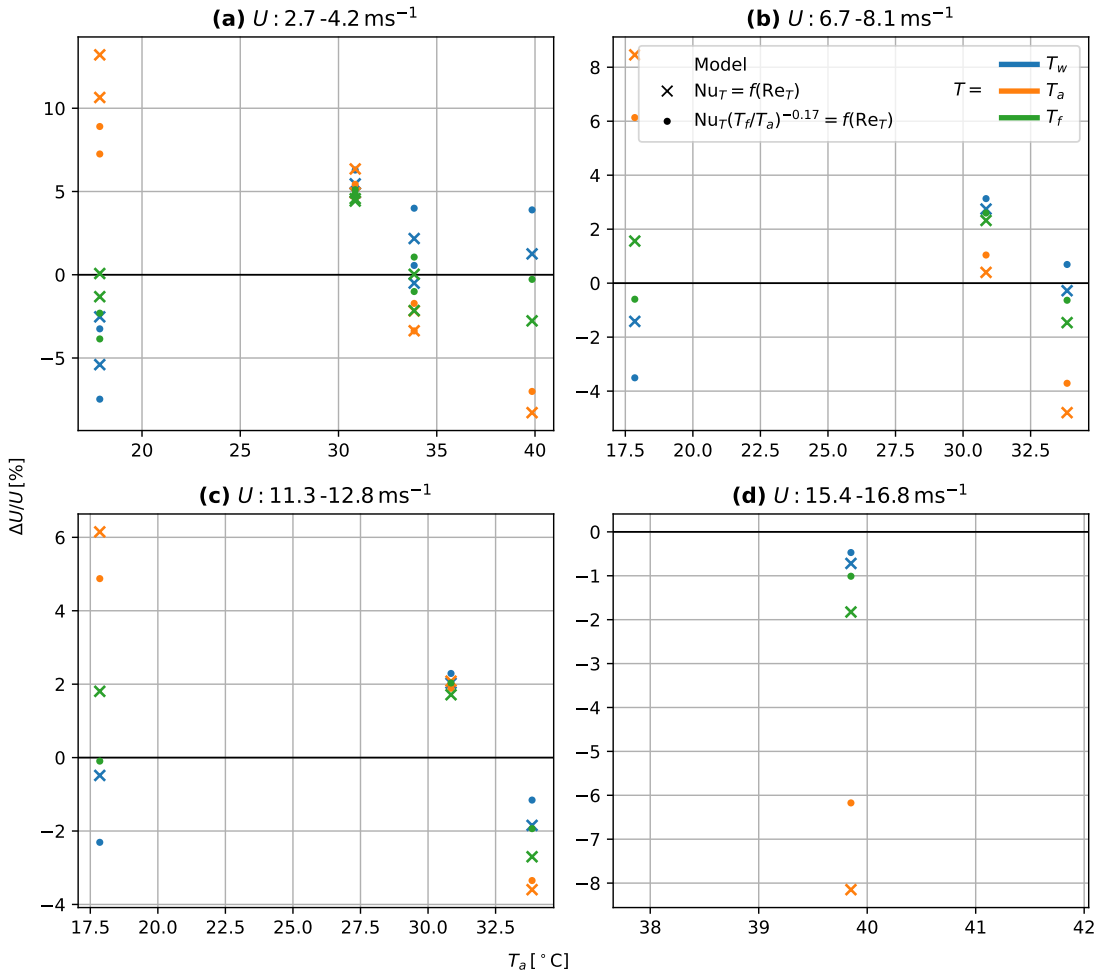

Figure B.16: Velocity error of calibration depending on correction for Artt & Brown data, $T_w = 536.7\,\mathrm{K}$

Correction	T_w [K]	σ_U [m s^{-1}]	Max.ΔU [m s^{-1}]	ϵ_U [%]	Max.$\Delta U/U$ [%]
T_w	**536.7**	0.163	0.428	2.27	5.46
T_w	539.0	0.162	0.438	2.2	5.38
T_w, C&W	**536.7**	0.211	0.429	3.23	7.47
T_w, C&W	561.7	0.166	0.449	2.24	5.47
T_a	**536.7**	0.537	1.373	6.59	13.21
T_a	475.0	0.136	0.357	1.67	4.62
T_a, C&W	**536.7**	0.422	1.04	5.08	8.9
T_a, C&W	486.1	0.139	0.366	1.71	4.72
T_f	**536.7**	0.212	0.474	2.25	4.57
T_f	514.0	0.153	0.407	2.0	5.11
T_f, C&W	**536.7**	0.159	0.433	1.98	5.11
T_f, C&W	532.6	0.157	0.419	2.05	5.22

Table B.4: Velocity errors depending on the temperature correction of the Artt & Brown data

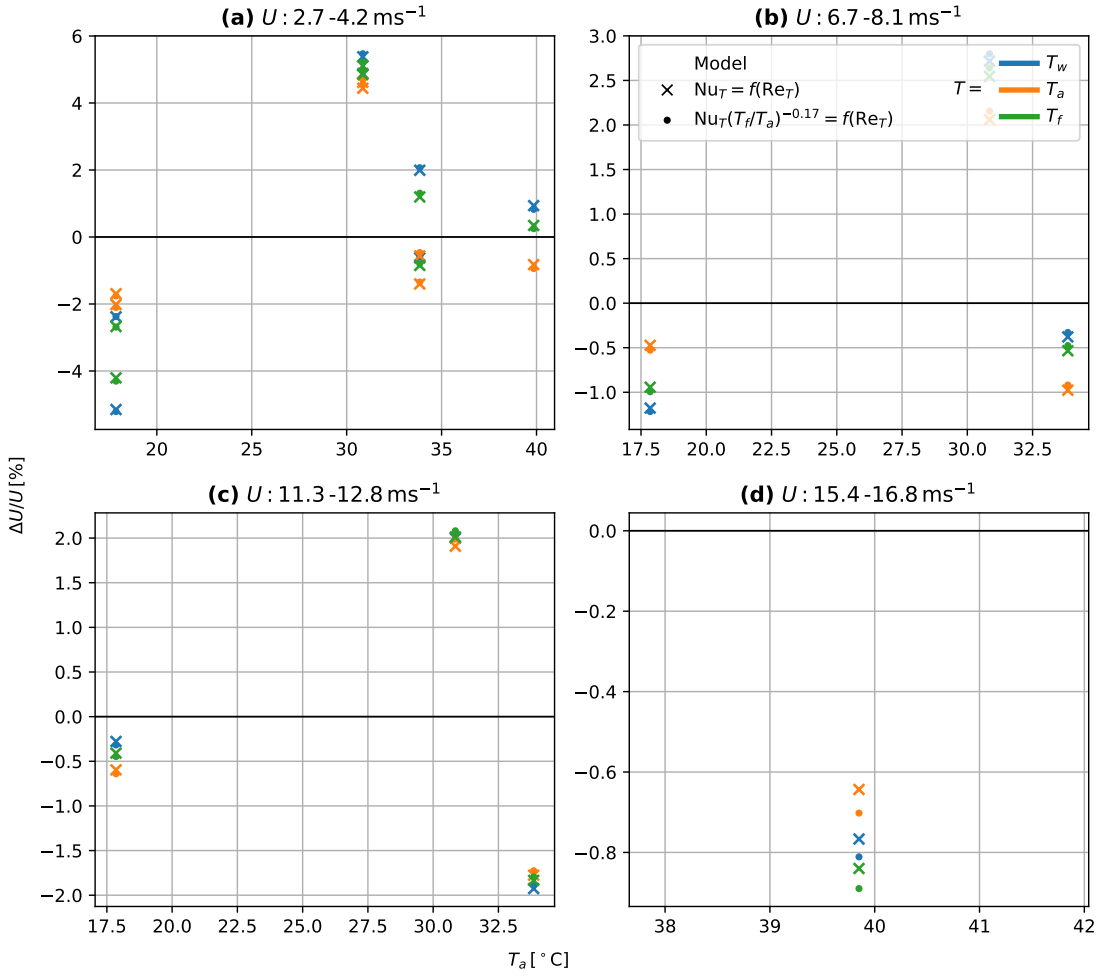

Figure B.17: Velocity error of calibration depending on correction for Artt & Brown data, T_w optimized

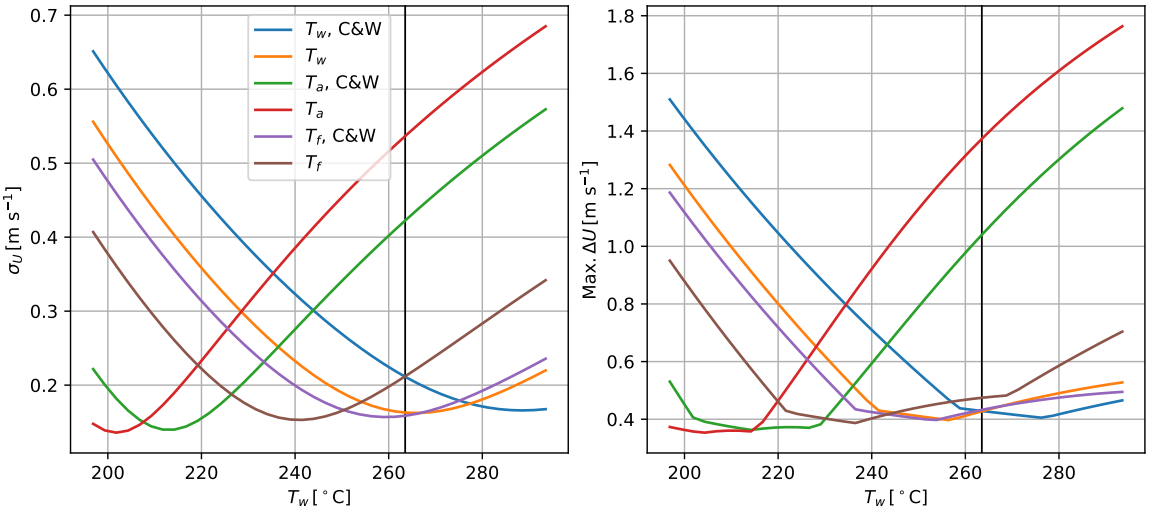

Figure B.18: Sensitivity of velocity error to T_w depending on correction for Artt & Brown data

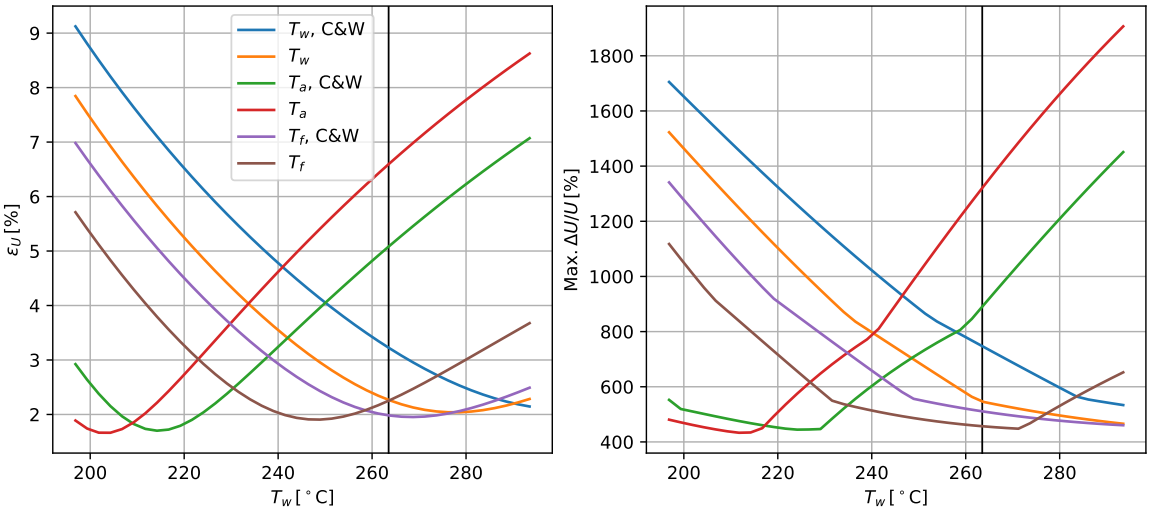

Figure B.19: Sensitivity of relative velocity error to T_w depending on correction for Artt & Brown data

C

X-wire Calibration Statistics

C.1. Statistic with full set used for calibration

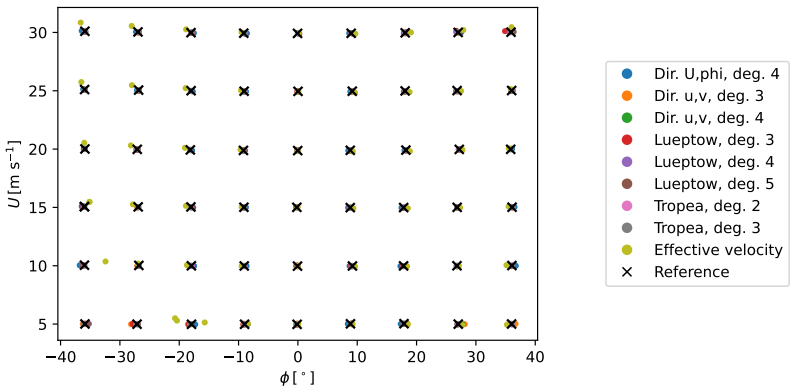

Figure C.1: Reference and predicted U and ϕ

Calibration	$\sigma_u\,[\mathrm{m\,s^{-1}}]$	$\mathrm{Max.}\Delta u\,[\mathrm{m\,s^{-1}}]$	$\sigma_v\,[\mathrm{m\,s^{-1}}]$	$\mathrm{Max.}\Delta v\,[\mathrm{m\,s^{-1}}]$
Dir. U,phi, deg. 4	0.069	0.626	0.136	0.951
Dir. u,v, deg. 3	0.05	0.245	0.035	0.157
Dir. u,v, deg. 4	0.03	0.115	0.027	0.12
Lueptow, deg. 3	0.048	0.383	0.057	0.427
Lueptow, deg. 4	0.026	0.115	0.042	0.235
Lueptow, deg. 5	0.025	0.161	0.033	0.249
Tropea, deg. 2	0.02	0.075	0.026	0.147
Tropea, deg. 3	0.019	0.075	0.025	0.12
Effective velocity	0.249	1.406	0.298	1.319

Table C.1: u and v error statistics

Calibration	ϵ_u [%]	Max.$\Delta u/U$ [%]	ϵ_v [%]	Max.$\Delta v/U$ [%]
Dir. U,phi, deg. 4	0.376	2.084	0.682	3.17
Dir. u,v, deg. 3	0.429	1.78	0.35	1.755
Dir. u,v, deg. 4	0.302	1.808	0.233	1.707
Lueptow, deg. 3	0.307	1.756	0.326	1.464
Lueptow, deg. 4	0.203	1.744	0.259	1.815
Lueptow, deg. 5	0.177	0.921	0.196	1.66
Tropea, deg. 2	0.152	1.073	0.154	0.784
Tropea, deg. 3	0.157	1.143	0.147	0.766
Effective velocity	2.884	28.055	2.533	26.311

Table C.2: u and v relative error statistics

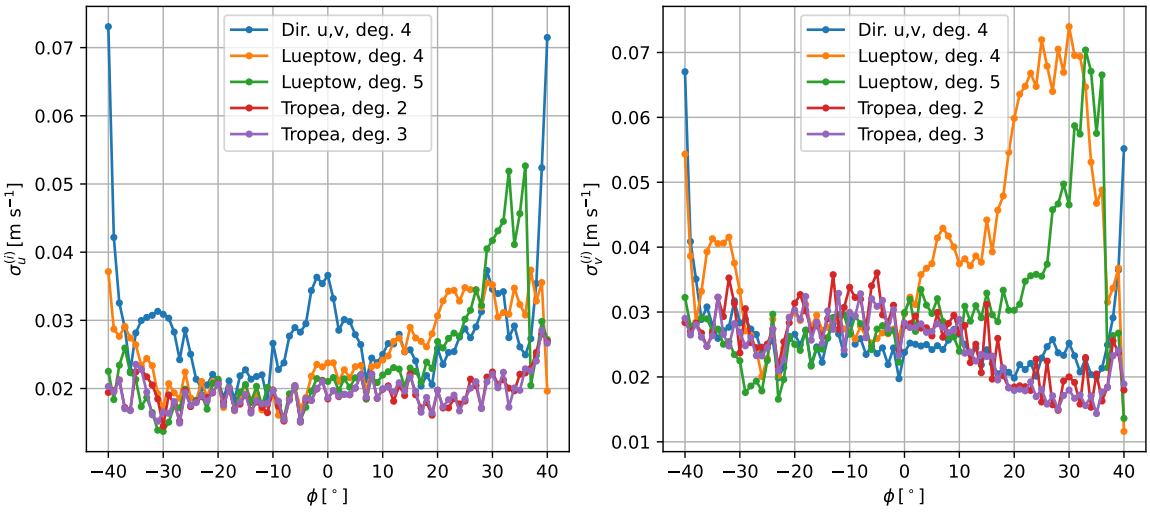

Figure C.2: σ_u and σ_v as a function of ϕ

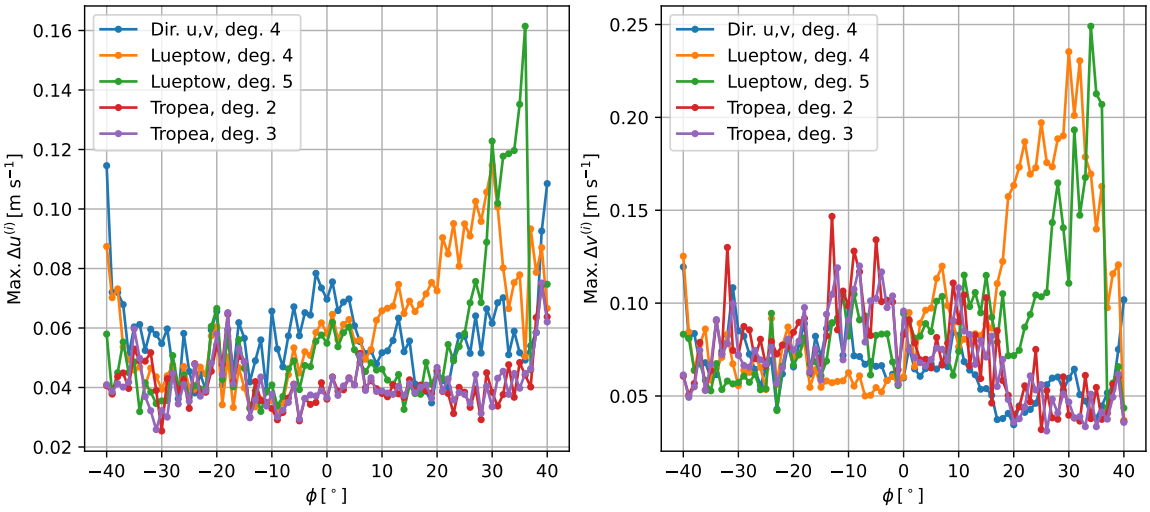

Figure C.3: Max. Δu and Δv as a function of ϕ

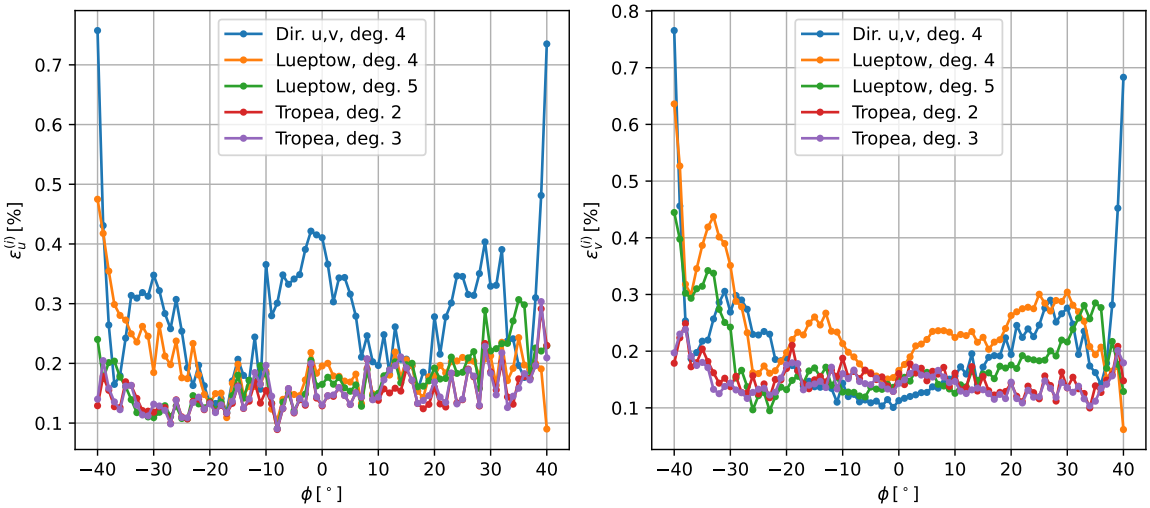

Figure C.4: ϵ_u and ϵ_v as a function of ϕ

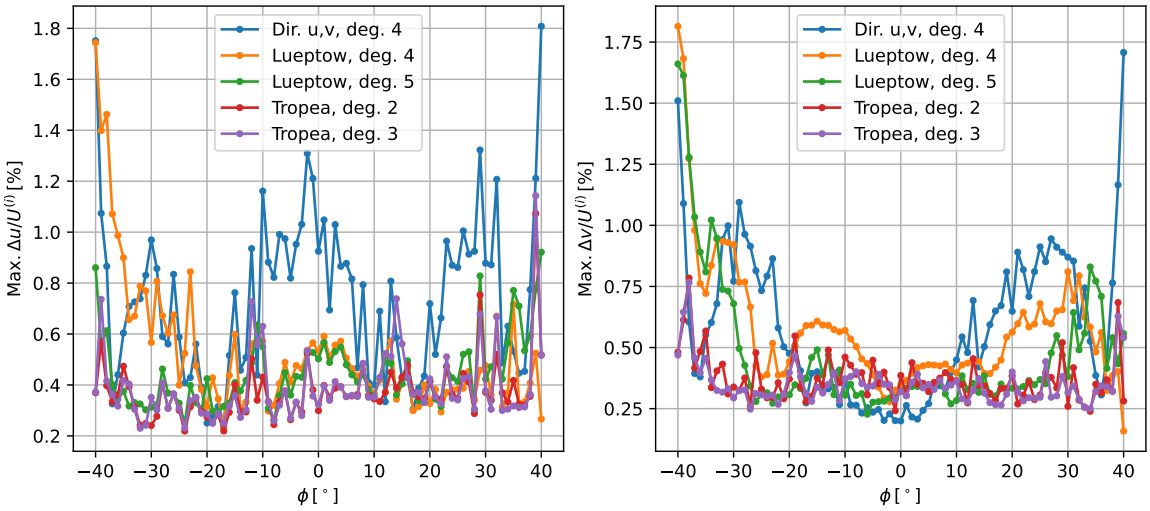

Figure C.5: Max. $\Delta u/U$ and $\Delta v/U$ as a function of ϕ

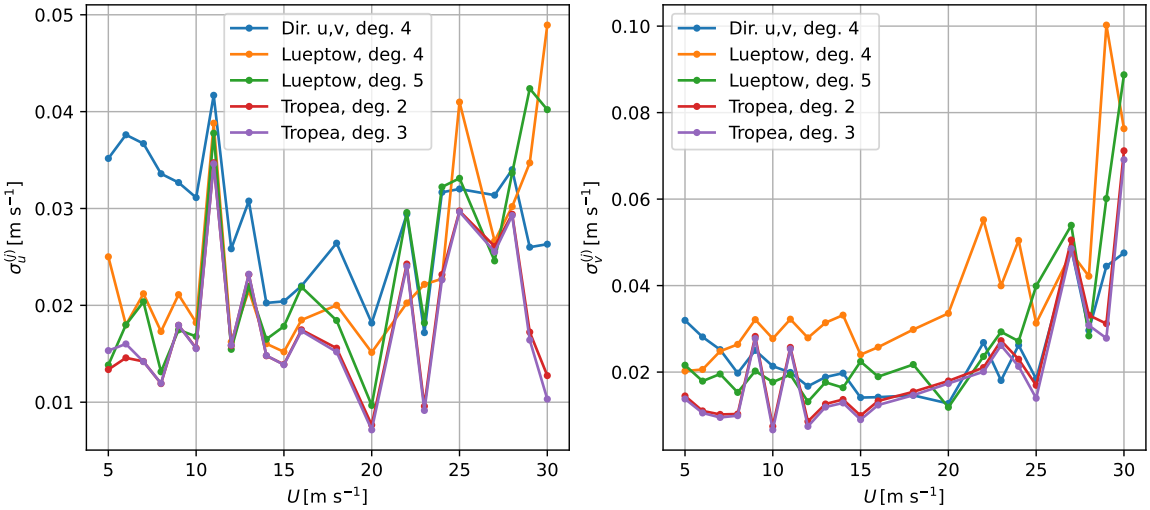

Figure C.6: σ_u and σ_v as a function of U

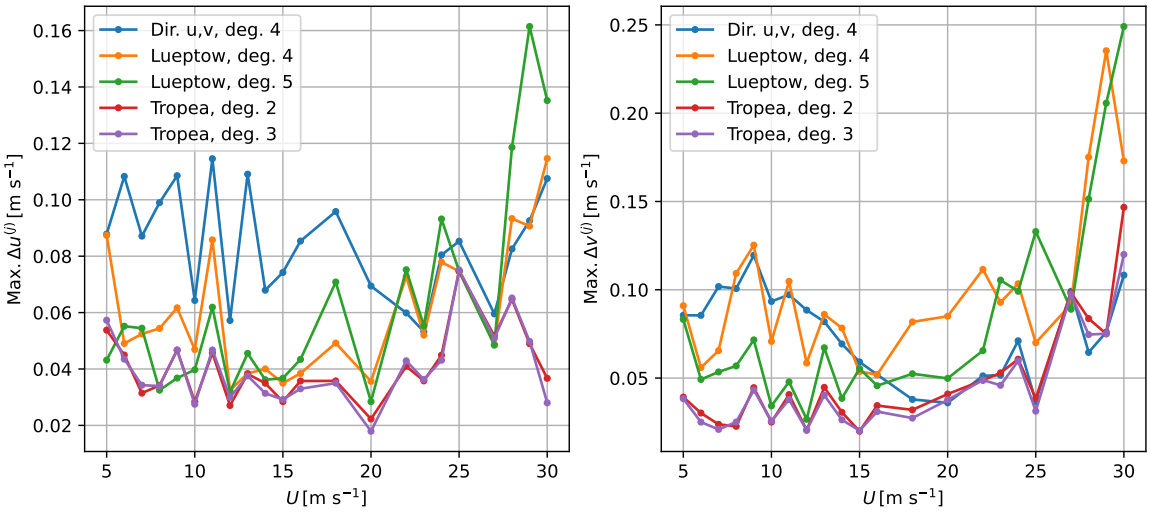

Figure C.7: Max. Δu and Δv as a function of U

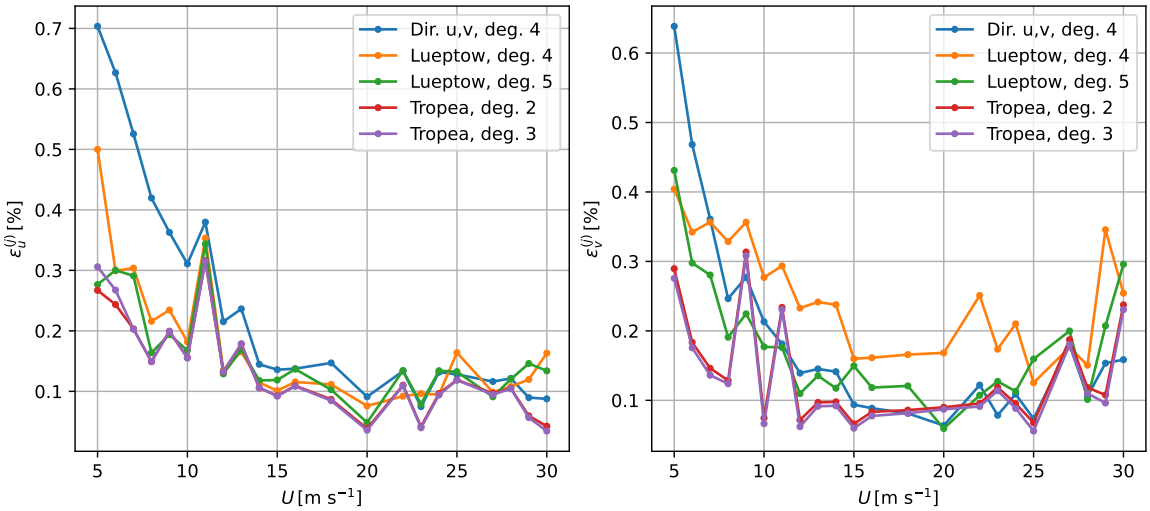

Figure C.8: ϵ_u and ϵ_v as a function of U

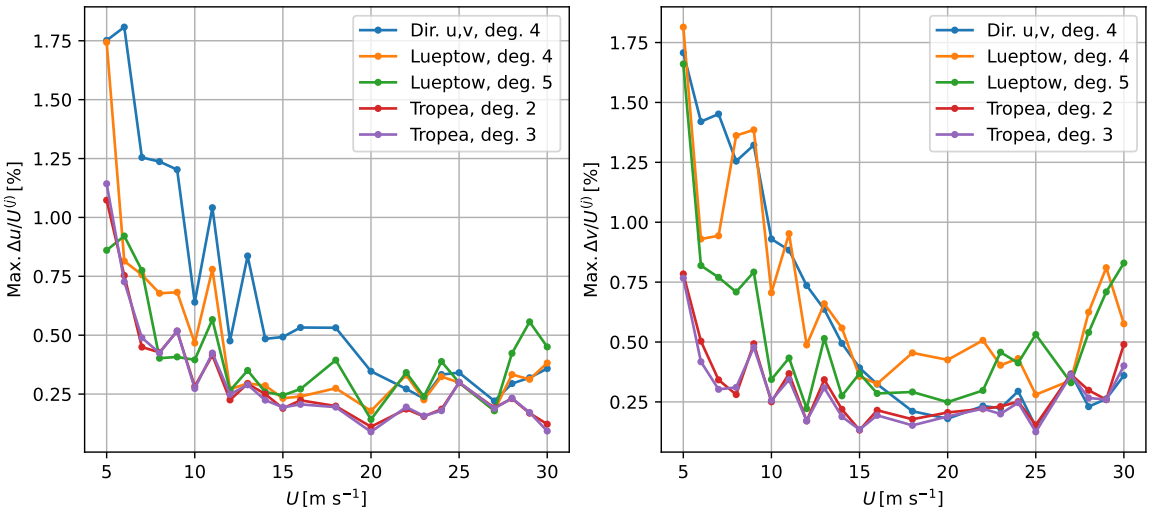

Figure C.9: Max. $\Delta u/U$ and $\Delta v/U$ as a function of U

C.2. Convergence in number of U levels

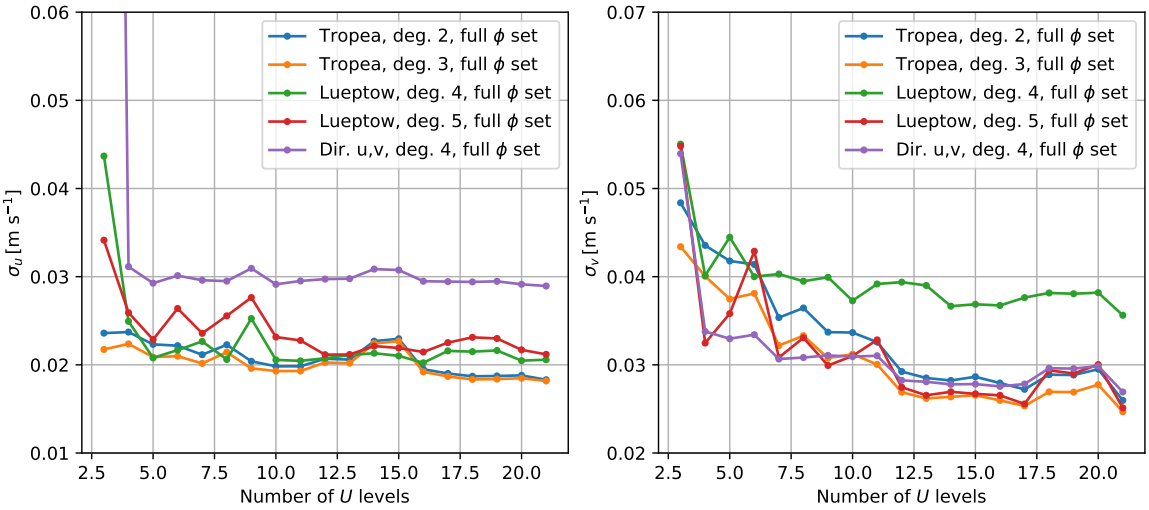

Figure C.10: σ_u and σ_v depending on number of U levels

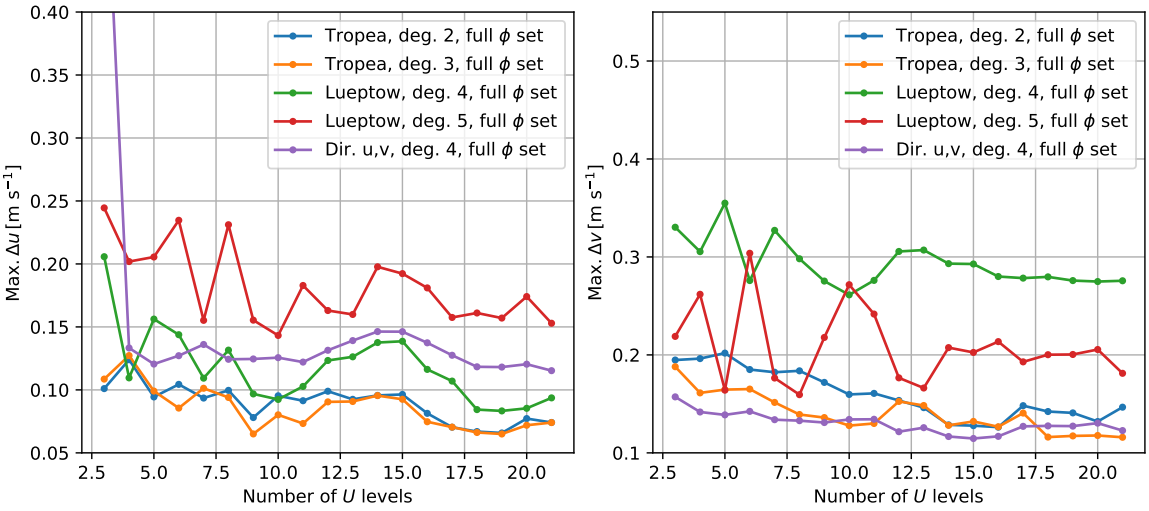

Figure C.11: Max. Δu and Δv depending on number of U levels

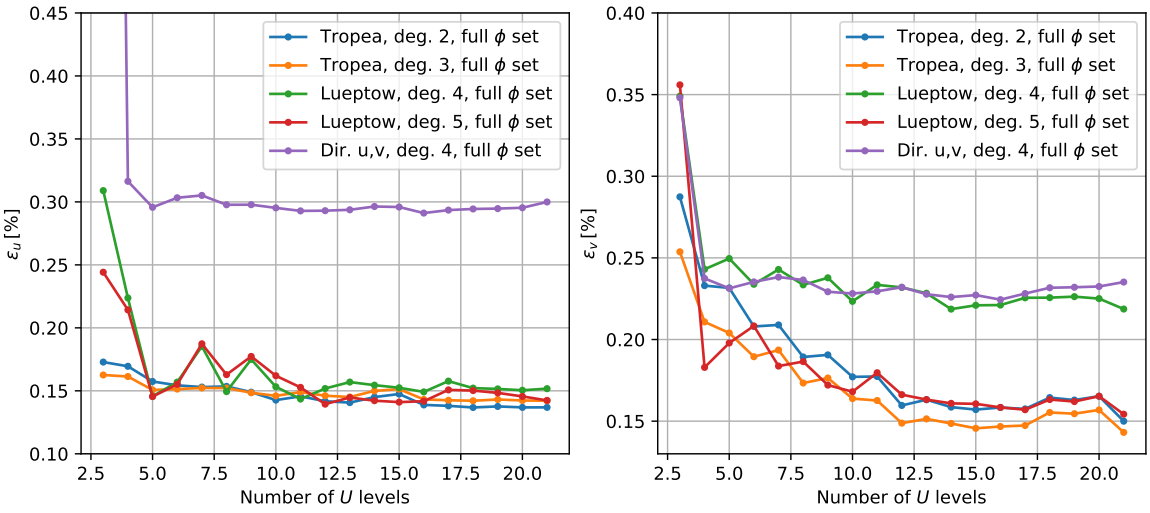

Figure C.12: ϵ_u and ϵ_v depending on number of U levels

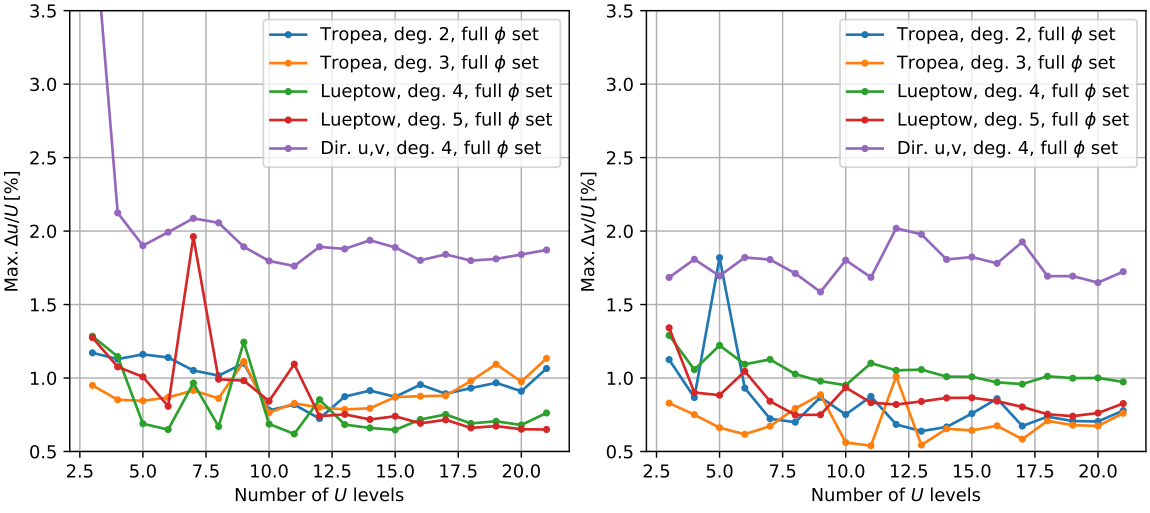

Figure C.13: Max. $\Delta u/U$ and $\Delta v/U$ depending on number of U levels

C.3. Convergence in number of angle levels

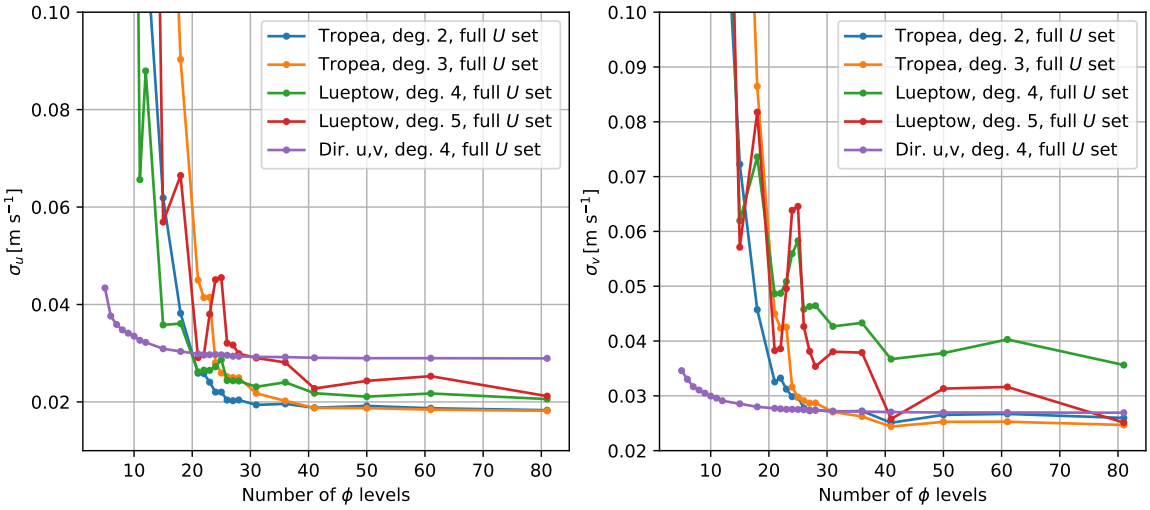

Figure C.14: σ_u and σ_v depending on number of ϕ levels

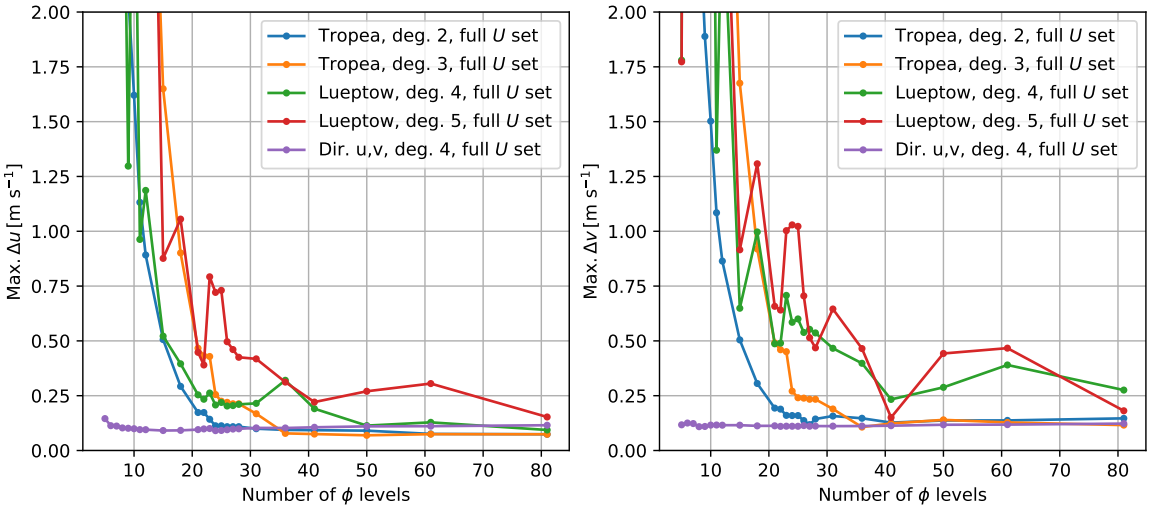

Figure C.15: Max. Δu and Δv depending on number of ϕ levels

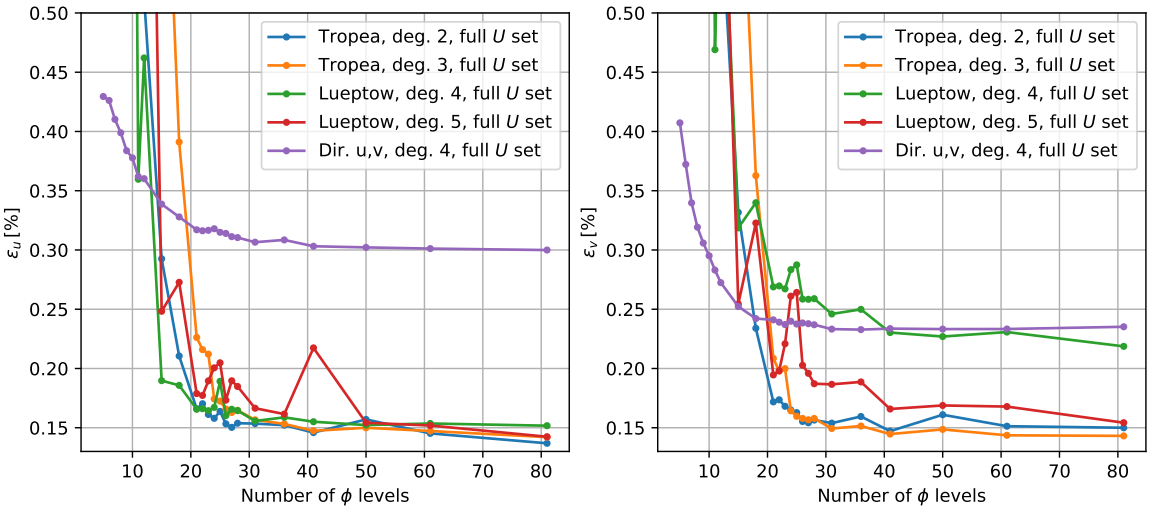

Figure C.16: ϵ_u and ϵ_v depending on number of ϕ levels

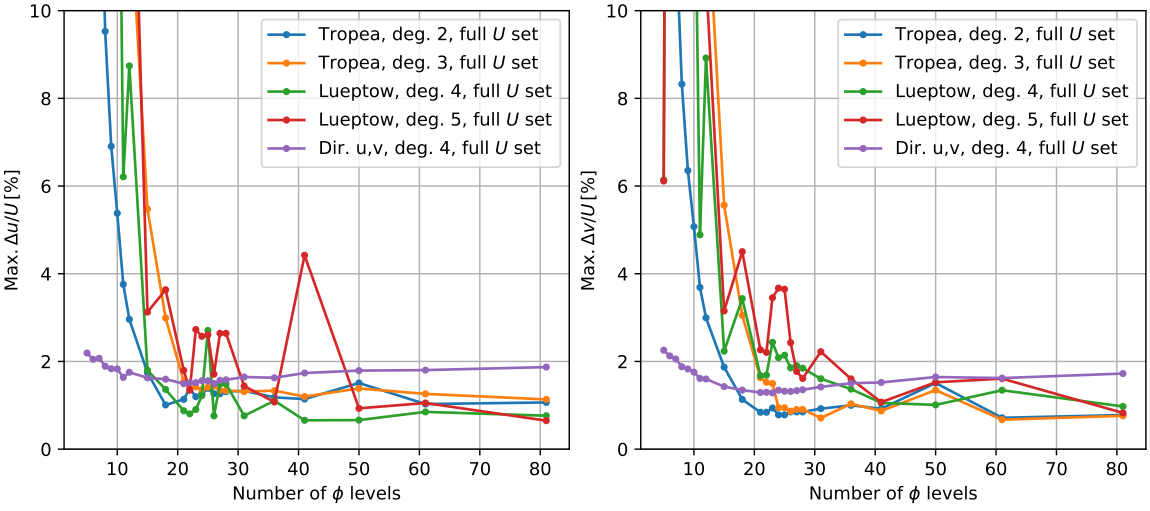

Figure C.17: Max. $\Delta u/U$ and $\Delta v/U$ depending on number of ϕ levels

C.4. Convergence in number of angle levels at reduced U levels

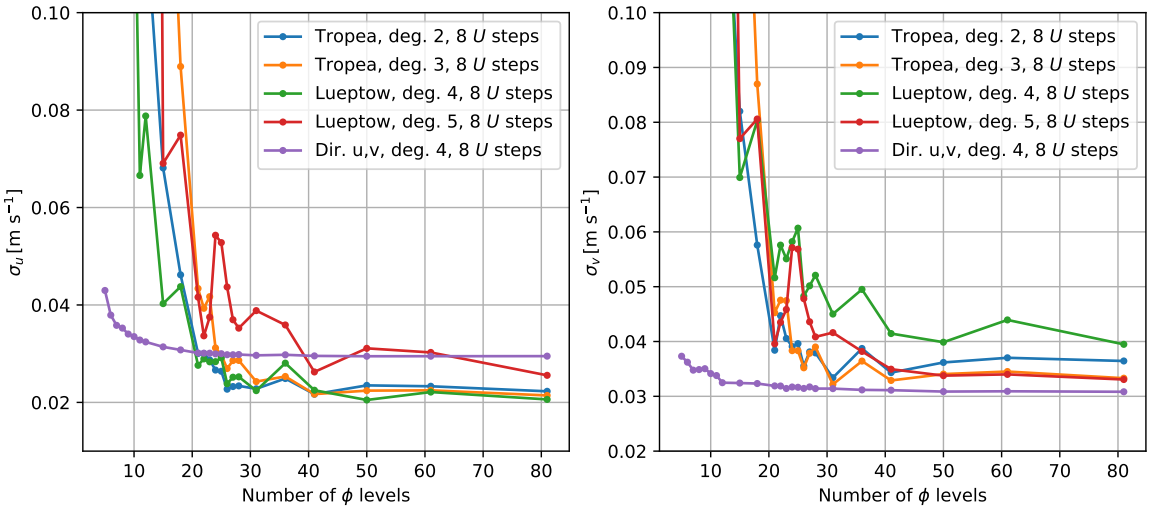

Figure C.18: σ_u and σ_v depending on number of ϕ levels at 8 U levels

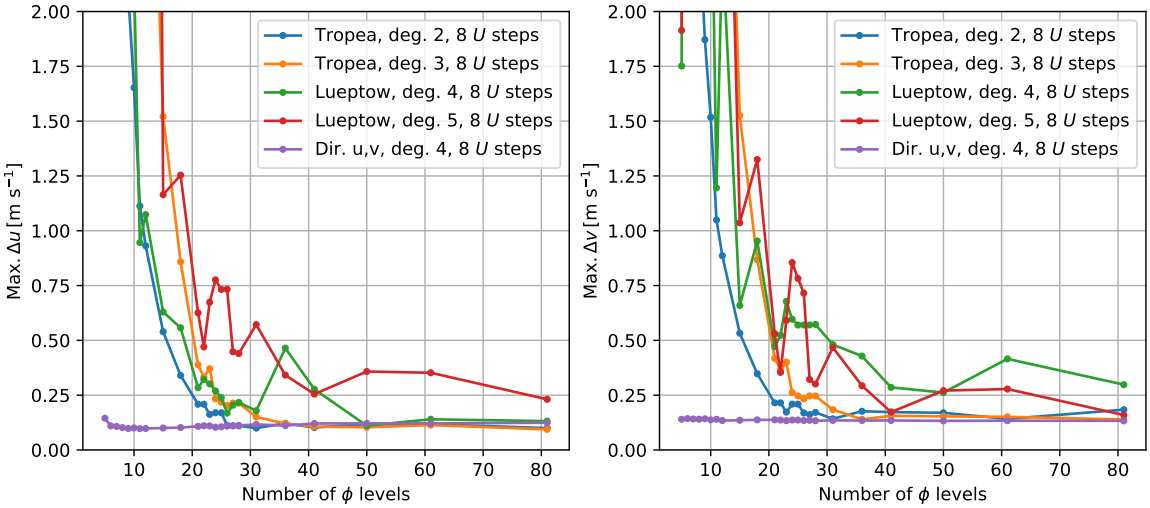

Figure C.19: Max. Δu and Δv depending on number of ϕ levels at 8 U levels

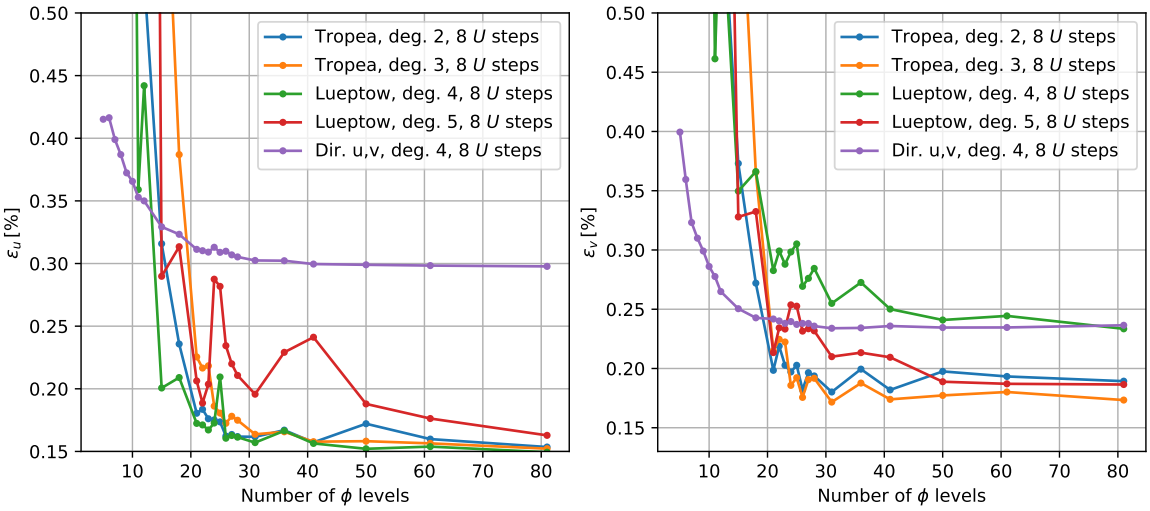

Figure C.20: ϵ_u and ϵ_v depending on number of ϕ levels at 8 U levels

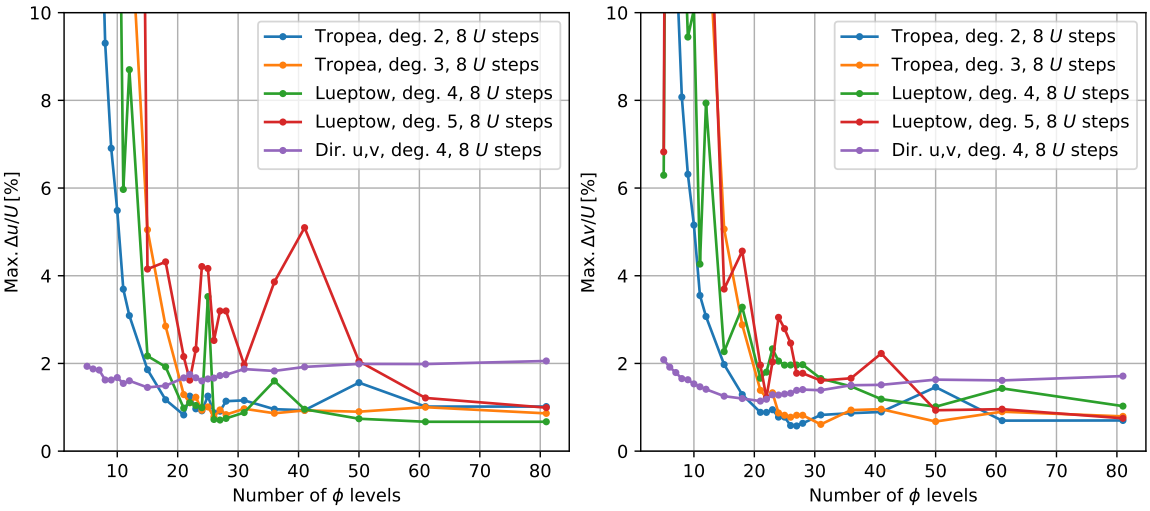

Figure C.21: Max. $\Delta u/U$ and $\Delta v/U$ depending on number of ϕ levels at 8 U levels

C.5. Statistics with reduced U and ϕ calibration grid

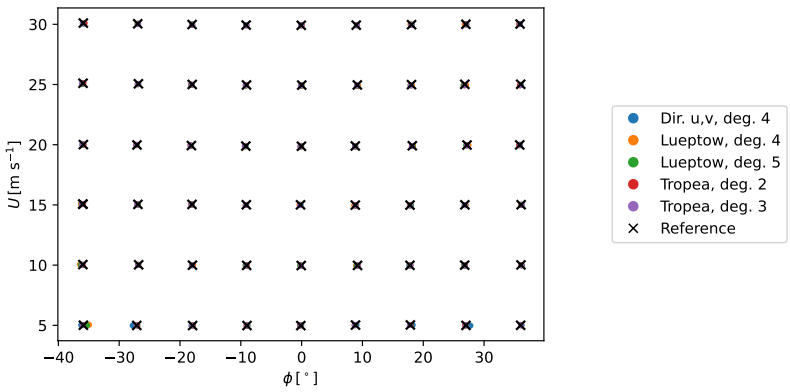

Figure C.22: Reference and predicted U and ϕ

Calibration	σ_u [m s^{-1}]	Max.Δu [m s^{-1}]	σ_v [m s^{-1}]	Max.Δv [m s^{-1}]
Dir. u,v, deg. 4	0.033	0.107	0.04	0.157
Lueptow, deg. 4	0.034	0.25	0.066	0.772
Lueptow, deg. 5	0.054	0.924	0.069	1.064
Tropea, deg. 2	0.027	0.114	0.041	0.172
Tropea, deg. 3	0.031	0.21	0.042	0.274

Table C.3: u and v error statistics

Calibration	ϵ_u [%]	Max.$\Delta u/U$ [%]	ϵ_v [%]	Max.$\Delta v/U$ [%]
Dir. u,v, deg. 4	0.303	1.682	0.256	1.304
Lueptow, deg. 4	0.222	1.819	0.332	2.725
Lueptow, deg. 5	0.255	3.297	0.306	3.741
Tropea, deg. 2	0.176	0.929	0.209	0.671
Tropea, deg. 3	0.189	0.781	0.208	1.054

Table C.4: u and v relative error statistics

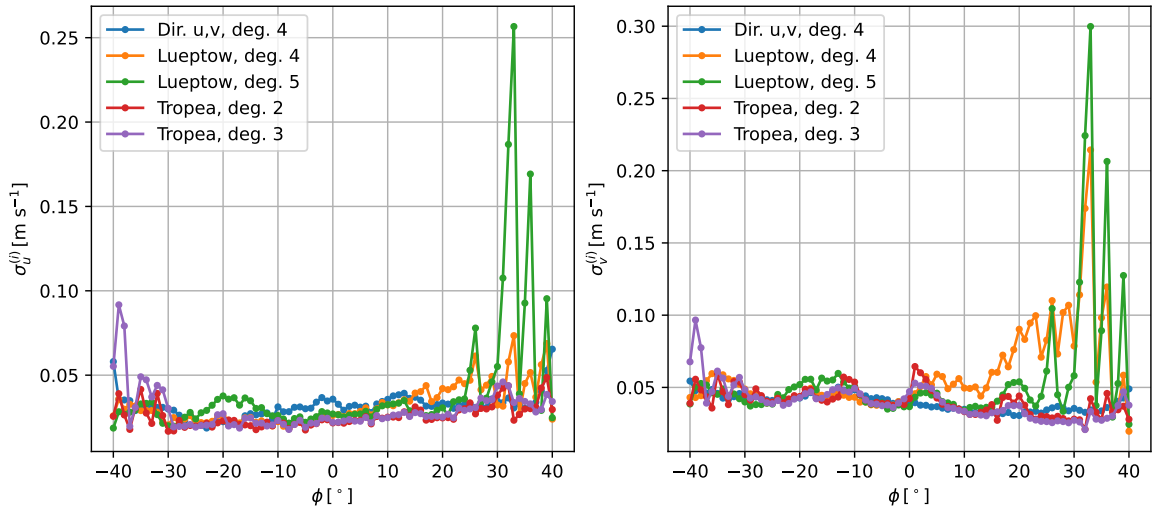

Figure C.23: σ_u and σ_v as a function of ϕ

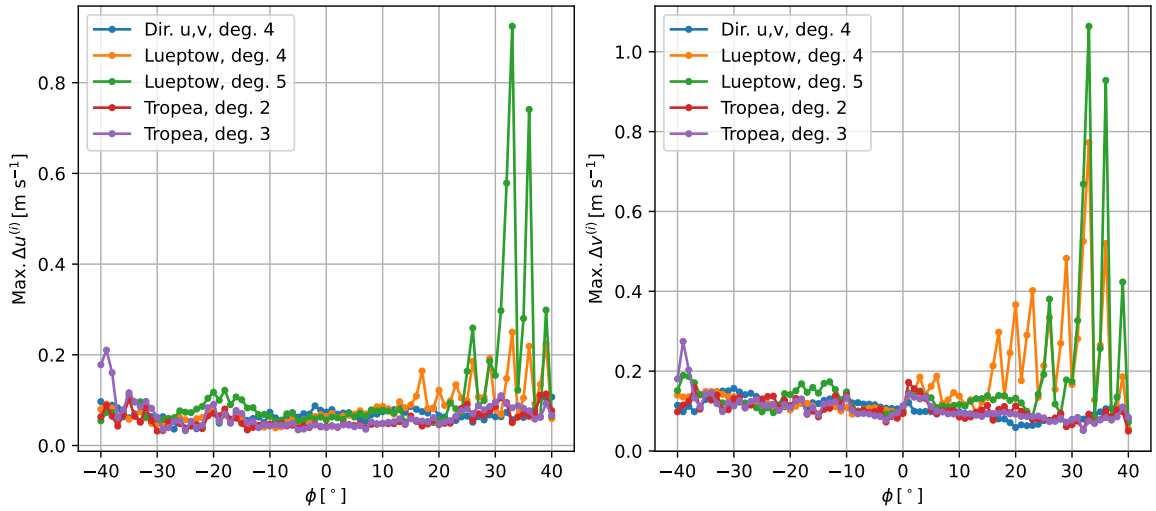

Figure C.24: Max. Δu and Δv as a function of ϕ

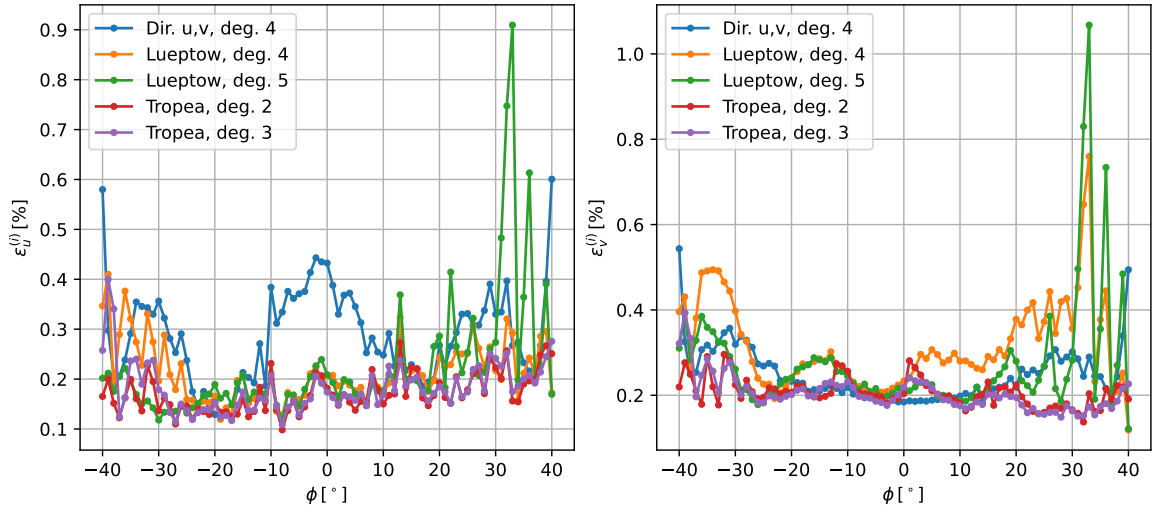

Figure C.25: ϵ_u and ϵ_v as a function of ϕ

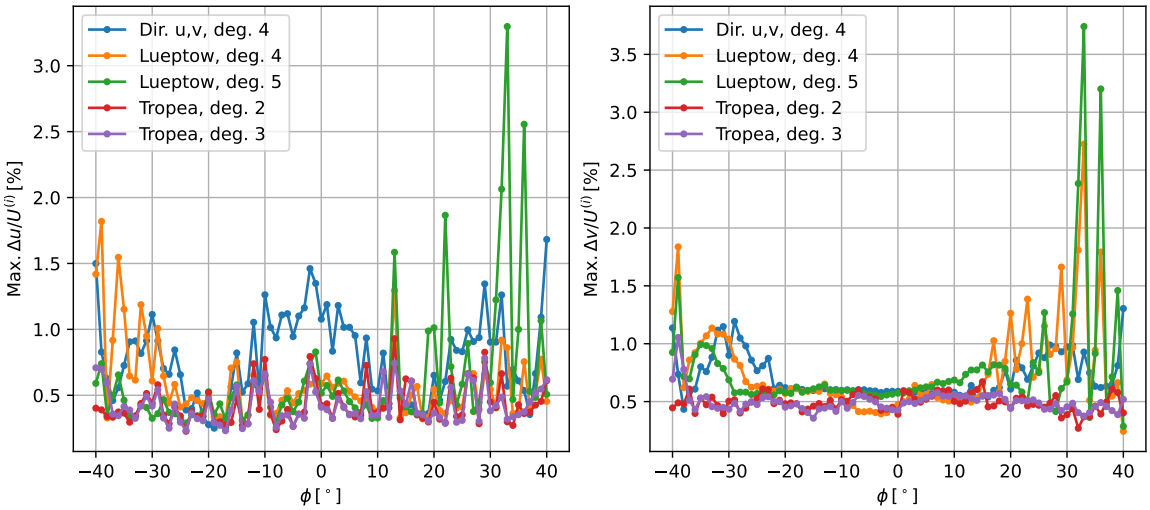

Figure C.26: Max. $\Delta u/U$ and $\Delta v/U$ as a function of ϕ

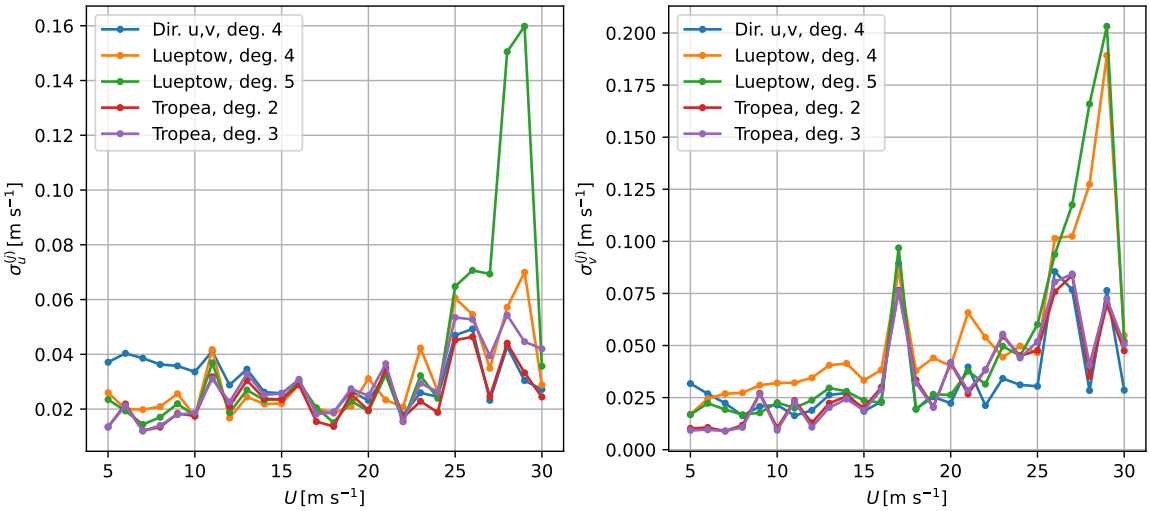

Figure C.27: σ_u and σ_v as a function of U

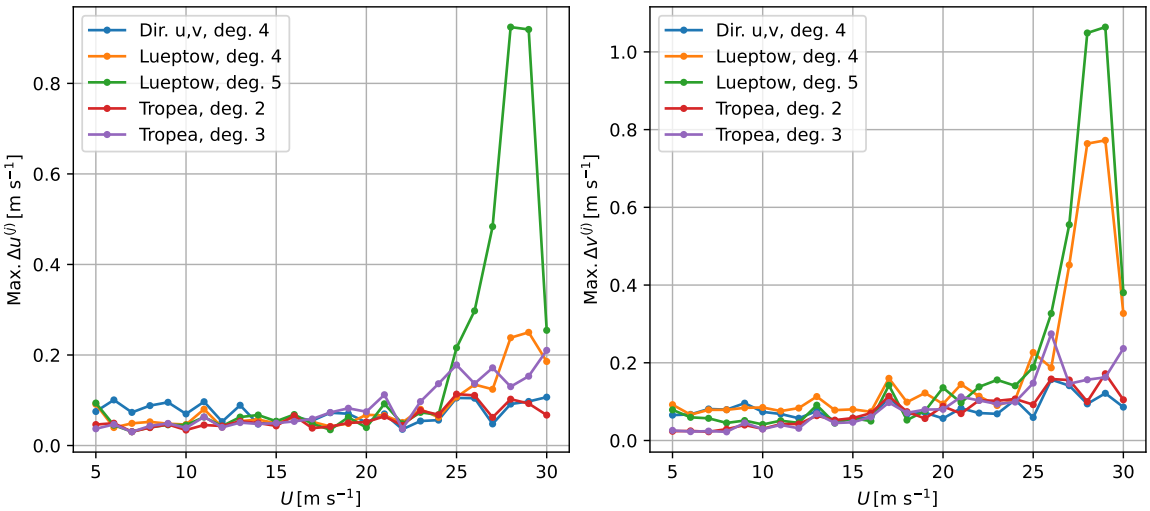

Figure C.28: Max. Δu and Δv as a function of U

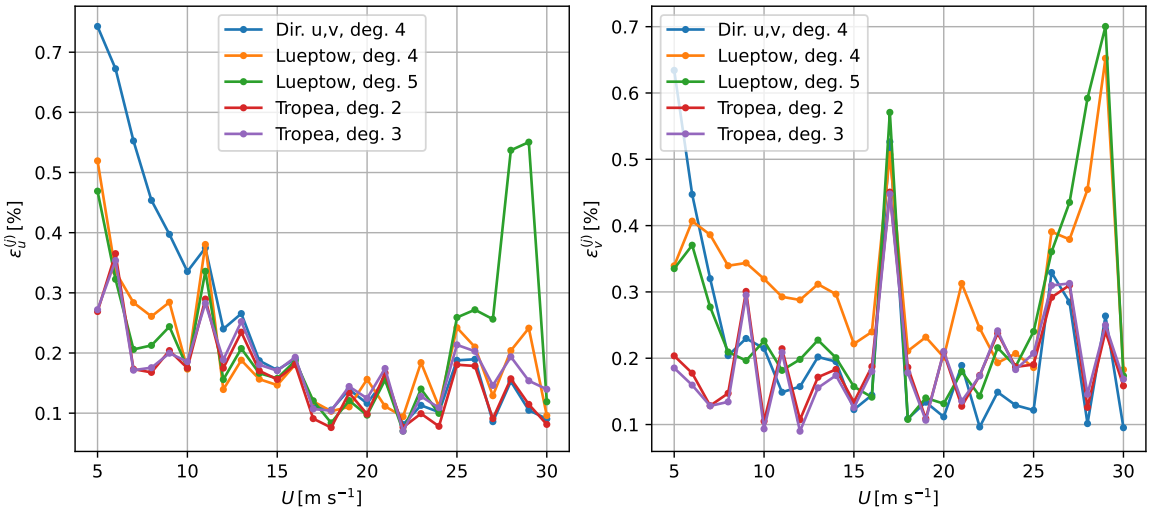

Figure C.29: ϵ_u and ϵ_v as a function of U

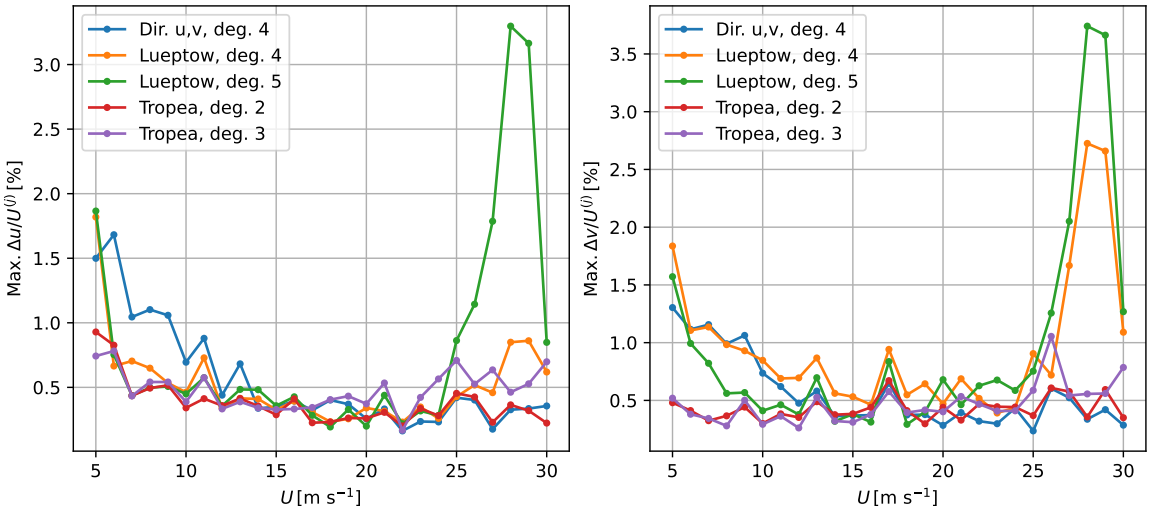

Figure C.30: Max. $\Delta u/U$ and $\Delta v/U$ as a function of U